POLITECNICO DI TORINO

**Corso di Laurea Magistrale
in Ingegneria Energetica e Nucleare**

Tesi di Laurea Magistrale

Solid Oxide Electrolysis System: Dynamic modelling and microgrid integration

Relatori:

Prof. Massimo Santarelli

Dott. Andrea Lanzini   **Candidato**

Prof. Jack Brouwer   Paolo Colombo

Aprile 2018

Acknowledgements

I would like to thank my supervisors professors Massimo Santarelli, Andrea Lanzini and Jack Brouwer for giving me the opportunity to work at my thesis at the University of California, Irvine. It has been an academic and life enriching experience that I will never forget.

Thanks to Alireza Saeedmanesh, who has shared with me long hours of work and without whom this thesis would not have been possible.

Thanks to Paolo Colbertaldo, a travel companion and a true friend who was there with me during happy and difficult moments, and never failed to cheer me up.

Finally, I'm grateful to my parents who have always supported me throughout my entire life and in the realization of my dream to conclude my studies abroad.

Abstract

In the future sustainable global system based on renewable energy sources, large scale electrical energy storage is going to have a fundamental role.

In this work a physical dynamic model of a high temperature steam electrolysis system based on Solid Oxide Cells has been developed. A thorough analysis on cell and balance of plant components has been carried out, focusing on dynamic and part load operation. Two system control strategies have been proposed and investigated to compare steady state and dynamic performances in terms of cell thermal management and hydrogen production efficiency. A system electrical efficiency higher than $70\%_{LHV}$ has been obtained for stack loads in the range 30-100% confirming that solid oxide electrolysis could be effectively coupled with intermittent renewable energy sources. The system electrical efficiency can be improved to values higher than $80\%_{LHV}$ if an external heat source is available for steam generation. Moreover, no challenges in terms of mechanical stresses on cell materials caused by thermal gradients during steady state and dynamic operation have been found.

The impact of increasing renewable energy sources deployment has been evaluated in the microgrid of the campus of the University of California, Irvine, modelling the existing power plant based on a natural gas fueled combined cycle and its response to additional photovoltaic installations. The renewable energy penetration of the campus electrical demand could increase to 19% with the installation of 35 MW of photovoltaic capacity, but 58% of the photovoltaic production would have to be curtailed. The integration of a modular Solid Oxide Electrolysis system in the microgrid to absorb the excessive photovoltaic power production has been simulated investigating the possibility of heat recovery from the gas turbine exhausts for steam generation. Two dispatch strategies of the electrolysis system have been compared and annual average efficiency values higher than $78\%_{LHV}$ have been obtained when both electrical and thermal integration have been considered, absorbing up to 95% of the otherwise curtailed photovoltaic electricity.

Contents

List of figures

6

List of tables

List of acronyms

ALK	Alkaline electrolyzer
ASR	Area specific resistance
CC	Combined cycle
CSP	Concentrated solar power
GT	Gas turbine
HHV	Higher heating value
HRSG	Heat recovery steam generator
LHV	Lower heating value
LSC	Lanthanum strontium cobaltite
LSCF	Lanthanum strontium cobaltite ferrite
LSM	Lanthanum strontium manganite
PEM	Proton exchange membrane
PEN	Positive electrode- electrolyte- negative electrode
PHS	Pumped hydro storage
PI	Proportional integral
PV	Photovoltaic
SCE	Southern California Edison
SOC	Solid oxide cell
SOEC	Solid oxide electrolysis cell
SOFC	Solid oxide fuel cell
SRU	Single repeating unit
ST	Steam turbine
SU	Steam utilization factor
TET	Turbine exit temperature
VRES	Variable renewable energy sources
YSZ	Yttria-stabilized zirconia

List of symbols

c_p	Specific heat capacity at constant pressure [$kJ/kg\,K$]
h_{conv}	Convective heat transfer coefficient [W/m^2]
$\dot{H}$	Total enthalpy of a stream [kW]
$\dot{m}$	Mass flow rate [kg/s]
$\dot{n}$	Molar flow rate [$kmol/s$]
$\dot{Q}$	Heat flux [kW]
V_{Rev}	Cell reversible voltage [V]
$\dot{V}$	Volumetric flow rate [m^3/s]
$\dot{\chi}$	Molar fraction [$-$]
ΔG	Molar Gibbs free energy difference [kJ/mol]
ΔH	Molar enthalpy difference [kJ/mol]
ΔS	Molar entropy difference [kJ/mol]
F	Faraday constant 96,485 [C/mol]
h	Specific enthalpy [$kJ/kmol$]
i	Current density [A/cm^2]
I	Current [A]
J	Rotational inertia [$kg\,m^2$]
k	Thermal conductivity [$W/m\,K$]
K	Controller gain [$-$]
p	Pressure [kPa]
P	Electrical power [kW]
Q	Thermal energy [kJ]
R	Universal gas constant 8.314 [$kJ/kmol\,K$]
T	Temperature [$°C$]
t	Time [s]
U	Overpotential [V]
V	Volume [m^3]
w	Rotational speed [rad/s]
z	Number of transferred electrons [$-$]
γ	Specific heat capacity ratio [$-$]
η	Efficiency [$-$]
ρ	Density [kg/m^3]

1 Introduction

The increasing diffusion of renewable energy sources as a solution for environmental problems like greenhouse gas emissions and pollution has highlighted challenges related to their integration with the existing electricity generation system. These issues are related to the variable, intermittent and sometimes unpredictable nature of the fastest growing renewable power sources: solar and wind energy [1]. In the current situation, the variability of power demand on the grid can still be handled by the traditional grid structure in most of the cases ramping down fossils fueled power plant or turning on natural gas fired peaking plants. In the near future this could not be possible anymore both because pollution concerns and technical limitations of traditional power generation.

A recent study by National Renewable Energy Laboratory estimated the amount of energy storage that is going to be required in the state of California alone to achieve a 50% penetration of photovoltaic generation in its energy mix. The analysis has been performed including the actuation of other measures to increase photovoltaic penetration such as traditional generators increased flexibility, demand response, exports and electric vehicle smart charge. In the most favorable scenario, characterized by high flexibility of the grid generators, up 19 GW of storage capacity would be necessary to achieve 50% of photovoltaic penetration in the California electricity sector alone [2].

Different typologies of energy storage are going to be needed in a future sustainable energy system based on different technologies and different functions. The balancing services that energy storage can provide to the grid include load shifting, peak shaving and voltage regulation.

Energy storage can allow the temporal decoupling of renewable energy production and its final use: electricity can be absorbed when the production exceeds the demand and released when needed, allowing load shifting. Peak shaving refers to the option of cover the short daily periods of demand peak with stored electricity instead of fast ramping natural gas fired power plants while voltage regulation can be achieved by fast responding energy storage solutions to

grid perturbations. An overview of main energy storage option characteristics is presented in Figure 1.

Currently the large majority of worldwide energy storage is provided by pumped hydroelectric systems (PHS), the only mature technology for large scale energy storage. Pumped hydro is a concept based on potential energy in which water is moved between two reservoirs at different altitudes depending on grid needs and energy prices. The other option already available for large scale energy storage based on mechanical energy is the Compressed Air Energy Storage concept in which the compressor and turbine of a traditional gas fired Brayton cycle are decoupled; the air is compressed when excess electricity is available and stored in an underground cavern and its expansion is exploited in the gas turbine when electricity is needed [3]. Both concepts can provide large scale energy storage but are intrinsically geographically constrained by sufficient elevation differences and the presence of suitable underground caverns.

Electrochemical energy storage has grown interest in the last decade as an effective alternative for energy storage at both distributed and centralized level due to the absence of geographical constrains and the good scalability thanks to its modularity nature. Electrochemical energy storage most promising technologies are Lithium-ion batteries and Flow Batteries but their utilization is more suitable for peak shaving and daily load shifting, as well as for grid stability services with discharge time at rated power in the order of hours [4]. Lithium-ion batteries are a fast developing market that is undergoing strong prices decrease, mainly due to the industry scale up related to electric vehicle manufacturing and are already being deployed around the world to provide short term energy storage [5].

Regarding long term energy storage at grid scale level the electrochemical conversion of electricity into hydrogen via water electrolysis, the Power-to-Gas concept, is considered a promising solution to enable a sustainable energy future.
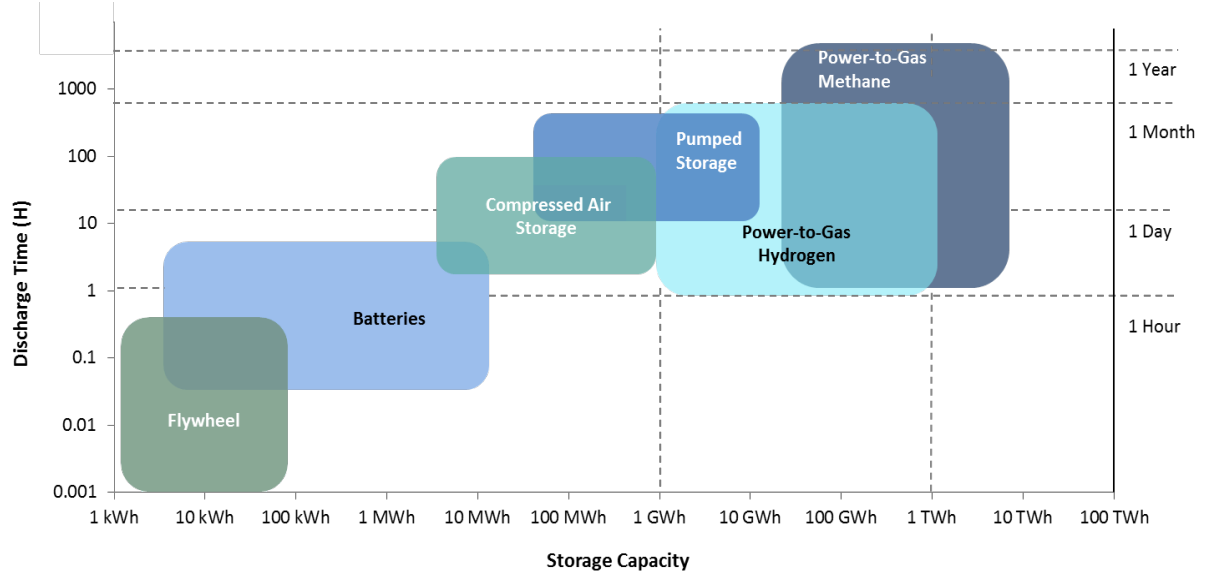
Figure 1. Comparison in terms of energy storage size and discharge time between the main electrical energy storage technologies under investigation [7].

1.1 Power-to-gas

The Power-to-gas concept consists in the electrochemical conversion of electricity into hydrogen, a flexible energy carrier that can allow the interconnection of the electricity sector with the transportation sector, heating sector and industrial sector, contributing to the decarbonization of the entire economy [6]. The renewable hydrogen can be converted back to electric power when needed in a fuel cell or in traditional thermal engines or gas turbines, fed to fuel cell electric vehicles or further converted to other chemicals, both gaseous or liquid, to be used into traditional thermal engines and turbine or as a feedstock in the chemical industry.

Hydrogen has a great potential because of the higher energy density compared to the other energy storage options like battery-based electrochemical energy storage, pumped hydro and compressed air, and can take advantage of the existing natural gas distribution grid as a storage volume. The potential of Power-to-Gas decentralized energy storage capability has been highlighted from the economical point of view compared to Lithium-ion batteries for storage durations from 12 to 35 hours because the efficiency-adjusted capital cost does not depend on the storage size but only on the power output, since this kind of system can be integrated into existing natural gas grid [7]. Hydrogen storage advantages compared to grid scale batteries derive also from the lower manufacturing energy input per unit of stored energy that results, even with lower round-trip efficiencies, in a better performance if the entire life cycle is taken into consideration causing a lower environmental impact [8].

Large scale hydrogen energy storage capability of mitigating fluctuations of large wind power installation has been evaluated dynamically with the integration of large underground salt cavern and compared with compressed air energy storage system; thanks to the higher volumetric density, the use of hydrogen can almost avoid wind energy curtailment allowing both daily and seasonal load shifting, with the advantage of the possible integration with local fuel cell electric vehicles fleets [9].

In the transportation sector hydrogen fueled fuel cell vehicles can provide a clean, zero emission solution for the growing pollution in urban areas but, like plug-in electric vehicles, faces the lack of a widespread refueling infrastructure that can foster the large scale diffusion of this kind of vehicles. There is a growing interest around the world for this solution and car manufacturers like Toyota and Honda already have commercial products. First Element Fuel is a California based company that is developing a network of 18 hydrogen fueling stations across the state, currently fed by only 33% of renewable hydrogen coming from biomethane, soon to become 30 as California Energy Commission recently founded the deployment of 24 more fueling stations [10].

The feasibility of a self-sustainable hydrogen fueling station powered only by renewable energy sources has been already assessed paving the way to decentralized renewable hydrogen delivery system [11].

Regarding alternative uses of hydrogen is under investigation the utilization of renewable hydrogen for the production of ammonia, essential precursor of fertilizers, in areas where the availability of abundant solar and wind energy can bring prices down to compete with traditional production with fossil fuels fertilizer for the agricultural sector. Ammonia could also results as an effective way to store hydrogen [12].

The electrolysis process can be performed with three main technologies: Proton Exchange Membrane Electrolyzers, Alkaline Electrolyzers and Solid Oxide Electrolyzers. Today only the first two technologies present commercial grade solutions and a large number of installation are already in operation while solid oxide electrolyzers are still at the development stage.

1.2 High Temperature Steam electrolysis

High temperature electrolysis can be performed with Solid Oxide Cells, that are solid oxide fuel cell operated in reverse mode. The cell is based on a solid oxide electrolyte that has to be operated at high temperature in order to reach sufficient ionic conductivity. A review of the thermodynamic of electrolysis is provided in the following section.

1.2.1 Thermodynamics

Water electrolysis, showed in Equation (1), is the reaction in which the water molecule is split into its constituents, hydrogen and oxygen. The reaction is endothermic and needs both thermal and electrical energy to be performed.

$$H_2O + Energy \rightarrow H_2 + \frac{1}{2}O_2 \qquad (1)$$
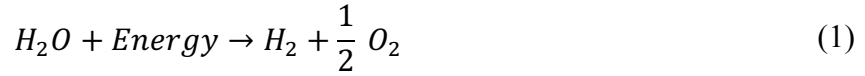
In solid oxide cells the ion that is conducted by the electrolyte is O^{2-}, the ions are transferred from the steam-hydrogen electrode (cathode) to the oxygen-air electrode (anode). The two half reactions are reported in Equation (2) and (3).

$$H_2O + 2e^- \rightarrow H_2 + O^{2-} \qquad Cathode \qquad (2)$$

$$O^{2-} \rightarrow \frac{1}{2}O_2 + 2e^- \qquad Anode \qquad (3)$$
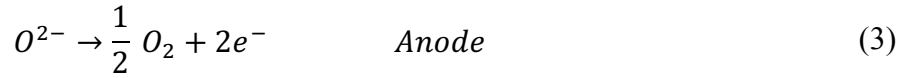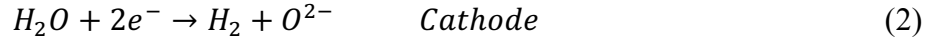
The overall energy demand for water electrolysis ΔH is described by Equation (4) and is composed by two terms: ΔG is the Gibbs free energy change of the reaction and is the part of the energy demand that has to be supplied in form of electrical energy while $T \cdot \Delta S$ represent the thermal energy demand. The dependence of these terms on the temperature is showed in Figure 2.

$$\Delta H = \Delta G + T \cdot \Delta S \qquad (4)$$
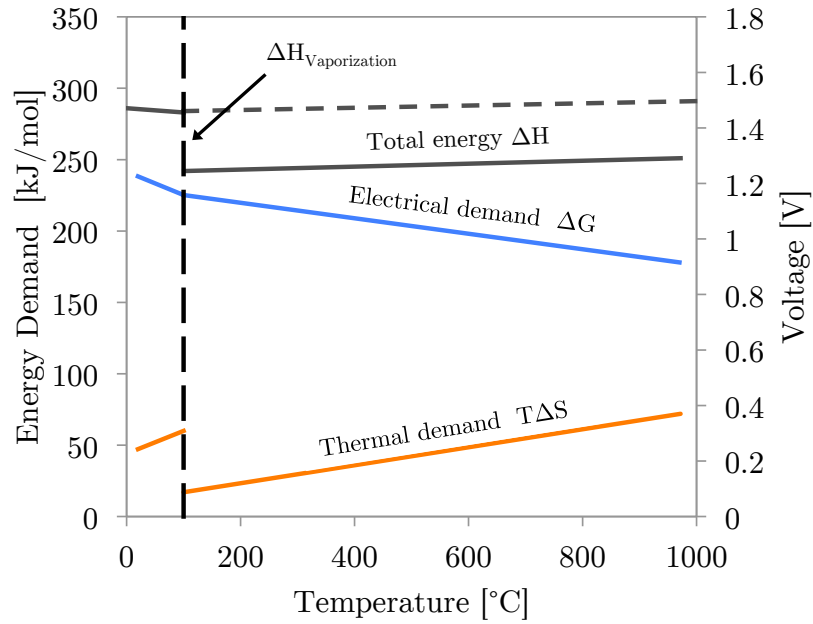
Figure 2. Energy demand for water electrolysis as function of temperature.

The main fact that can be noticed in Figure 2 is that high temperature steam electrolysis intrinsically needs less energy than water electrolysis to be performed, if the energy demand for vaporization is not taken into account. This thermodynamic advantage leads to good opportunity for heat integration with low temperature sources for steam generation. At cell level, where steam electrolysis is performed, while the overall energy demand ΔH slightly increases from ambient temperature to the operating temperature range of solid oxide electrolysis (700 - 900 °C), the electrical demand decreases from being 93 % of energy demand at 100°C to 77% at 750°C.

The reversible voltage is the minimum cell voltage that would be required to perform steam electrolysis and is dependent on the Gibbs free energy change as in Equation (5).

$$V_{Rev} = \frac{\Delta G}{z \cdot F} \qquad (5)$$

Where z is the number of electrons involved in every reaction ($z = 2$) and F is the Faraday constant equal to 96485 C/mol.

The thermoneutral voltage, defined in Equation (6), is the cell operating voltage at which the heat generated by cell internal irreversibilities is enough to provide the heat demand of the electrolysis reaction, resulting in the fact that an ideal cell can be operated in thermal equilibrium at this voltage. In this way, only electrical energy has to be supplied to the cell in order to perform steam electrolysis. The cell thermoneutral voltage is equal to 1.285 V at 750°C

considering only the energy demand for steam electrolysis, meaning that this is the voltage at which the cell operates at thermal equilibrium, i.e. the cell temperature is uniform, and the inlet and outlet temperature of the reactants are the same. If also the energy for steam generation has to be taken into account, the cell operating voltage necessary to cover the tire energy demand would be around 1.5 V.

$$V_{TN} = \frac{\Delta H}{z \cdot F}$$
(6)

The thermoneutral voltage at cell and stack level is important because an electrolysis cell operated at voltage lower than thermoneutral is endothermic and heat needs to be provided to the cell in order to sustain the reaction and keep the cell in the operating temperature range. If a cell is operated at voltages higher than the thermoneutral voltage the cell is exothermic, and the heat generated by irreversibilities, mainly by joule effect, has to be removed from the cell in order to avoid excessive cell overheating.

1.2.2 Literature review

High temperature electrolyzer based on solid oxide cells are still in the development phase, but advancement made in solid oxide fuel cells can be applied also to the reverse operation.

The two main typologies of solid oxide cells are Electrolyte Supported Cells and Cathode Supported Cells. In the electrolyte supported type the electrolyte has also the function of mechanically support the cell and it is thicker (0.1-0.2 mm) compared to the electrode applied to its sides (around 50 μm) and as a consequence need to be operated at higher temperatures, higher than 850°C, otherwise the electrolyte has insufficient ionic conductivity. Cathode supported cells presents thinner electrolyte with thickness in the range 5-20 μm while the steam-hydrogen electrode (cathode in electrolysis mode) gives the mechanical strength to the cell and reach thickness in the range 0.2-1.5 mm. The main consequence of the thinner electrolyte is its lower resistance to ionic conduction that allow the cell to be operated at lower temperature in the range 700 – 800 °C and at higher current densities [13].

The state-of-the-art materials employed for the electrolyte is usually is yttria-stabilized zirconia (YSZ) , a zirconium oxide doped with 8%$_{mol}$ of yttrium to achieve the desired ionic conductivity; the hydrogen electrode is constituted by a cermet of nickel, the catalyst, and YSZ, the ionic conductor material; for the oxygen electrode perovskite materials are considered as lanthanum-strontium-manganite (LSM) for temperature above 800°C and mixed ionic and electronic conductor materials as lanthanum-strontium-cobaltite (LSC) or strontium doped lanthanum ferrite partially cobalt doped (LSCF) for temperature below 800°C [14].

Today the only company offering a commercial prototype based on ESC cells is Sunfire that developed its system as a reversible device that can operate in both electrolysis and fuel cell mode; operation of the system has been proven in in a collaboration with Boeing in Huntington Beach, CA [15] as an energy storage device to reliably support microgrids such as military bases or island energy systems [16]. The same system is going to be deployed soon as part of the European project GrInHy that integrates the solid oxide reversible system into a steel industry [17].

Versa Power System is developing solid oxide cells and stacks since 2012 [18] and latest test performed on cathode supported cell with conventional SOFC materials such as Ni-YSZ cathode, YSZ electrolyte, all ceramic anode at ultra-high current densities up to 6 A/cm^2 shows the potential of cathode supported cells to achieve efficient hydrogen production at high current densities [19].

One of the major problems is related to durability and cell degradation over time that seems to be higher with respect to Solid Oxide Fuel Cells. Degradation can be expressed as the loss of performance over a certain amount of time, usually 1000 hour, referring to the cell voltage in absolute values as mV/1000h or in relative terms as %/1000h. A target for reliable applications would be lower than 1%/1000h. Long term test on solid oxide electrolysis cell and stacks are still not numerous and mostly refers to quite mild operating conditions involving constant current densities lower than 1A/cm2. Long term tests on cathode supported cells have been reported for 9000 hours with degradation rates between 3.8%/1000 h and 1.7%/1000 h [20]. A longer tests has been performed on electrolyte supported cells operated at 0.9 A/cm2 for 23,000 hours showing promising degradation rate of 0.57%/1000 hours [21]. Recent developments regarding the optimization of the microstructure the electrodes of cathode supported electrolysis cells shows very promising degradation rates as low as 0.3-0.4 %/1000 hours but no long term tests have been reported yet [22].

A fact to take into consideration while assessing the effect of degradation on cell performance is that an increase of cell resistance leading to higher overpotentials and lower cell efficiency not necessarily mean a decrease of overall efficiency if the whole system is taken into account. The higher irreversibilities will lead to better heat recovery allowing to maintain the system performance constant in a wide time range.

As previously mentioned one of the main advantages of solid oxide electrolysis is the possibility of improving the electrical efficiency of the process integrating the system with alternative heat sources at both low and high temperature level.

Several previous works at system level focus on the integration of Solid Oxide Electrolyzers with Concentrated Solar Power technologies as source of heat and power. An energy system analysis from DLR explored the possibility of providing both heat and power to a high temperature electrolysis system with a solar tower plant resulting in a Solar-to-Hydrogen

efficiency of the process of 18% [23]. Solar tower technology is also investigated with a CO_2 Brayton cycle as a power generation cycle and high temperature thermal energy storage to achieve non-stop hydrogen production [24]. Different plant layouts have been studied to minimize the impact on a Solar Tower system efficiency of an high temperature electrolysis system, identifying the extraction of steam from the low pressure stage of the Rankine cycle as the less impacting option, with the reduction of the performance penalty of 60% compared to other extraction point considered in the analysis [25]. A Fresnel receivers field coupled with modular thermal energy storage and SOEC system has been investigated to provide a reliable and renewable hydrogen supply to a sustainable fuel cell bus fleet [26].

One of the main aspects that must be taken into account when coupling electrolysis with variable renewable energy sources is the dynamic operation and the control strategies that can be employed to allow such operating condition without compromising cells integrity and system performances. The effect of strong dynamics have been evaluated at cell level and the temperature control via sweep-gas flow manipulation have been investigated [27] and optimized, taking into account the additional power consumption of the air blower but not the overall power consumption or the nature of the heat source necessary to bring inlet streams to the operating temperature [28].

The part-load operation has been also analyzed from a complete system point of view and an operational range of 60-100% of stack load results in high efficiency, above 90%$_{HHV}$, when no external heat source is considered and no control strategy is implemented to extend the working range [22]. When a combination of suitable control strategies is implemented, the electrolysis system can be operated from 10 to 100% of the stack load with an almost flat efficiency curve that remains between 91 and 97%$_{HHV}$ if the low temperature steam comes from a CSP plant [30].

Other alternatives heat sources that have been investigated include geothermal heat [31] and biomass incinerations as renewable sources as well as the integration with nuclear reactors [32].

An additional potential of solid oxide cells that will not be investigated in this work, related to their high temperature of operation and tolerance of nickel catalyst to carbonaceous compounds, is the possibility of the simultaneous co-electrolysis of water and carbon dioxide that can result in an effective way of converting a CO_2 feedstock into syngas or widespread chemical fuel like synthetic methane in the case of further integration with the methanation process [33]. This concept has been investigated for the realization of a closed energy storage system in which the reactants are kept in pressurized vessels and recycled in one direction or the other depending on the availability of excess power or the power demand; such a system could reach a roundtrip efficiency of 74% [34].

1.3 Goal and thesis outline

The University of California, Irvine commitment to a sustainable and carbon neutral future has promoted the implementation of energy efficiency measures and the deployment of on-site renewable energy generation. The UCI campus existing photovoltaic installations are already influencing the microgrid operation and the challenges will increase as additional capacity will be installed to pursue the environmental sustainability pathway.

The goal of the present work is to model a Power-to-gas system based on Solid Oxide Electrolysis and its integration with the existing energy infrastructures of the UCI campus microgrid.

Compared to existing literature works the entire electrolysis system will be modelled dynamically taking into account all the balance of plant components consumptions at full and part load. The Solid Oxide Cells will be modelled with a quasi-3D dynamic model that will allow the investigation of thermal gradients across the cell to assess the feasibility of the operation under strong dynamic conditions. Moreover, the integration of both electrical and thermal energy inputs to the high temperature electrolysis system will be investigated exploiting the photovoltaic excess power and the waste heat from the cogeneration plant of the microgrid.

The present work is structured as follows:

- Chapter 2: the physical dynamic model of the solid oxide cell and of balance of plant components are described in detail. The electrolysis system layout is defined in this section and two control strategies for system and cell temperature control are proposed.
- Chapter 3: the results of steady state and dynamic simulations are presented and discussed in order to compare the system and cell behaviour and performances when different control strategies are implemented.
- Chapter 4: the University of California, Irvine campus microgrid model for the existing power plant and its dispatch is presented in this section. A simplified modular model of the electrolysis system is defined together with two dispatch and integration strategies.
- Chapter 5: the effects of the deployment of increasing photovoltaic capacity on the campus generation mix and microgrid operation are presented and discussed in this section as well as the integration of the solid oxide electrolysis systems.

2 Solid Oxide Electrolysis System: Physical model development

The Solid Oxide Electrolysis system has been modelled starting from the Matlab® tool developed at the National Fuel Cell Research Center (NFCRC) at the University of California, Irvine [35], [36]. The model allows a quasi-3D dynamic representation of fuel cells as well as auxiliary system components like heat exchangers, compressors, valves etc. The main characteristics and assumptions of the model will be described in the following sections.

2.1 Cell and stack

The model represents a Single Repeating Unit (SRU) whose inputs and outputs are multiplied to reach the desired stack size. The cell is modelled in five layers: Cathode side interconnector plate, Steam side (Cathode) flow channels, Positive Electrode-Electrolyte-Negative Electrode (PEN) assembly, Air side (Anode) flow channels and Anode side interconnector plate. Each layer is discretized in control volumes in which the equations for energy and species conservation are implemented. The spatial resolution can be increased increasing the number of nodes.

Each gaseous node control volume is assumed to be a perfectly stirred reactor, temperatures and species concentrations are averaged between inlet and outlet and assumed constant in the node for heat exchange and Nernstian voltage calculations.

2.1.1 Energy conservation

Energy conservation equations for each control volume of the cathode channels, PEN layer, anode channels and interconnector plates are presented in Equations (7)-(10).

$$\rho_{cath} \cdot c_{p_{cath}} \cdot V_{cath} \cdot \frac{dT_{cath}}{dt} = \dot{Q}_T + \dot{H}_{in} - \dot{H}_{out} + \dot{Q}_{ion} - \dot{Q}_{react} \qquad (7)$$

$$\rho_{PEN} \cdot c_{PEN} \cdot V_{PEN} \cdot \frac{dT_{PEN}}{dt} = \dot{Q}_T + \dot{Q}_{GEN} \qquad (8)$$

$$\rho_{an} \cdot c_{p_{an}} \cdot V_{an} \cdot \frac{dT_{an}}{dt} = \dot{Q}_T + \dot{H}_{in} - \dot{H}_{out} - \dot{Q}_{ion} \qquad (9)$$

$$\rho_{plate} \cdot c_{p,plate} \cdot V_{plate} \cdot \frac{dT_{plate}}{dt} = \dot{Q}_T \qquad (10)$$

where $\dot{H}_{in}$ and $\dot{H}_{out}$ are the total enthalpy terms at the inlet and outlet condition of the gaseous nodes, ρ is the density, V is the volume and c, c_p are the specific heat capacity.

$\dot{Q}_{ion}$ is the term related to the sensible enthalpy of the oxygen ions crossing the electrolyte from the cathode to the anode side, evaluated at PEN temperature according to Equation (11).

$$\dot{Q}_{ion} = \frac{I}{4 \cdot F} \cdot h_{O_2} \qquad (11)$$

$\dot{Q}_{GEN}$ is the term related to the heat generated or absorbed by the cell depending on the electrolysis thermodynamic behaviour, evaluated according to Equation (12).

$$\dot{Q}_{GEN} = \dot{Q}_{react} - V \cdot I \qquad (12)$$

Where $\dot{Q}_{react}$ is the heat of the reaction evaluated at PEN temperature with Equation (13), V is the cell voltage and I is the current of the node.

$$\dot{Q}_{react} = \frac{I}{2 \cdot F} \cdot \left(h_{H_2} + \frac{1}{2} h_{O_2} - h_{H_2O} \right) \qquad (13)$$

$\dot{Q}_T$ is the term related to convective and conductive heat transfer between solid-solid, solid-gaseous and gaseous-gaseous interfaces.

$$\dot{Q}_T = \dot{Q}_{cond} + \dot{Q}_{conv} \qquad (14)$$

The conductive heat transfer $\dot{Q}_{cond}$ is evaluated considering uniform surface temperature for both solid and gaseous nodes and the heat exchange surfaces are calculated from geometrical parameters listed in Table 1 and thermal parameter are listed in Table 2.

The convective heat transfer $\dot{Q}_{conv}$ is calculated assuming fully developed flow resulting in a constant Nusselt number, equal to 4 [35], allowing the evaluation of a constant convective heat transfer coefficient with the following equation:

$$Nu = \frac{h_{conv} \cdot D_h}{k} \qquad (15)$$

where h_{conv} is the convective heat transfer coefficient, k is the thermal conductivity of the involved gas and D_h the hydraulic diameter of the cell channel.

Table 1. Geometrical parameters of the cell [35].

Geometrical Parameters		[m]
Cell	Length	0.1
	Width	0.1
Plate 1	Thickness	0.003
	Channel Wall	0.005
	Channel Height	0.002
	Channel Width	0.005
Plate 2	Thickness	0.003
	Channel Wall	0.005
	Channel Height	0.002
	Channel Width	0.005
Cathode	Thickness	800e-6
Anode	Thickness	50e-6
Electrolyte	Thickness	18e-6

Table 2. Thermal properties of materials.

Thermal properties

Electrolyte	Thermal Conductivity	6.19	W/mK
	Density	375	kg/m^3
	Specific Heat	0.8	kJ/kgK
Plates	Thermal Conductivity	5	W/mK
	Density	2000	kg/m^3
	Specific Heat	0.6	kg/m^3
Steam Flow	Thermal conductivity	0.259	W/mK
Air Flow	Thermal conductivity	0.067	W/mK

2.1.2 Species conservation

The nodes related to cathode and anode flows present also species conservation balances needed to take into account the different species concentration along the flow channels. On the cathode side the species are H_2 and H_2O and the species conservation is expressed in Equations (16) and (17), while on the anode side the considered species are O_2 and N_2 according to Equations (18) and (19).

$$\frac{p_{cath} \cdot V_{cath}}{R \cdot T_{cath}} \cdot \frac{d\chi_{H_2}}{dt} = \left(\dot{n}_{cath} \cdot \chi_{H_2}\right)_{in} - \left(\dot{n}_{cath} \cdot \chi_{H_2}\right)_{out} - \frac{I}{2 \cdot F} \tag{16}$$

$$\frac{p_{cath} \cdot V_{cath}}{R \cdot T_{cath}} \cdot \frac{d\chi_{H_2O}}{dt} = \left(\dot{n}_{cath} \cdot \chi_{H_2O}\right)_{in} - \left(\dot{n}_{cath} \cdot \chi_{H_2O}\right)_{out} + \frac{I}{2 \cdot F} \tag{17}$$

$$\frac{p_{an} \cdot V_{an}}{R \cdot T_{an}} \cdot \frac{d\chi_{O_2}}{dt} = \left(\dot{n}_{an} \cdot \chi_{O_2}\right)_{in} - \left(\dot{n}_{an} \cdot \chi_{O_2}\right)_{out} - \frac{I}{4 \cdot F} \tag{18}$$

$$\frac{p_{an} \cdot V_{an}}{R \cdot T_{an}} \cdot \frac{d\chi_{N_2}}{dt} = \left(\dot{n}_{an} \cdot \chi_{N_2}\right)_{in} - \left(\dot{n}_{an} \cdot \chi_{N_2}\right)_{out} \tag{19}$$

where $\dot{n}$ is the total molar flow rate in the anode or cathode channel and χ is the species molar fraction, p, V and T are the pressure, volume and temperature of the respective channel node and R is the universal gas constant. The current is negative, so hydrogen and oxygen are yielded at the cathode and anode side respectively while water steam is depleted at the cathode side.

2.1.3 Polarization

The cell voltage is determined starting from the species concentration in each node with the evaluation of the local Nernst potential according to Equation (20) and (21).

$$U_{NERNST} = U_0 + \frac{R \cdot T_{PEN}}{2 \cdot F} \cdot \ln\left(\sqrt{p_{an}} \cdot \frac{\chi_{H_2} \cdot \sqrt{\chi_{O_2}}}{\chi_{H_2O}}\right) \tag{20}$$

$$U_0 = \frac{-\Delta g_f}{2 \cdot F} \tag{21}$$

where U_0 is the reversible voltage, Δg_f is the molar Gibbs free energy of formation at the PEN nodal temperature T_{PEN} and χ is the species molar fraction.

In this work the cell polarization has been modelled to reproduce the behaviour of recently developed HiPoD Solid Oxide Cells by Versa Power System. The materials used for these cells are conventional SOFC material, the cathode electrode is made of nickel oxide and yttria-stabilized zirconia (YSZ) cathode, the electrolyte is YSZ and the cathode is all ceramic with no noble metals. The cells have a squared geometry and the flow channels of the metallic interconnector plates have a cross flow arrangement [19].

The polarization curves have been acquired for three different operating temperatures of the cell. The curves can be well approximated by linear fittings with an error lower than 5%, as showed in Figure 3, allowing the determination of the Area Specific Resistance values at the three temperatures 700, 750 and 800 °C.
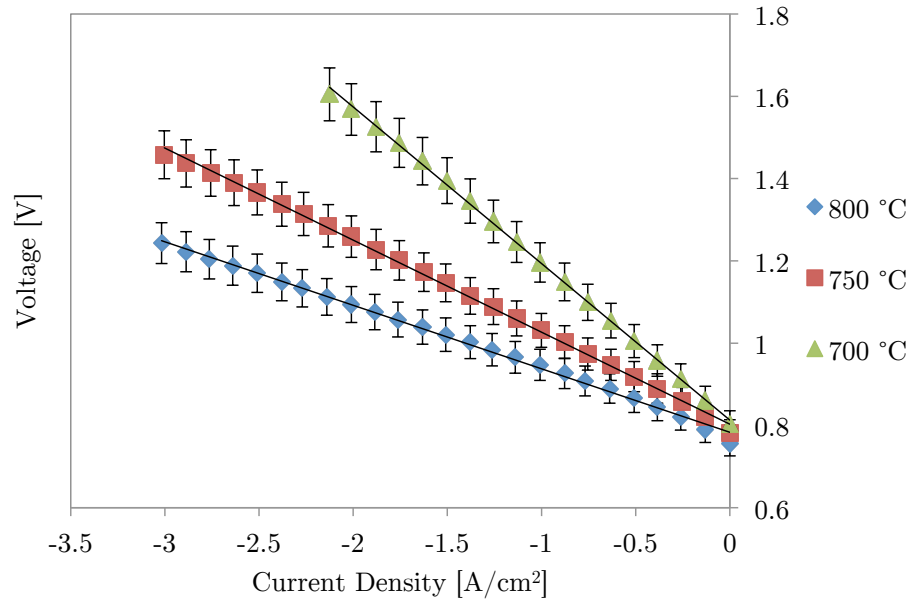
Figure 3. Polarization curves of HiPoD cells from Versa Power Systems [19]
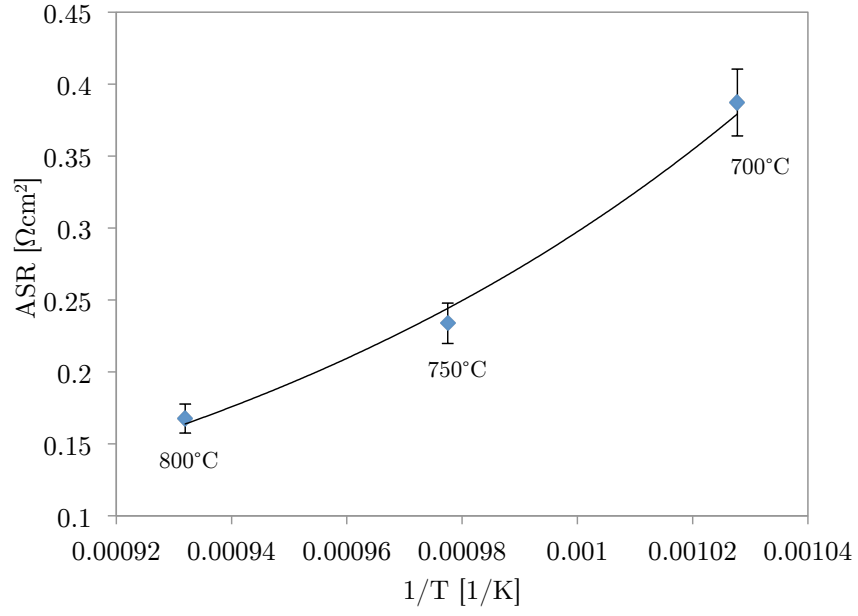
Figure 4. Area Specific Resistance dependence on cell temperature.

The equation for the ohmic resistance of the cell has been derived with an exponential fitting of ASR(T) values, showed in Figure 4, and expressed as Equation (22). A similar approach can be found in many literature works [30], [33], [37] .

$$ASR_{cell} = A \cdot e^{B/T_{cell}} \tag{22}$$

To take into account the increasing resistance due to interconnection of cells to form the stack, a second constant ohmic resistance of $0.1\ \Omega cm^2$ term has been added [38], and the local ohmic overpotentials and cell voltage are evaluated node by node with the following equations:

$$U_{ohmic} = i \cdot ASR_{cell}(T_{PEN}) + i \cdot ASR_{interconnect} \tag{23}$$

$$V_{cell} = U_{NERNST} + U_{ohmic} \tag{24}$$

Parameters relative to the polarization assumptions are listed in Table 3.

Table 3. Cell ohmic resistance parameters.

Area Specific Resistance parameters		
A	4.64462e-5	Ωcm^2
B	8.754e3	K
$ASR_{interconnect}$	0.1	Ωcm^2

2.2 Balance of plant components

In this section the main assumptions and equation relative to the balance of plant components are reported and the main simulation parameters are listed in Table 4.

Table 4. Parameters relative to balance of plant components.

Balance of plant parameters			
Heat exchangers	h_{conv}	50	W/m^2K
Pump	η_{mec}	0.75	-
Compression section	η_{is}	0.75	-
	η_{mec}	0.9	-
	Z_{stage}	1.0015/1.0081	-
	γ_{stage}	1.401/1.412	-
	$p_{compr,in}$	1.01e5/5.5e5	Pa
	$p_{compr,out}$	5.5e5/3e6	Pa
Electric heaters	η_{EH}	0.95	-
Air Blower	η_{Blower}	0.65	-

2.2.1 Heat exchangers

Heat exchangers are modelled as one-dimensional counter flow plate heat exchangers represented by three layer of control volumes: hot flow, metal separator plate and cold flow. The heat exchanger is assumed to be adiabatic with respect to the ambient and the convective heat transfer coefficient between the plate and the flows is assumed to be constant. In each node energy and mass conservation equations are implemented according to Equation (25) for gaseous control volumes and to Equation (26) for the metal plate.

$$\frac{V_{h,c} \cdot p_{h,c}}{T_{h,c} \cdot R} \cdot c_{p_{h,c}} \cdot \frac{dT_{h,c}}{dt} = \dot{Q}_T + \dot{H}_{in_{h,c}} - \dot{H}_{out_{h,c}} \tag{25}$$

$$\rho_{plate} \cdot c_{plate} \cdot V_{plate} \cdot \frac{dT_{plate}}{dt} = \dot{Q}_T \tag{26}$$

where the term $\dot{Q}_T$ is the term of convective heat transfer between solid and gaseous nodes, ρ is the density, V is the volume and c, c_p are the specific heat capacity of gaseous and solid nodes.

2.2.2 Electric heaters

Electric heaters are needed to supply additional heat to the flow at both high and low temperature level. Their energy consumption has been taken into account as the obtained enthalpy increase of the flow according to Equation (27) and the efficiency is assumed to remain constant during dynamic operation.

$$P_{EH} = \frac{\dot{H}_{out} - \dot{H}_{in}}{\eta_{EH}} \tag{27}$$

where $\dot{H}$ is the total enthalpy at the inlet and outlet condition and η_{EH} is the efficiency of the electric heater.

2.2.3 Pump

A pump is necessary to feed water to the system overcoming the pressure drops on the water side. Its electric power consumption is evaluated assuming a constant pump efficiency with Equation (28).

$$P_{Pump} = \frac{\dot{m}_{water} \cdot (p_{out} - p_{in})}{\eta_{Pump}} \tag{28}$$

where $\dot{m}_{water}$ is the mass flow rate, p_{out} is the outlet pressure needed, p_{in} is inlet pressure assumed to be the atmospheric pressure and η_{Pump} is the pump efficiency.

2.2.4 Air blower

On the air side a blower is necessary to overcome system pressure drops especially when the system control manipulate the air flow to control stack temperature variations. For this reason the dynamic shaft torque balance is used to model the blower inertia [39]–[41] :

$$J \cdot w \cdot \frac{dw}{dt} = P_{Blower} - P_{Impeller} \tag{29}$$

where w is the rotational speed, J is the moment of inertia, P_{Blower} is the electric power supplied to the blower and $P_{Impeller}$ is the blower work evaluated according to Equation (30) assuming a constant blower efficiency.

$$P_{Impeller} = \frac{\dot{V}_{air} \cdot (p_{out} - p_{amb})}{\eta_{Blower}} \tag{30}$$

Where $\dot{V}_{air}$ is the volumetric flow rate, p_{out} the required outlet pressure and η_{Blower} the mechanical efficiency.

2.2.5 Compression section

The hydrogen compression section has been modelled as a multi-stage isentropic compressor as proposed in other works [38][42]. The outlet pressure is set to 30 bar, a suitable pressure for grid injection. Two compressor stages have been considered and modelled with Equations (31) and (32), assuming constant isentropic and mechanical efficiency [37].

$$P_{Compr} = \dot{n}_{H_2} \cdot \left(T_{Compr,out} - T_{Compr,in}\right) \cdot \frac{R}{\eta_{mec}} \cdot \sum_{stage} Z_{stage} \cdot \frac{\gamma_{stage}}{\gamma_{stage} - 1} \tag{31}$$

$$T_{Compr,out} = T_{Compr,in} \cdot \left(1 + \frac{\left(p_{compr,out}/p_{compr,in}\right)^{\frac{\gamma_{stage}-1}{\gamma_{stage}}} - 1}{\eta_{is}}\right) \tag{32}$$

where P_{Compr} is the electrical power consumption of the compression section, $T_{Compr,out}$ is the temperature at the compressor outlet, $T_{Compr,in}$ is the temperature at the compressor stage inlet, $\dot{N}_{H_2}$ is the molar flow rate of hydrogen, γ_{stage} is the average heat capacity ratio of each stage, Z_{stage} the average compressibility factor of hydrogen in each stage and $p_{compr,in}, p_{compr,out}$ are the inlet and outlet pressures of the compressor stage.

2.3 System layout

The system configuration has been developed to realize a stand-alone electrolysis system where the only energy input is electrical energy. Two inlet streams are present, the water stream and the ambient air stream. The system layout is showed in Figure 5.
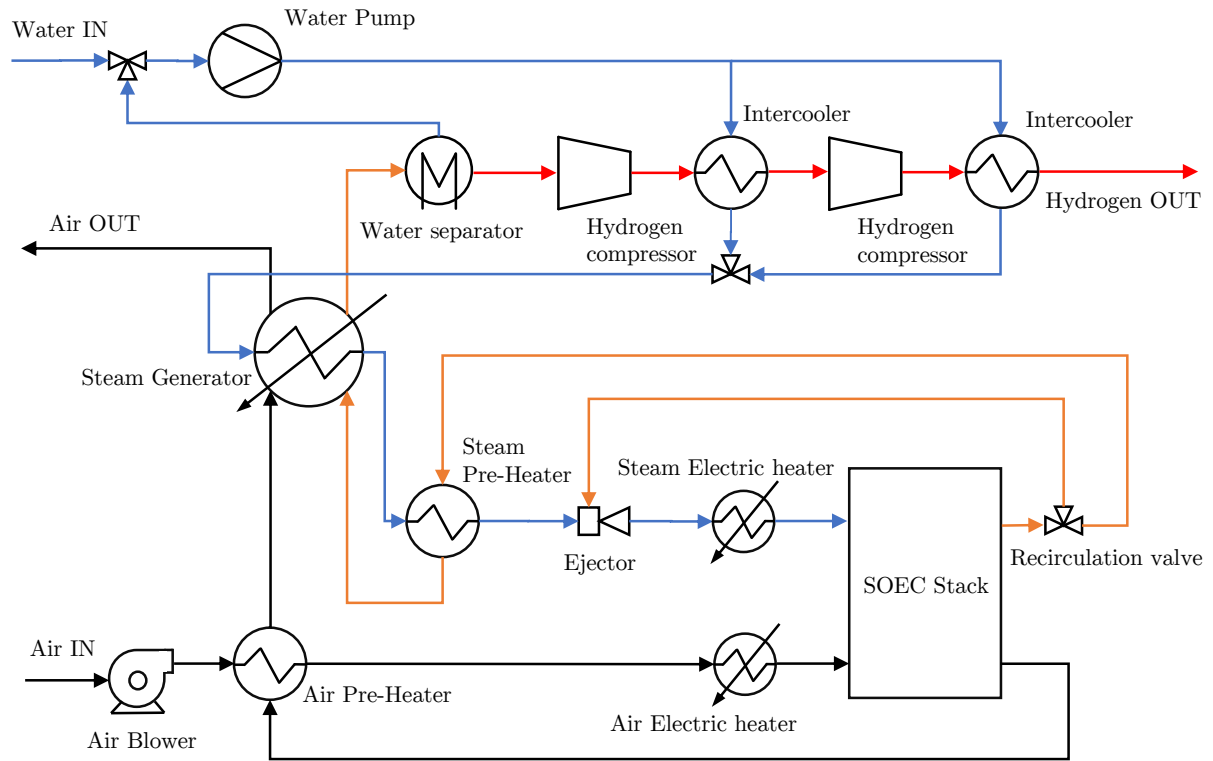
Figure 5. SOEC system layout.

Water is fed to the system by a pump to provide sufficient head to overcome system pressure drops and assumed to enter the system at 15 °C. Feed water is pre-heated to 100°C by the two intercooling stages of the hydrogen compression section. Evaporation is then carried out recovering heat from both stack outlet flows and completed by an electric steam generator. The steam is further pre-heated in a counter flow heat exchanger with the outlet hydrogen rich flow and then mixed with the hydrogen rich recirculated flow entrained by the recirculation ejector in order to obtain the required cathode inlet composition with 10% H_2 molar concentration [37]. The final super-heating necessary to bring the steam to the required stack inlet temperature is performed by the steam side electric heater. After the passage through the stack channels, where the electrochemical conversion of steam into hydrogen takes place, a recirculation valve allows to split the outlet hydrogen rich mixture for partial recirculation. The main stream is then cooled

down by the counter flow heat exchanger and steam generator in order to recover its thermal energy. Additional cooling below 60°C is performed in the water separator and the water is recirculated into the feed water flow. The pure hydrogen flow is then sent to the two-stage compression section with intercooling to reach a final outlet pressure of 30 bar adequate for natural gas pipeline injection.

On the sweep-gas side, ambient air is fed to the system by a blower, pre-heated by a counter-flow heat exchanger with the stack anode outlet and further heated to the required stack inlet temperature by an electric heater. Crossing the stack, the flow is enriched by oxygen coming from the cathode side and then is used to pre-heat the entering air and contribute to the steam generation before being discharge to the environment.

Once the system configuration has been defined, the system performance can be assessed evaluating a system efficiency based on the lower heating value of hydrogen as showed in Equation (33).

$$\eta_{System} = \frac{\dot{n}_{H_2} \cdot LHV_{H_2}}{P_{Stack} + P_{EH,air} + P_{EH,steam} + P_{Steam\,gen} + P_{Pump} + P_{Blower} + P_{Compr}} \tag{33}$$

where $\dot{n}_{H_2}$ is the molar flow rate of hydrogen at the outlet of the system, LHV_{H_2} is the lower heating value of hydrogen and P is the electric consumption of stack and balance of plant components.

2.4 System control

The electrolysis system is controlled by the electric power supplied to the stack. At every time step the current that can be imposed to each cell is computed as follow:

$$I = \frac{P_{stack}}{V_{cell} \cdot n_{cells}} \tag{34}$$

where P_{stack} is the electric power supplied to the stack, V_{cell} is the voltage of the cells and n_{cells} is the number of cells in the stack. The water feed necessary to the system is determined and consequently modulated as inlet stream to the system model via the Faraday's Law of electrolysis:

$$\dot{N}_{H_2O} = \frac{I}{2 \cdot F} \cdot \frac{n_{cells}}{SU} \tag{35}$$

where *SU* is the steam utilization factor defined as the ratio between the stoichiometric steam flow necessary to perform the electrolysis process at a given current and the inlet steam flow supplied to the system.

2.4.1 Temperature control

Cell temperature control is one of the key issues involved in the dynamic operation of high temperature solid oxide systems. In this work the temperature control is performed via the manipulation of the air flow at the anode side, in this way the air flow has two functions: removing the oxygen produced by the electrolysis process and provide active cooling or heating to the stack. Two different control strategies have been implemented as PI (Proportional-Integral) feedback controls to simulate the system response to power source perturbations typical of VRES.

The controller calculates an error $e(t)$ between a control variable and its desired set point and applies a correction based on a term proportional to the error and one to the integration of the error over time. The general controller correction $u(t)$ can be represented by Equation (36).

$$u(t) = K_P \cdot e(t) + K_I \cdot \int_0^t e(t') \cdot dt' \tag{36}$$

where K_P is the proportional gain and K_I is the integral gain.

2.4.1.1 Constant PEN average temperature

The target of this control strategy is to keep the average operating temperature of the cell equal to 750 °C. The controller will react to temperature variation manipulating the inlet air flow via the power consumption of the blower and the air inlet temperature to the stack changing the outlet temperature of the high temperature air electric heater. The control strategy scheme is showed in Figure 6 and the implemented parameters are summarized in Table 5.

The error from the set point of the cell temperature is evaluated every time step according to Equation (37).

$$e(t) = T_{PEN,avg}(t) - T_{PEN,SP} \tag{37}$$

where $T_{PEN,avg}$ is the average temperature of the PEN layer and $T_{PEN,SP}$ is the set point temperature. When the cell temperature is lower than the set point value, airflow and inlet

temperature are increased to supply heat to the stack while if it is higher the airflow is increased and the air inlet temperature is decreased.

Figure 6. Scheme of constant PEN average temperature control strategy.

Table 5. Summary of constant PEN temperature control strategy parameters.

Constant PEN temperature control parameters

Cell temperature set point	750	°C
Blower minimum power	0.5	kW
K_P	2.5e3	-
K_I	2.5e2	-
Air inlet temperature range	650-750	°C
K_P	1.5e2	-
K_I	8.5e2	-

2.4.1.2 Constant air inlet temperature

This control strategy has been elaborated after the evaluation of the results of the previous control strategy in term of thermal gradient on the cell and performance at system level.

This simpler control approach consists in keeping the air inlet temperature and volumetric flow constant in a wide range of operating conditions. In this way the cell average temperature will vary between a maximum and minimum set point values. When the difference between air outlet temperature from the cell and air inlet temperature reaches one of the set points, the air

flow is increased in order to cool or heat the cell to keep the cell operating temperature inside the required safety range. The control strategy scheme is showed in Figure 7 and the implemented parameters are summarized in Table 6.

The error is evaluated at every time step only when the temperature difference between the anode inlet and outlet is higher than the set point value, according to Equation (38).

$$e(t) = \frac{\Delta T_{air}(t) - \Delta T_{air,SP}(t)}{\Delta T_{air,SP}} \tag{38}$$

Where ΔT_{air} is the difference between the temperature measured at the outlet of the cell and the inlet temperature and $\Delta T_{air,SP}$ is the set point value of the temperature increase or decrease. When the cell is operated over the thermoneutral voltage the outlet temperature will be higher than the inlet while, when operated below the thermoneutral voltage the outlet temperature will be lower.
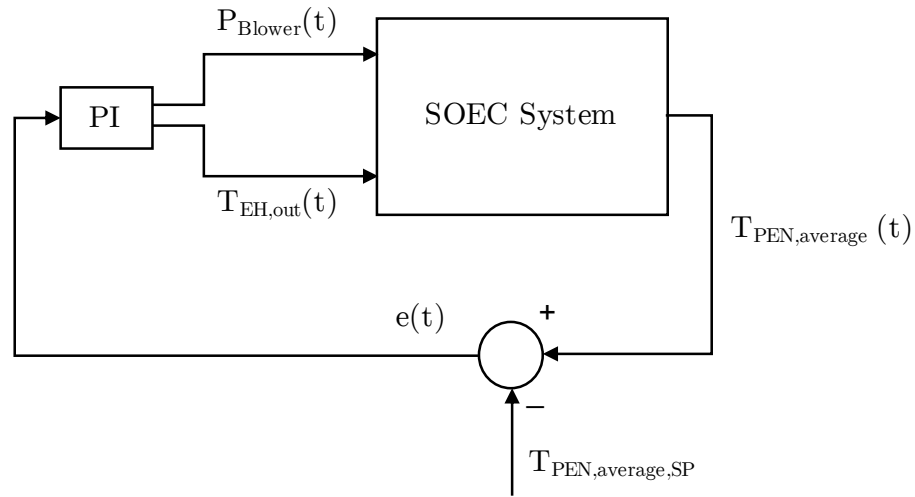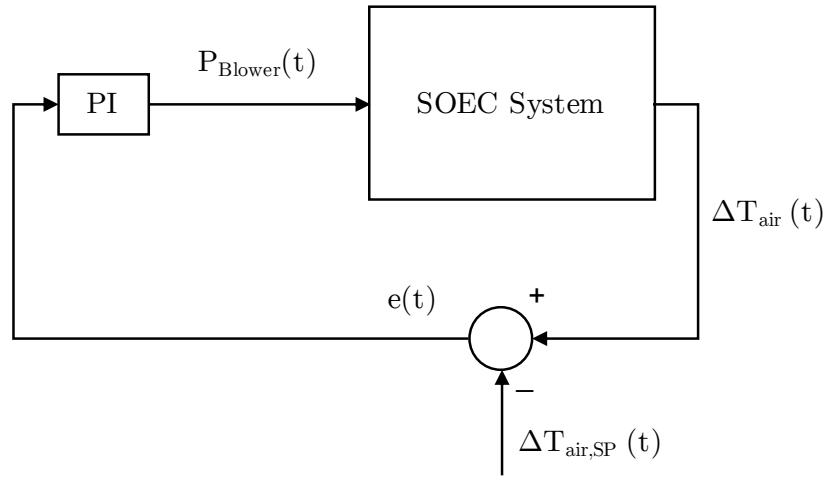

Figure 7. Scheme of constant air inlet temperatue control strategy.

Table 6. Summary of constant inlet air temperature control strategy parameters.

Constant air inlet temperature control parameters

ΔT anode air	45	°C
Blower minimum power	0.5	kW
K_P	1	-
K_I	30	-
Air inlet temperature	750	°C

3 Solid Oxide Electrolysis System: Results

3.1 Steady State results

The model has been used to characterize the performance and operating parameters in a sequence of steady state. The modelled stack is made of 2500 cells in series and absorbs 300 kW at the thermoneutral voltage of 1.285 V. The driver of the system is the electric power supplied to the stack that has been varied in the range 60-480 kW and the energy consumption of the complete system has been determined as a consequence.

The operating range has been determined for different reasons that will be further explained in this section:

- In the case of constant PEN temperature control, at the maximum stack load, since the cell voltage is high, the stack efficiency decreases, and the system efficiency drops to PEM or Alkaline electrolysis levels.
- In the case of constant inlet air temperature control, the cell temperature reaches the upper and lower threshold and the system efficiency start to decrease.

The steam utilization factor of the system has been set to 85% to avoid the generation and heating of excessive steam flows in a stand-alone configuration that would result in lower system efficiencies [43], that results slightly higher than the stack utilization, since a partial recirculation of the cathode side is performed. Steady state results are presented for the two developed control strategies. The result reported here refers to a cross-flow configuration of cathode and anode flow cannels.

Table 7. Summary of SOEC system simulation parameters.

Simulation parameters		
SU$_{System}$	0.85	-
Steam inlet T	750	°C
Stack load	60-480	kW

3.1.1 Cell

The first difference between the two control approaches can be clearly seen in the resulting polarization curves representing the cell working points (Figure 8). When the average temperature of the cell is kept constant the relation between average current density and cell voltage reflect the linear ohmic loss behaviour implemented in the model (Section 2.1.3). In the case in which the cell temperature can vary, the resulting polarization curve is different: increasing the imposed current density from the minimum value, the first section shows a linear trend since the cell is working in strong endothermicity and the temperature is kept constant by the hotter airflow; moving to higher current densities the cell temperature start to increase causing the gradual decrease of the ohmic resistance from 0.48 to 0.26 Ωcm^2 and resulting in the lower slope of the polarization curve. When the cell reaches the maximum allowable temperature the cell temperature is kept constant by the cooler airflow and the polarization curve shows again the linear trend. The lower voltage value of the constant temperature cell for
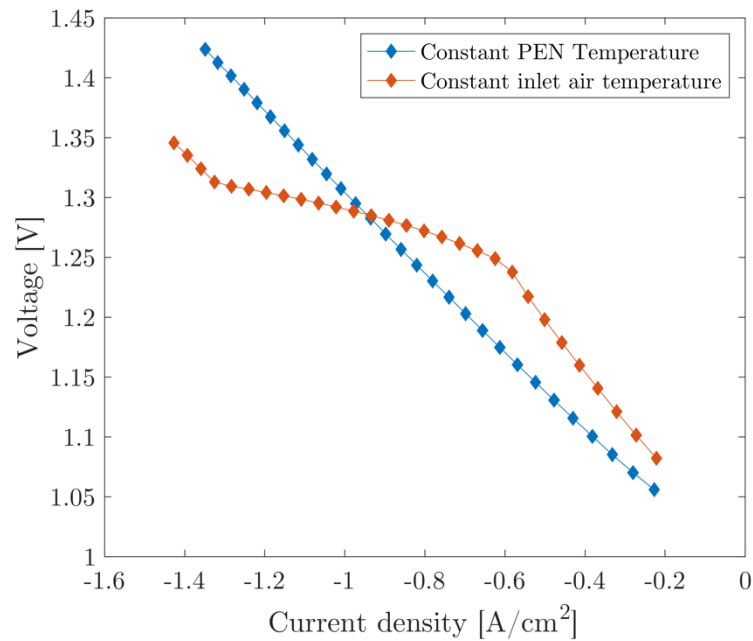
Figure 8. Working polarization curves resulting from the two different control strategies.

working points below the thermoneutral voltage is due to the lower cell ASR at higher temperature and higher dilution of anode side resulting in lower Nernstian voltages.

It can be stated that the stack electrical efficiency is lower for the system operated at variable cell temperature for all the operating condition below thermoneutral voltage compared to the stack operated at constant temperature but from the system level, as will be investigated in the next section, this advantage is negligible compared to the additional auxiliary consumption.

Representative cases of steady state spatial distribution of reacting species across the cell are showed in Figure 9-10-11. On the graphs the flow direction of the cathode side is from left to right while, given the cross-flow configuration, the anode side flow direction is from bottom to top.

As a result, it can be observed in Figure 9 the steam concentration inside the cathode channels decrease along the horizontal direction as it is converted into hydrogen with a slight dependence on the vertical position as a consequence of different current densities as will be explained in this section. In Figure 10 the complementary behaviour can be observed as the molar concentration of hydrogen increase from left to right reaching outlet concentration around 80%. The inlet values on the left side of both figures reflect the desired cathode inlet flow composition of 10% H_2-90% H_2O, achieved via partial recirculation of the cathode outlet. The spatial distribution of cathode side species concentration is very similar to the reported ones in all the steady states at different cell load as a consequence of the constant steam utilization factor.
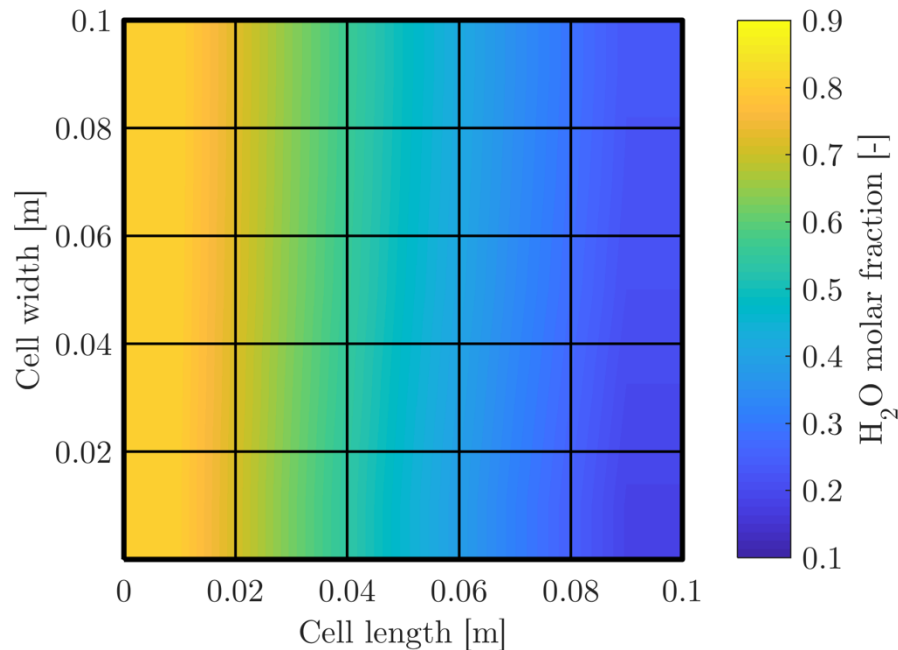
Figure 9. Typical steam molar concentration across the cell on the cathode side.
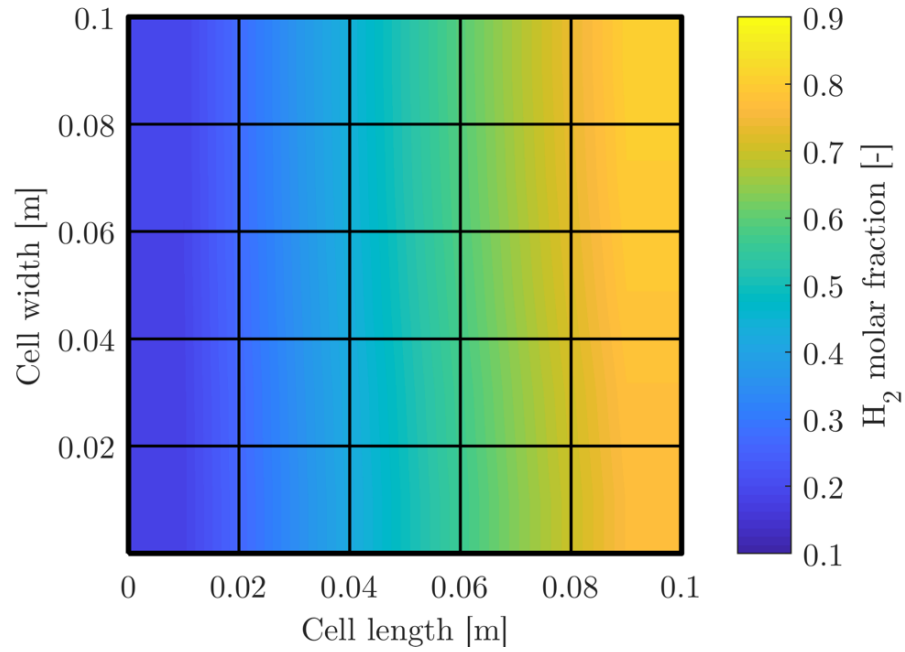
Figure 10. Typical hydrogen molar concentration across the cell on the cathode side .

The anode side concentration of oxygen is reported in Figure 12 for an operating condition around the thermoneutral voltage. In this case the air flow rate reaches the minimum because is not needed for heat management. As a consequence, the anode flow is less diluted and the highest gradients in oxygen concentration along the anode channels can be observed. The inlet concentration reflects the ambient air oxygen concentration of 21% and the outlet average concentration reaches values higher than 30%. In cases where airflow is manipulated by the controller for thermal management the increase in molar concentration of oxygen on the anode channels is almost negligible.

The oxygen concentration slightly affects the Nernstian voltage spatial distribution, showed in Figure 11, that is instead strongly influenced by the steam and hydrogen concentration on the cathode side. The resulting Nernstian voltage increase from values around 0.89 V on the cathode inlet side, where the reactant concentration is highest, to values higher than 1 V closer to the cathode outlet where the reaction product concentration is highest.
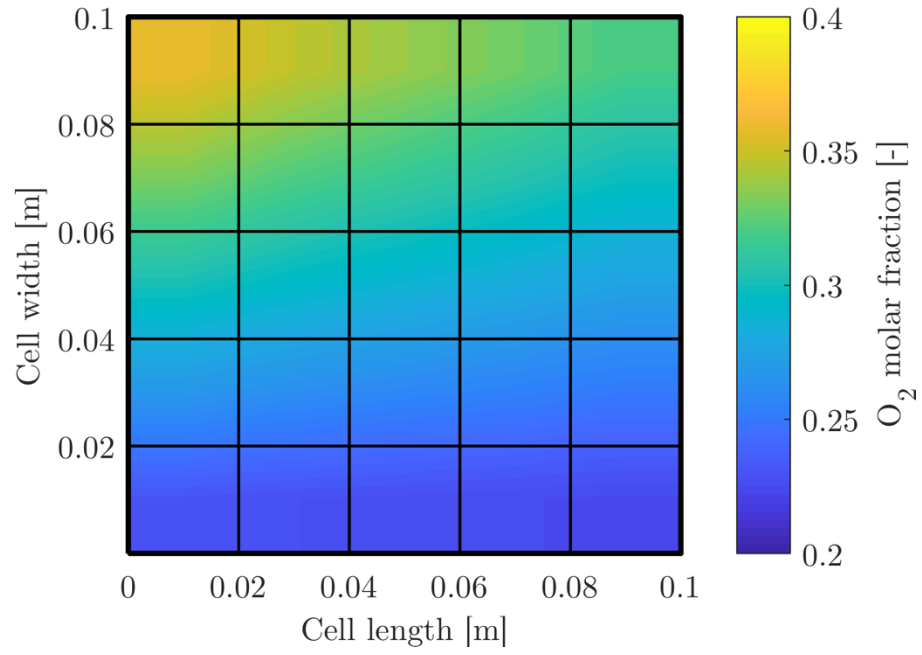
Figure 12. Oxygen molar concentration on the anode side in the case of minimum airflow.
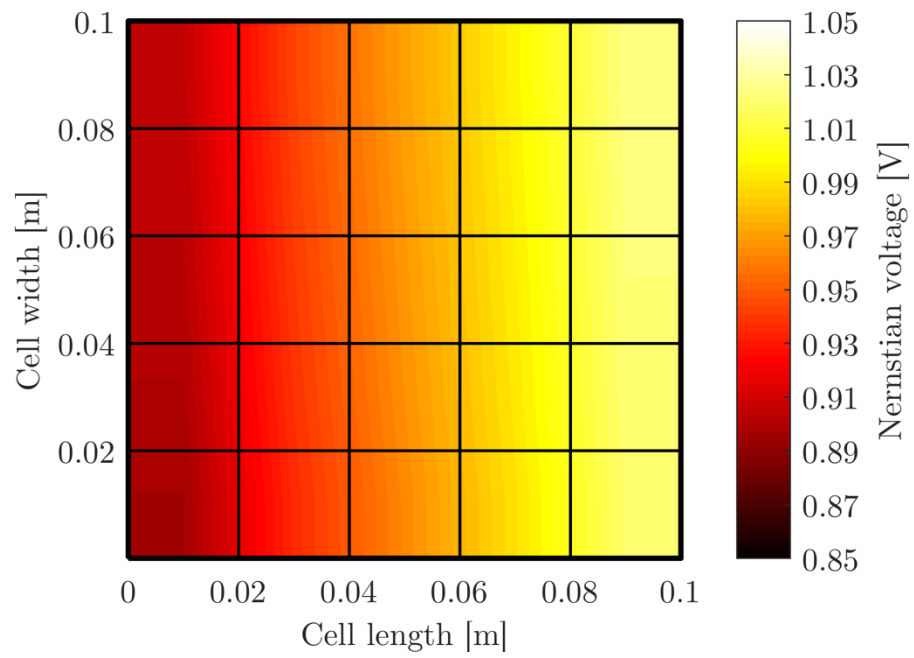
Figure 11. Typical spatial distribution of the Nernst voltage across the cell.

The direct consequence of the Nernstian voltage distribution is that, since the cell is an equipotential surface, the current density that is possible to impose to the cell shows a complementary pattern. Where the Nernstian voltage is lower, at a given cell voltage, the current density is higher, the overpotential are higher and more hydrogen is produced. This is not the only factor that influence the current density because of the dependence of the cell voltage on the temperature. While the Nernstian voltage distribution is similar in every working condition at steady state the temperature distribution strongly depend on the working condition and the system control strategy implemented.

Representative spatial temperature distributions are showed in Figure 13 and Figure 15. The two figure refers both to the maximum cell load that, depending on the control strategy implemented correspond to $i_{avg} = 1.34\ A/cm^2$ and $V_{cell} = 1.42\ V$ for the constant average cell temperature control strategy and $i_{avg} = 1.42\ A/cm^2$ and $V_{cell} = 1.34\ V$ for the constant air inlet temperature control strategy. As will be explained in this section this is the operating condition that causes the highest temperature gradients across the cell.

As showed in Figure 13 the spatial temperature distribution in exothermic conditions reflect the direction of the cooling anode air flow. The temperature is lowest on the bottom side of the graph, around 733°C close to the air inlet side, and highest on the top left corner where reaches 766°C. The center of the cell is, as expected, at 750 °C. The temperature distribution on the horizontal direction of the graph can be explained overlapping the current density spatial distribution showed in Figure 14.

The current density distribution reflects both temperature and Nernstian voltage distribution; as can be observed, it decreases from the left to right as the molar concentration of steam decreases and the hydrogen concentration increase (Figure 9-10-11). The current density presents a maximum in the upper left corner where the temperature is highest and, as previously explained, the electrolyte resistance is lowest. The symmetrical behaviour is present on the lower right corner where the temperature is lowest. These two facts are interconnected because the temperature is dependent on the heat generated by irreversibilities that increase as the current increase.

Figure 13. Spatial temperature distribution of the PEN layer at maximum cell load if constant average cell temperature control is implemented.

F**igure 14.** Spatial distribution of the current density at maximum cell load if the constant average cell teperature control is implemented.

The temperature distribution at maximum cell load in the case of constant air inlet temperature is showed in Figure 15. The temperature distribution is more uniform compared to the previous case and the overall temperature reaches values higher than 780°C. In this case the maximum temperature is on the top left corner and is 797°C since both the steam flow and airflow inlet temperatures are 750°C, so the cell temperature increases from bottom to top of the graph and from left to right. The minimum temperature is 779°C resulting in a maximum temperature difference across the cell of 18°C.

As a consequence of the overall lower cell resistance due to the higher temperatures and lower temperature gradients compared to the other control strategy the current density distribution showed in Figure 16 reflects more the distribution due to the reactant concentration. The current density is highest on the left side where the highest molar concentrations of steam are and gradually decreases toward right as the concentration of hydrogen increase.
When this second control strategy is applied also the difference between the maximum and minimum local current density is lower as the current density ranges from 1.19 to 1.69 A/cm^2 while in the previous case it ranges from 1.08 to 1.69 A/cm^2.

As expected the better performance in term of current densities at given cell power will lead to better overall performance in term of hydrogen production.
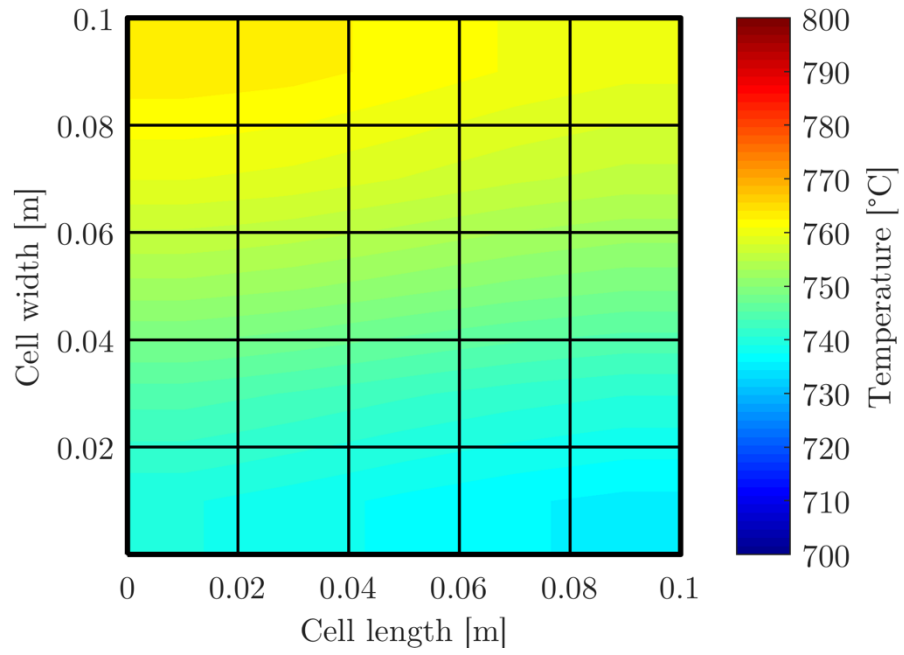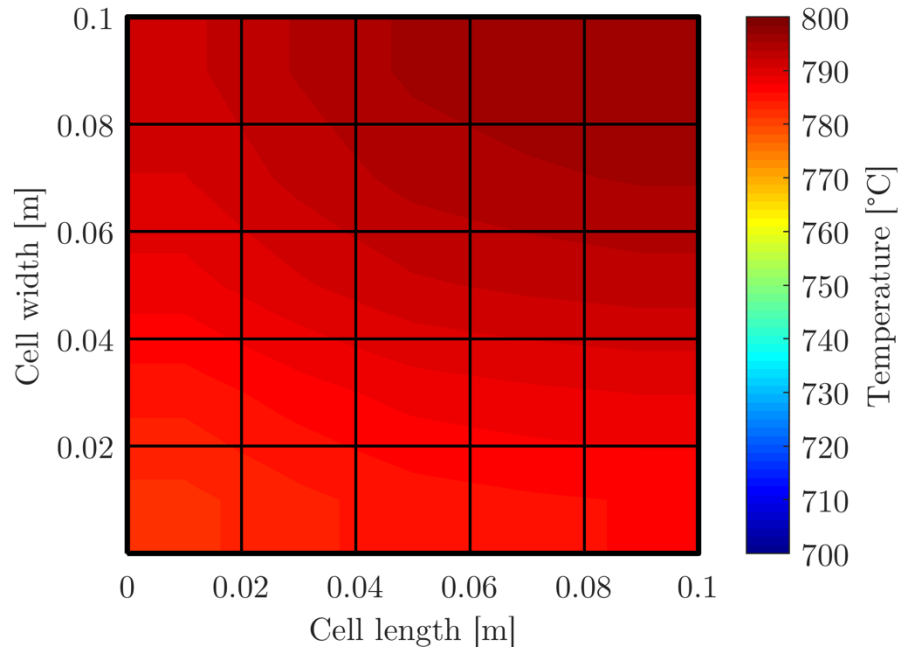
Figure 15. Spatial temperature distribution of the PEN layer at maximum stack load if constant inlet air temperature control is implemented.
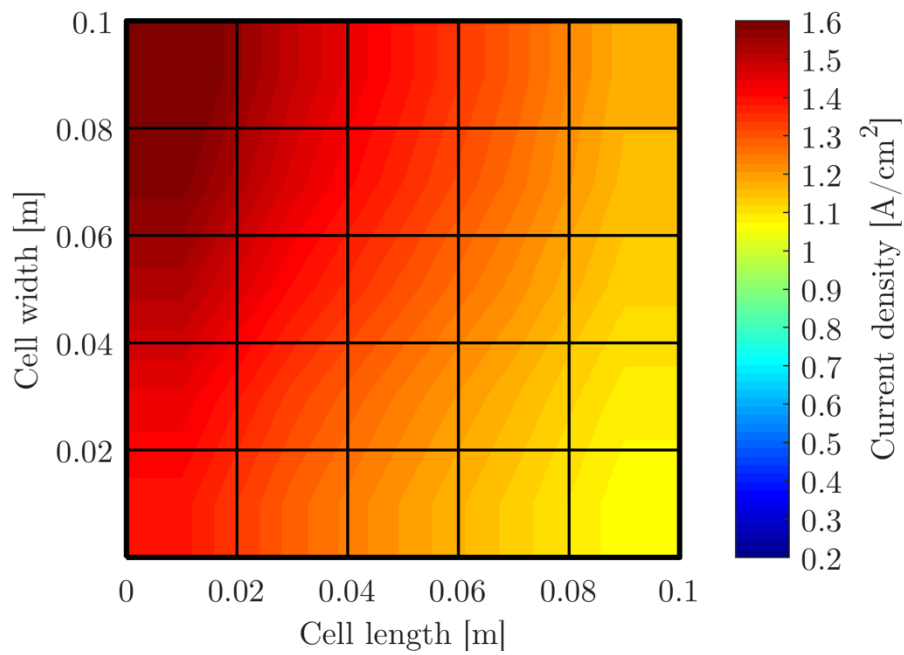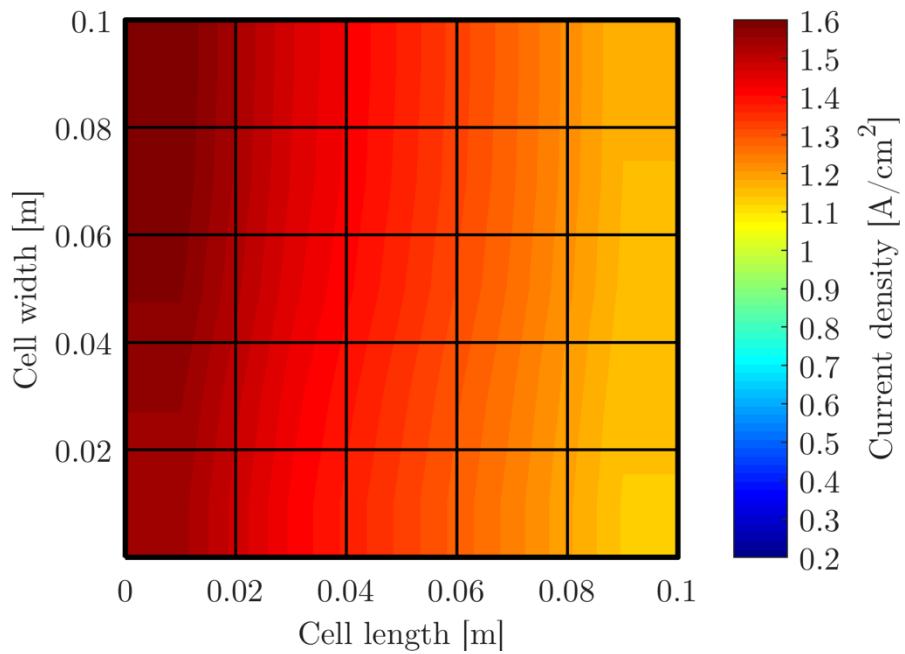

Figure 16. Spatial distribution of the current density at maximum cell load if the constant inlet air temperature control is implemented.

The synthesis of the cell temperatures behaviour as a function of the stack load is showed in Figure 17 comparing the effects of the two control strategies. The common point is when the stack is operated at the thermoneutral voltage: in both cases the average cell temperature is 750°C and there are almost no temperature gradients along the cell in steady state conditions.
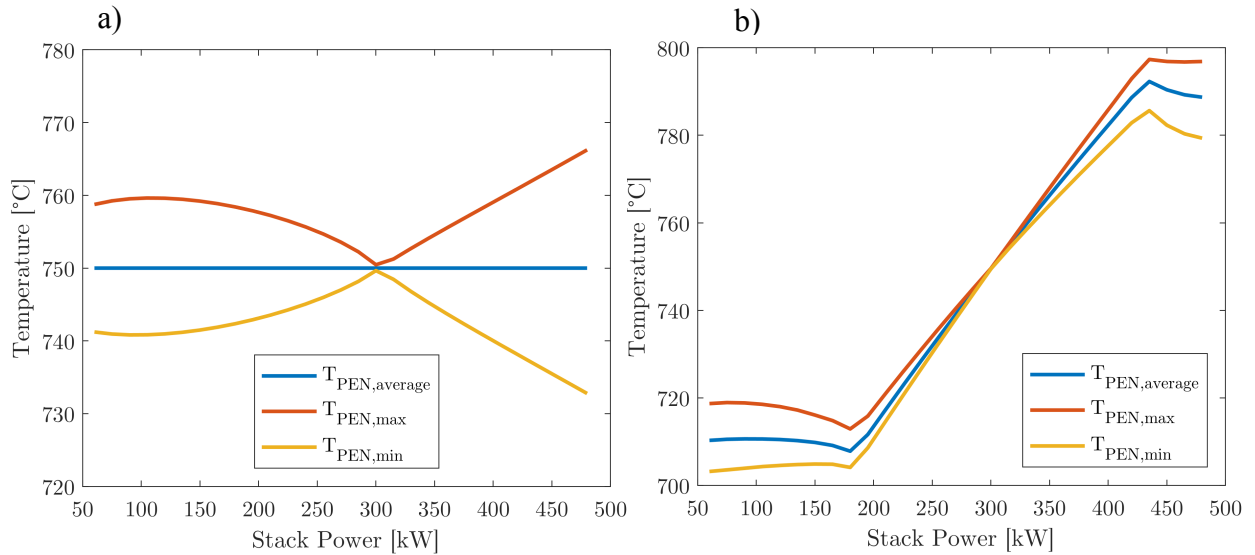
Figure 17. Cell temperatures at different stack loads when the two control strategies are implemented: a) Constant average temperature , b) Constant inlet temperature.

When the aim of the control strategy is keeping the average temperature constant, left figure, the variation of air inlet temperature is immediately reflected in temperature differences between the hottest and coldest point of the cell. The maximum temperature difference in steady state condition is 33°C at the maximum stack load, while in strong endothermic condition is 19°C. In both conditions the cell operate well below the safety threshold of 100°C temperature difference along the cell [27].

If the second control strategy is implemented the airflow is not manipulated until the air outlet temperature reaches 705 or 795°C to conservatively keep the overall cell temperature oscillation below 100°C. As a consequence, the results show that temperature gradient are very low in the uncontrolled range and only when the airflow increases to keep the average temperature constant, the temperature differences increase reaching 15°C and 18°C respectively at minimum and maximum operating load. It can be noticed than after the air outlet temperature reach the upper or lower limit the temperature difference across the cell start to increase as a consequence of the increased air flow. The second control strategy results in milder cell condition regarding thermal gradients across the cell suggesting that stack durability could be improved adopting it. Nevertheless, even when the cell temperature is kept constant the

resulting thermal gradients are much lower than the gradients that are considered acceptable for Solid Oxide Cell materials.

3.1.2 System

In the constant cell temperature control case, showed in Figure 18, the main consumer components are the stack and the air electric heater that together account for more than 80% of consumption in all operating condition. As can be noticed when the stack load is equal to 300 kW the stack is at the thermoneutral condition i.e. the voltage is 1.285 V. In the condition the system works at the best condition because the balance of plant components consumption is at its minimum allowing to reach the highest system efficiency. All the other working points present a strong increase of auxiliary components especially the blower consumption and the air electric heater consumption. The latest strongly increase when the stack operates below thermoneutral voltage because both air flow and inlet temperature to the stack are increased to maintain the constant cell temperature.

The electric steam generator contribution in very low, around 1%, in almost every working condition because a large airflow is involved in the temperature control and therefore effective heat recovery at evaporation temperature can be performed. When the system operates around thermoneutral condition the heating/cooling need decreases consistently, less heat can be recovered at lower temperature and the steam generation consumption reaches 10% of total consumption.
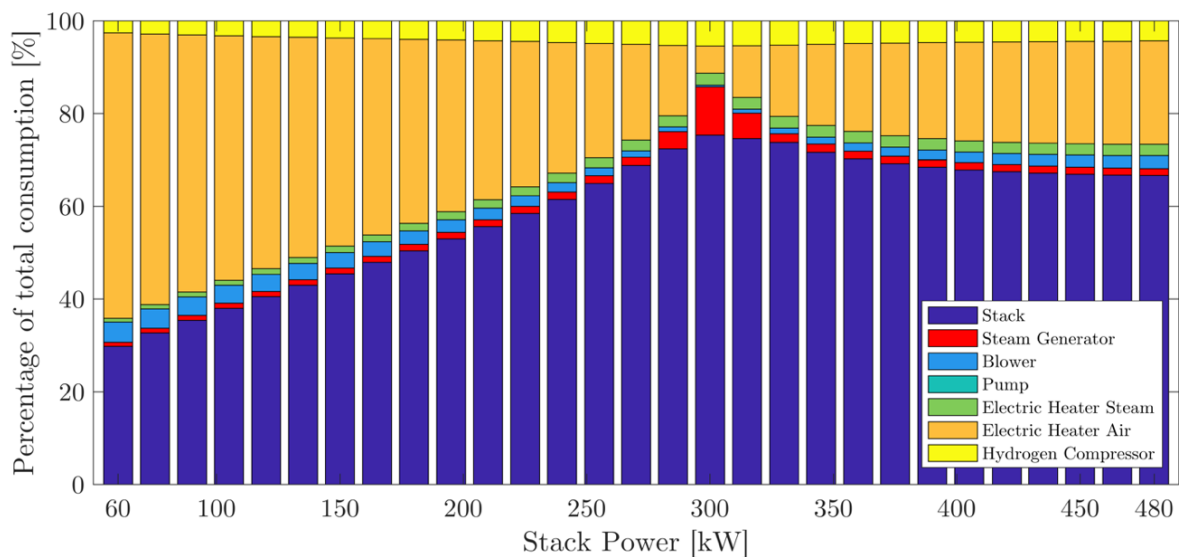
Figure 18. Contribution of each component to total system electricity consumption at differents stack loads, with constant average cell temperature control in steady state conditions.

The hydrogen compression consumption contribution varies between 3% and 6 % in the whole operating range of the system since is dependent only on the hydrogen production rate.

In the case in which the inlet air temperature is kept constant, showed in Figure 19, the system behaviour sensibly changes. The stack accounts for the largest share of electric consumption, higher than 70% in a wide range of operating conditions; only in strong endothermic condition the energy need for stack heating reduces the stack electrical contribution below 50%.

The second main difference is that the energy need for steam generation contributes for 10-14% of total consumption for stack loads between 180 and 435 kW. This is the range in which the airflow is at the minimum meaning that a relatively small amount of heat can be recovered in steam generator section and the evaporation heat has to be provided via electric heating. This fact can offer a good opportunity for integration with low temperature heat sources as will be investigated in this dissertation.
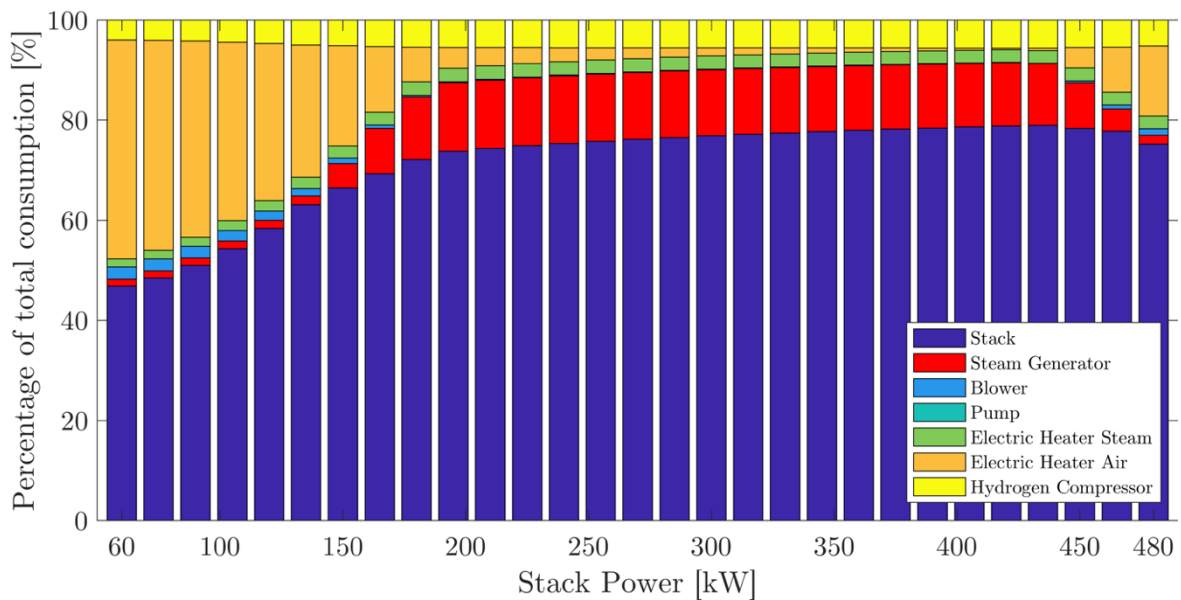
Figure 19. Contribution of each component to total system electricity consumption at different stack loads, with constant air inlet temperature control in steady state conditions.

In both cases the inlet steam temperature to the stack is kept constant to 750°C and for this reason the power consumption contribution of the high temperature steam electric heater is around 1-3% for all the operating conditions. The water pump is also a component who does not affect the system performance accounting for 0.1% of the electric consumption.

The final and most important comparison between the two control strategies can be made in term of electrical efficiency of the hydrogen production at different system loads showed in Figure 20. If the constant cell temperature strategy is implemented, the system reaches a maximum efficiency of 73%$_{LHV}$ at thermoneutral voltage that is the condition in which the stack electrical efficiency is 100%$_{LHV}$ and the stack load is 300 kW. When the load changes the auxiliary consumption rapidly rises resulting in much lower efficiencies, down to 35%$_{LHV}$. The working range with acceptable efficiency, at least comparable with competing technologies like PEM and ALK that can reach 60%$_{LHV}$ [44], is then limited to stack loads higher than 225 kW, reducing the operating range from 48% to 100% of stack load.

The second control strategy allows to reach a higher efficiency at higher load, reaching a peak efficiency of 75%$_{LHV}$ at 420 kW. The main finding is that electrolysis can be performed at very high electrical efficiencies, higher than 70%$_{LHV}$, for stack loads higher than 180 kW (from 37 to 100% of stack load). At lower loads the overall efficiency drops to 55%$_{LHV}$ a value that is still comparable with other electrolysis technologies.

The second relevant aspect is that if the consumption of the electric steam generator is not taken into account i.e. an external steam source is available, in the same range of working conditions the system electric efficiency reach remarkable values higher than 85%$_{LHV}$. This advantage is much lower if the constant cell temperature control strategy is applied because of the good internal heat integration that can cover most of the steam generation heat consumption. Improvements of electrical efficiency around 10% are present only for operating points around the thermoneutral voltage.
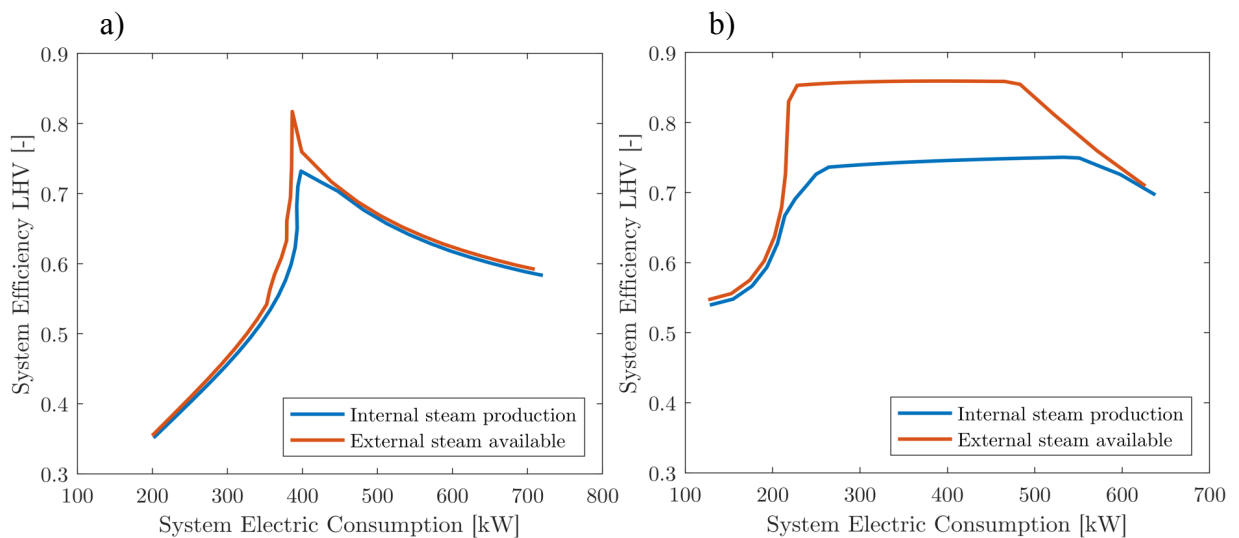
Figure 20. System electrical efficiency comparison between the two implemented control strategies:a) Constant average cell temperature,b) Constant air inlet temperature.

The results clearly highlight that, implementing a control strategy that allows cell temperature variations of around 90°C, high efficiency steam electrolysis can be performed in a wide range of operating conditions. In this comparative analysis the same stack can be better employed reaching higher current densities and consequent higher hydrogen production. The capability of working with high efficiencies at variable loads is a key characteristic for the integration with variable renewable energy sources for renewable hydrogen production.

3.2 Dynamic simulation results

The dynamic operation of this electrolysis system is important due to the desirable coupling with variable renewable energy sources. Strong transient behaviour can result in real working condition from cloud cover passing over a photovoltaic plant, sudden decrease or rise of winds powering a wind farm or sudden releases or request of power from the grid resulting in a sudden increase or decrease of available power for electrolysis. Literature works show that the most critical conditions regarding thermal stresses for solid oxide system can be experienced in sudden step changes of current density; the resulting perturbation are not realistic working conditions but any other transient will result in milder conditions regarding both thermal stresses and control loop reactions [40].

A series of simulations of step changes in power supply, both step increase and step decrease, have been performed in order to assess the capability of the cell to sustain such perturbation and the effectiveness of the control loop. In this section, only step increases simulations are reported since the results shows more severe conditions compared to step decreases of stack power. The simulations are summarized in Table 8.

Table 8. Summary of stack power step increases simulated.

Stack Power step increase				
Initial stack load [kW]	Initial load percentage [%]	Final stack load [kW]	Final load percentage [%]	Line color
90	18	180	37	————
		300	63	————
		360	75	————
		480	100	————

It can be clearly noticed from Figure 21 that a step increase in stack power is immediately reflected by a step increase in average current density. When the constant inlet air temperature control is implemented after the initial step, Figure 21.a, the current density values reached after the stack power increase remain constant. If the constant air inlet temperature control is implemented, Figure 21.b, after the first step the current slowly changes to higher values as the average cell temperature increases and the cell resistance decreases.

The final current is lower than the constant cell temperature control case if the stack still operates in endothermic mode after the step, resulting in a higher cell resistance or higher when

the stack moves to operating points in the exothermic region and the cell resistance decreases as consequence of increasing cell operating temperature.
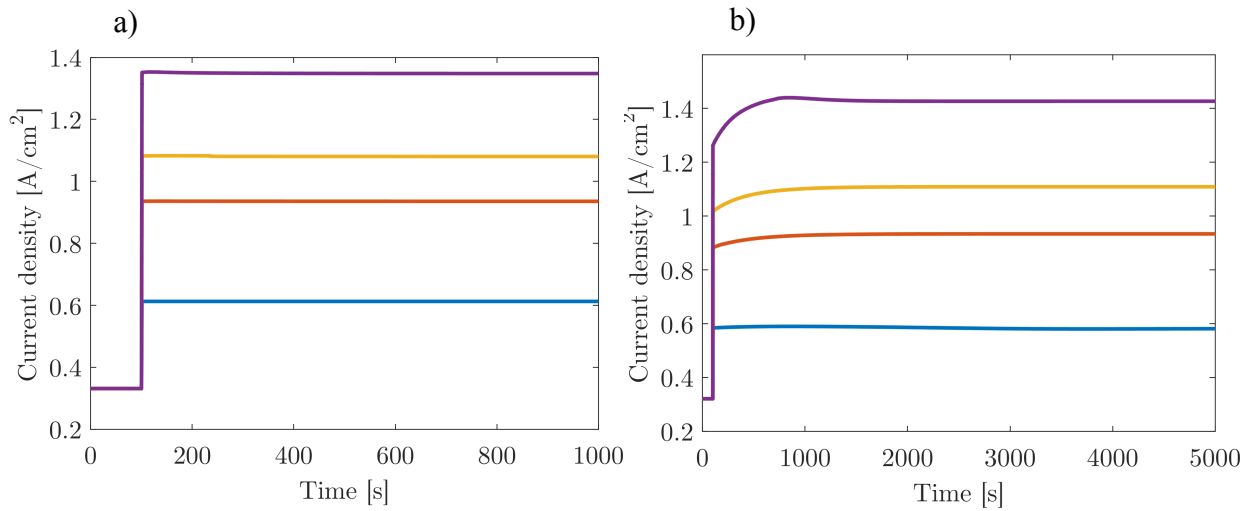
Figure 21. Transient response of current density to a step increase in stack power when differrent control strategy are implemented: a) Constant average temperature , b) Constant inlet temperature.

The same slow transient is present also in Figure 22.b as the voltage suddenly increases when a step increase in power is imposed to a cold cell but then, in about 2000 s, the voltage stabilizes reaching the corresponding steady state value. The voltage behaviour comparison between control strategies is complementary to the current density one. The final voltages are higher for the constant inlet temperature control when the cell operate in endothermic mode and lower when the cell operate in exothermic mode.
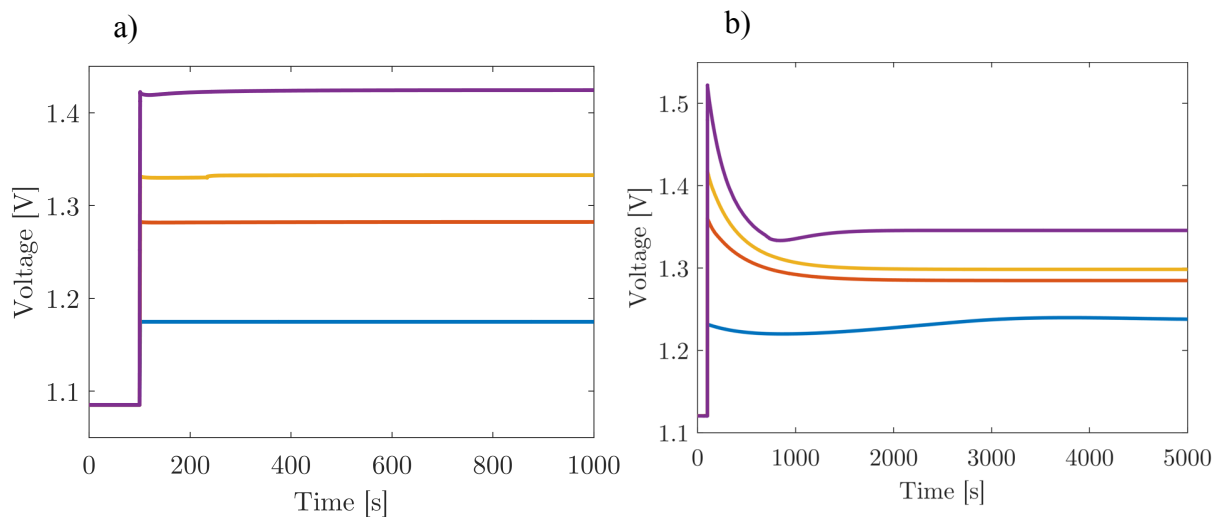
Figure 22. Transient response of cell voltage to a step increase in stack power when differrent control strategy are implemented: a) Constant average temperature , b) Constant inlet temperature.

As explained the reason of the different behaviours is the different transient experienced by the average cell temperature after the power step increase that can be observed in Figure 23. The first control strategy is able to maintain the average temperature of the cell variation lower than 2°C even during the most severe transient up to maximum stack power and bring the temperature back to the desired value in around 800 s, as can be observed in Figure 23.a. If the second control strategy is implemented the average temperature at the starting operating condition is 710°C and only after 2000 s reaches the final values as can be observed in Figure 23.b. In particular can noticed that when the stack operated at 300 kW, orange curve, is at thermoneutral condition and the final temperature is 750°C as in the other control case. In the case the final load is the maximum one, purple curve, the average temperature has a peak at 795°C after 900 s and then decrease to 790°C after the controller reaction to the increase of air outlet temperature as will be explained in this section.
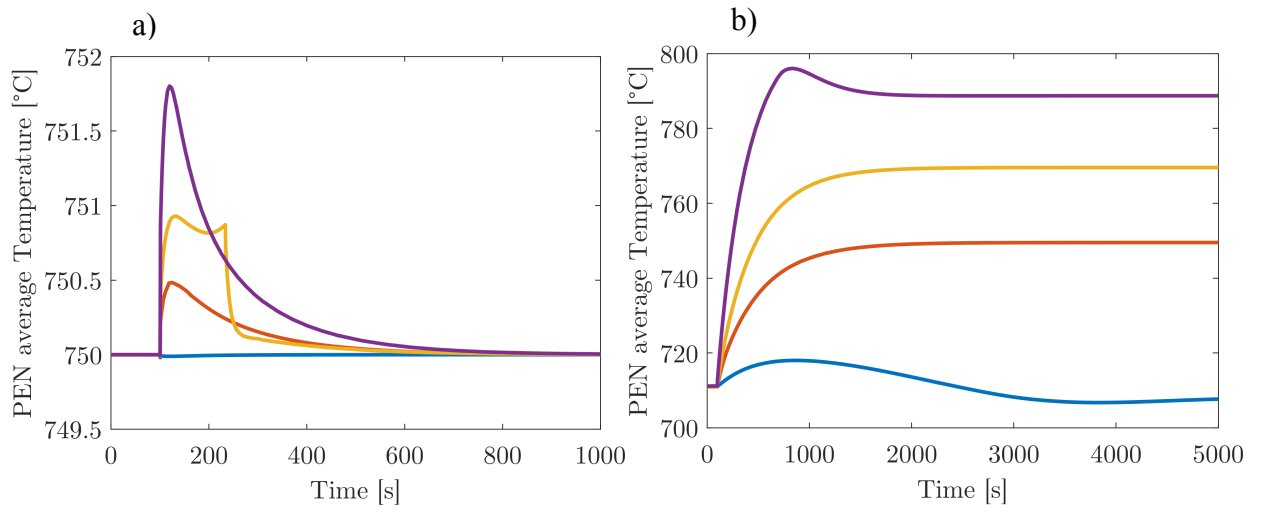
Figure 23. Transient response of cell temperature to step increase in stack power when differrent control strategy are implemented: a) Constant average temperature , b) Constant inlet temperature.

The controller reaction during the transient when the constant average cell temperature control is implemented is represented in Figure 24. At the initial operating point, the air blower absorbs 11 kW and the air inlet temperature is 781°C, hotter than the cell, since the operating condition is endothermic. Immediately after the step change in stack power the blower power is manipulated together with the inlet temperature of the air to the stack to keep the average temperature of the cell to the desired value of 750°C. The blower power decreases only when the new operating condition is near the thermoneutral voltage (orange curve) and air is no more needed for temperature control. In this case the inlet air temperature gets set to 750°C. In the

two cases in which the stack after the step is operated in exothermic mode and heat needs to be removed from the stack the blower power increases while the stack air inlet temperature decreases below the cell operating temperature. At maximum stack load the blower power consumption reaches 35 kW and the air inlet temperature decrease to 697°C.
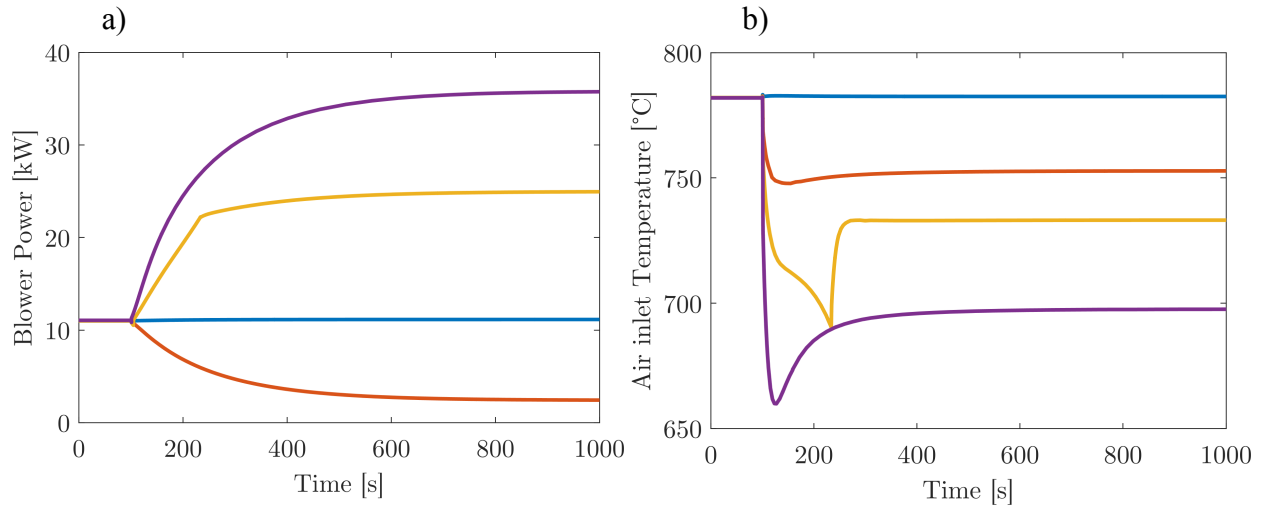
Figure 24. Controller response when the the constant cell temperature strategy is implemented: a) Blower power consumption, b) Stack air inlet temperature.

In the cases in which the second control strategy is implemented and the air inlet temperature is kept constant at 750°C, the controller reaction to the same step increases in stack power consists only in the manipulation of the air blower and it is showed in Figure 25. In every case an increase in stack power is followed by a decrease in the blower power consumption since, as previously explained, moving to less endothermic or exothermic operating point causes cell temperature increase above the lower threshold of 705°C. The blower is rapidly turned down to the minimum load of 0.5 kW except in one case. This case is the in which the final operating condition is still endothermic and the blower turn down is much slower and finally settle after 5000 s to a value that is slightly higher than the minimum because that stack operating load corresponds to cell temperatures very close to the set point threshold; this reaction is due to the fact that, immediately after the step power change, the voltage increases followed by the temperature but, as the cell resistance decrease, the voltage decrease again and the cell settle to a lower temperature at steady state.

In the case in which the final operating load is the maximum load, purple curve, after 690 s the air outlet temperature reaches the upper threshold set point of 795°C and the controller react increasing again the airflow via the blower, causing the decrease in cell average temperature highlighted in Figure 23.b, that reach the maximum power consumption after 2000 s equal to 8.1 kW.
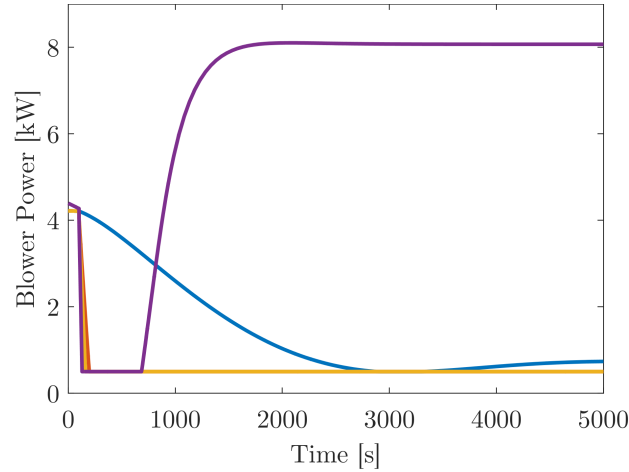
Figure 25. Controller response when the constant air inlet temperature strategy is implemented.

One of the main concerns for solid oxide cells integrity and degradation over time are the thermal gradients across the cells that, as previously stated have to be kept below 100°C for a solid oxide cell of 0.1 m of side length. Figure 26 clearly shows the evolution over time of the temperature difference between the hottest and coldest point of the cell after the step increases of stack power.

When the constant average cell temperature control strategy is implemented, Figure 26.a, can be noticed that generally, as the cell becomes less endothermic the temperature gradients decrease from the initial situation. In the case the final operating point is the maximum load, after an initial decrease, the temperature difference across the cell increases again as the airflow in increase and the air inlet temperature change from values hotter than the cell to values colder as previously explained. In around 300 s the temperature gradient across the cell decreases to 6°C and increases again up to 28°C. The same behaviour can be observed in Figure 26.b when the constant air inlet temperature is implemented with the difference that all the transients are at least 2000 s long and the entity of the temperature difference across the cell is always lower than the cases in which the first control strategy in applied. The maximum temperature difference is 19°C, reached when the stack is operated at maximum load.

In both control strategy graphs can be highlighted that when the stack is operated at the thermoneutral condition, orange line, the temperature difference across the cell approaches zero because the inlet temperatures of both air and steam are set to 750°C and the cell internal losses equals the thermal energy need for electrolysis.
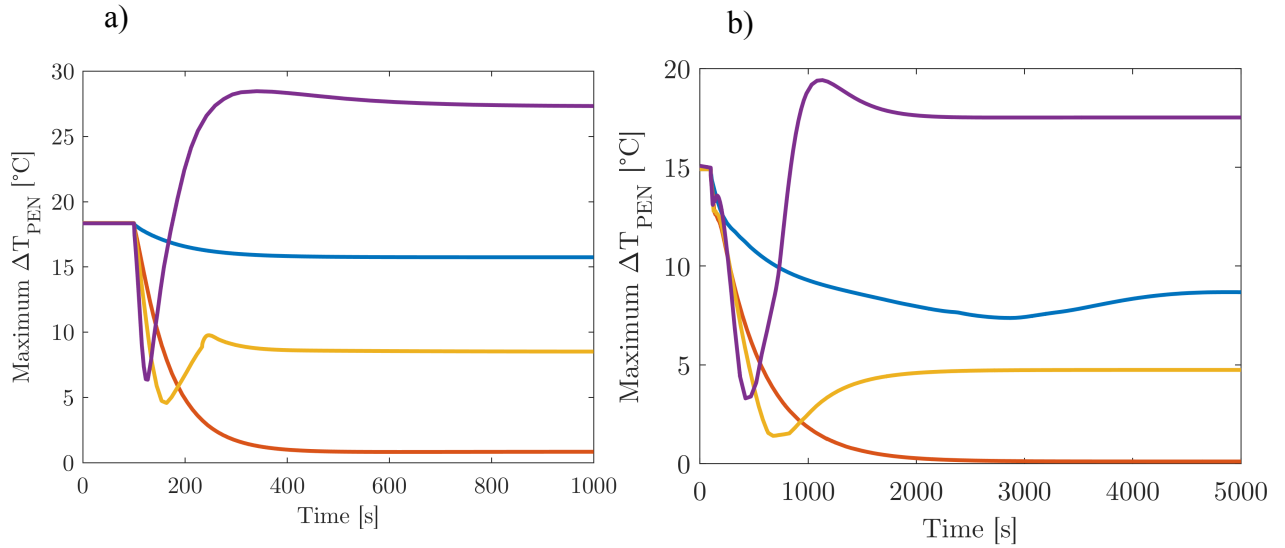
Figure 26. Evolution of maximum temperature difference across the cell after step increase in stack power when differrent control strategy are implemented: a) Constant average temperature , b) Constant inlet temperature.

From the results presented in this section can be stated that both control strategies are able to maintain the cell inside the safety limit of temperature gradients during dynamic operation. Moreover, the temperature gradients experienced by the cell when the constant inlet temperature control is applied are generally lower and evolve with slower transients, further decreasing thermal stresses and the risk of cell ruptures.

3.2.1 Photovoltaic generation profiles

To assess the capability of the electrolysis system to effectively convert renewable electrical energy into hydrogen and to dynamically follow input power variation, the integration with a solar photovoltaic installation is simulated in this section.

Two representative power generation profiles, referring to the same installation, have been acquired from real data of the UCI campus photovoltaic installations and reported on Figure 27. One curve represents the power production of a clear sky day while the other represents a day with passing clouds over the installation.
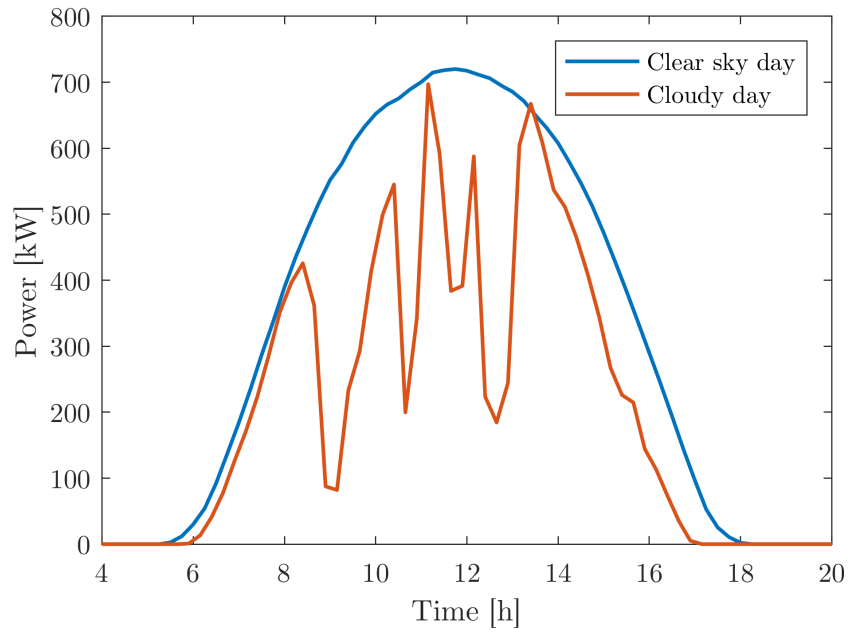
Figure 27. Photovoltaic power generation profiles.

The curves have been scaled to simulate the installation of an electrolysis system sized to fit existing photovoltaic installations. The control strategy based on constant air inlet temperature has been implemented since previous results clearly showed better performance in terms of operating range and efficiency.

The results of the load following simulation for the clear sky day are reported in Figure 28. As expected the system is able to receive the power produced by the photovoltaic plant ramping up from the minimum operating load in the morning to values close to the maximum load around noon and then slowly decreasing the load during the afternoon following the natural daily irradiance profile. Given the timescale all the transients are very smooth and the only irregularities are related to the moments in which the cell temperature reaches the lower and upper threshold as can be noticed in Figure 28.c before 8 am, during the start up when the cells is at 710°C, between 10 am and 2 pm when the cell reaches the highest loads and the

temperature reaches 795°C and after 4 pm when the cell return to temperature around 710°C. The time periods just mentioned are also characterized by the higher temperature differences across the cell caused by the increased airflow needed for heating or cooling the cell. The good performance of the electrolysis system is highlighted in Figure 28.d that shows that the process efficiency throughout the day remains on values higher than 70%$_{LHV}$ for the majority of the time and especially during the periods in which the current is high and consequently the hydrogen production.

During the 10.5 hours of operation the electrolysis system consumes 4,643 kWh, producing 101 kg of hydrogen and resulting in an average efficiency of 72.6%$_{LHV}$.
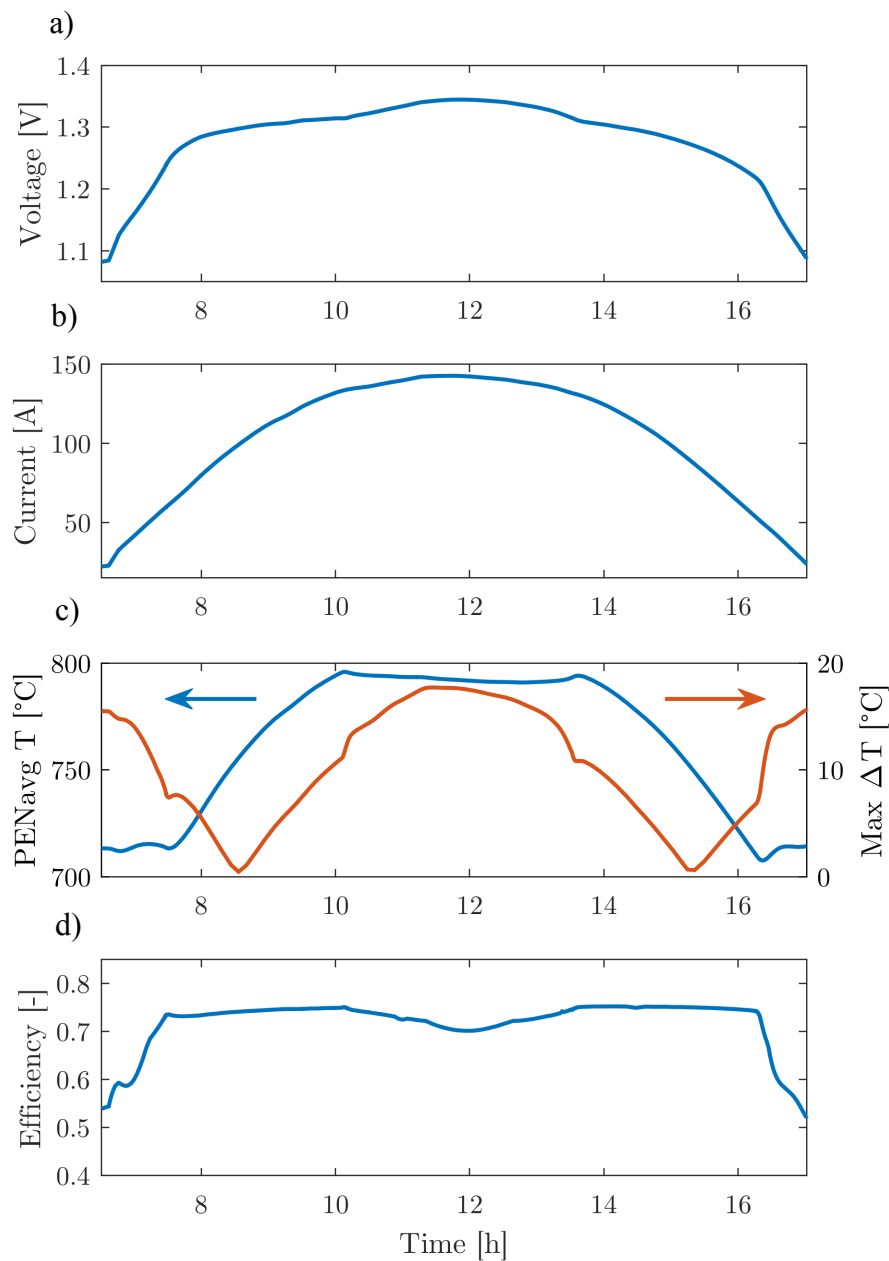
Figure 28. Electrolysis system simulation results during the clear sky day.

During the cloudy day several strong dynamic conditions are present, but the system is able to modulate its operating condition following the available power. The transients related to the passing clouds cause multiples fluctuations of the average operating temperature of the cells that during the day switch between exothermic and endothermic mode 10 times. These variations, that can be observed in Figure 29.c, are not excessive confirming the appropriate configuration of the control system that is able to keep the operating temperatures inside the 90°C safety range during realistic dynamic operation. The maximum temperature difference across the cell is lower than 10°C most of the time and rises to higher values in the moments in which the cell temperature reaches the lower limit value of 710°C and the cell needs to be heated with the increased airflow. The increased auxiliary consumption related to cell heating with respect to the stack consumption causes the temporary drop of efficiency to 45%$_{LHV}$ around 10 am as can be noticed in Figure 29.d.

The other input power variations do not result in large efficiency penalties since every time there is a decrease in input power the efficiency increase at first, when a relatively hot cell is operated at low voltages and then start to decrease when the cell temperature decrease below 750°C with the consequent increase of cell resistance. As previously highlighted in Section 3.1.2 in the steady state analysis, if a power variation does not bring the stack to work below 37% of maximum load or the power supply rise again above that threshold in such a way that the cell temperature does not have time to decrease enough to activate the control reaction, the system efficiency remains higher than 70%$_{LHV.}$

During the 9.5 hours of operation the electrolysis system consumes 3,091 kWh, producing 67.23 kg of hydrogen and resulting in an average efficiency of 72.5%$_{LHV}$.

The results show that this system configuration could perform high temperature electrolysis at part load and under dynamic conditions typical of photovoltaic power production without showing relevant impact on the daily average hydrogen production efficiency that remains around 72%$_{LHV}$ when steam is considered to be internally generated.
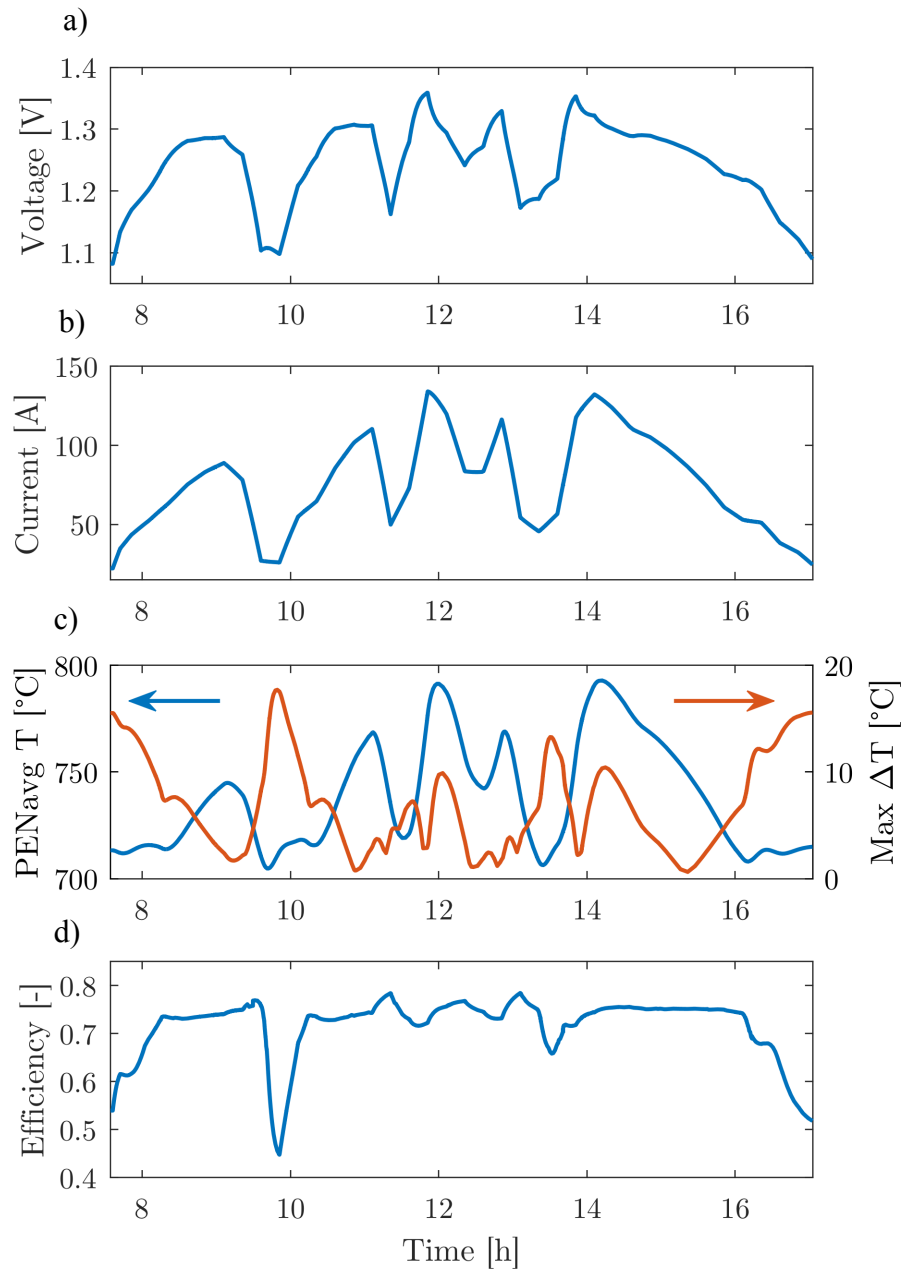
Figure 29. Electrolysis system simulation results during the cloudy day.

4 Microgrid Integration: Model development

The University of California, Irvine campus offers a unique opportunity to investigate the management and performance of a microgrid. The microgrid present a variety of buildings type such as classroom, laboratory facilities and offices and also some features that are going to become part of future energy systems such as electric vehicle fleet and their charge stations, batteries for grid balance and renewable distributed energy sources [45][46]. The campus has been planned and built starting from in the 1960s around a central park surrounded by an underground tunnel along which all the campus utilities networks are deployed. The campus microgrid is connected with the external Southern California Edison (SCE) grid through a substation where the voltage is decreased from 66 to 12 kV. The campus can operate in parallel with the external grid but has an agreement with SCE for a minimum continuous import of 100 kW and the export must be avoided or the university has to pay additional fees or force the plant shut down [47].

The campus power plant is able to provide more than 90% of campus electricity consumption via ten 12 kV circuits and district heating and cooling network. The power plant consists in a 19 MW natural gas fired combined cycle formed by a 14 MW gas turbine and a 5 MW steam turbine, 7 electrically driven chillers and 1 steam driven absorption chiller. One of the main characteristics of the UCI central plant is the presence of a 175 MWh cold water storage tank that allow the microgrid management to run the chillers during off peak hours, having to run chiller during on-peak electricity rate hours only during summer hottest days [48].

On the UCI campus, following the plan of University of California carbon neutral future, are already on operation three large photovoltaic installations over parking structures and many other distributed rooftop installations for a total installed capacity of more than 4 MW and two two-axis tracking photovoltaic devices of 113 kW installed capacity. These solar installations are already introducing challenges to the microgrid operation when the power plant output has

to adjust in order to allow the renewable energy utilization in the grid. Given the future goal of UCI administration of increasing the renewable energy share into the energy mix the implementation of energy storage will become a fundamental component of the campus energy infrastructure.

Recently a 60 kW Power-to-gas system based on a Proton Exchange Membrane electrolyzer have been installed to produce renewable hydrogen from photovoltaic electricity and investigate the effects of hydrogen injection into the natural gas feeding the gas turbine [49].

A schematic of the existing microgrid components considered and modelled in this work, their interconnections and the integration of the SOEC system are showed in Figure 30.
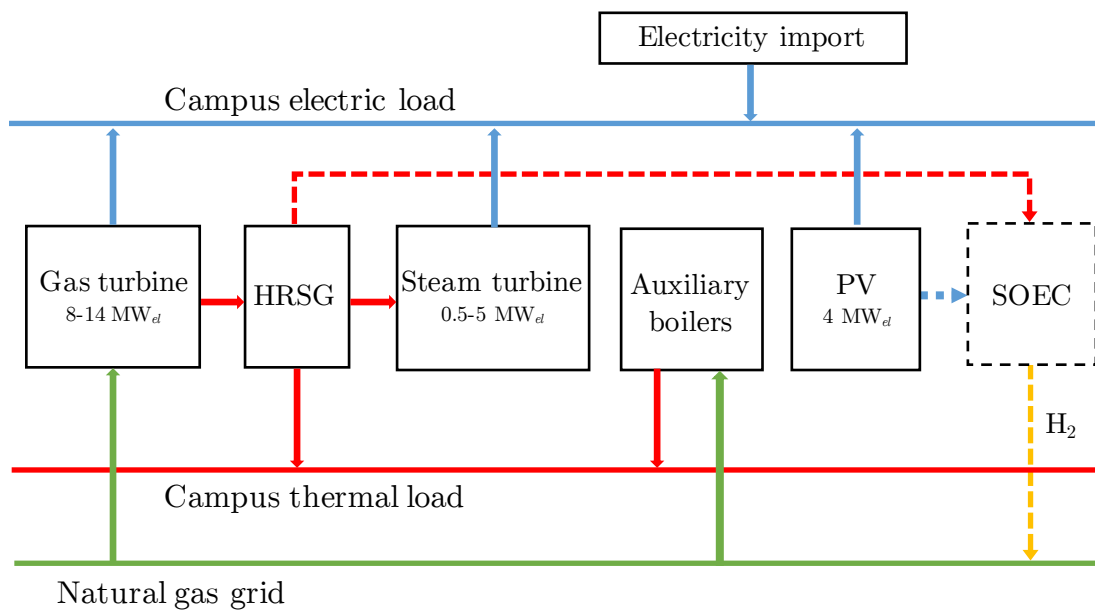
Figure 30. Schematic representation of microgrid components considered in the analysis and SOEC electrolyzer integration.

4.1 Microgrid demand profiles

Historical data about the campus demand and photovoltaic production from the year 2014 have been provided by UCI, Facility Management and used as input for the model. The data come with a 15 minutes resolution and comprehend both electricity and thermal demand. The campus electric and thermal loads are showed in Figure 32 and Figure 31 respectively.
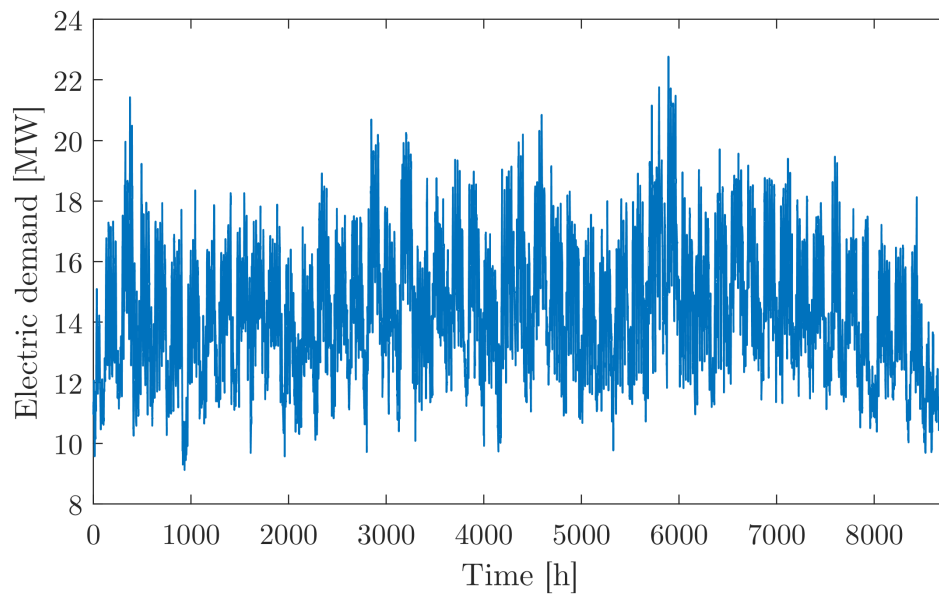
Figure 32. UCI campus electricity demand for the year 2014.
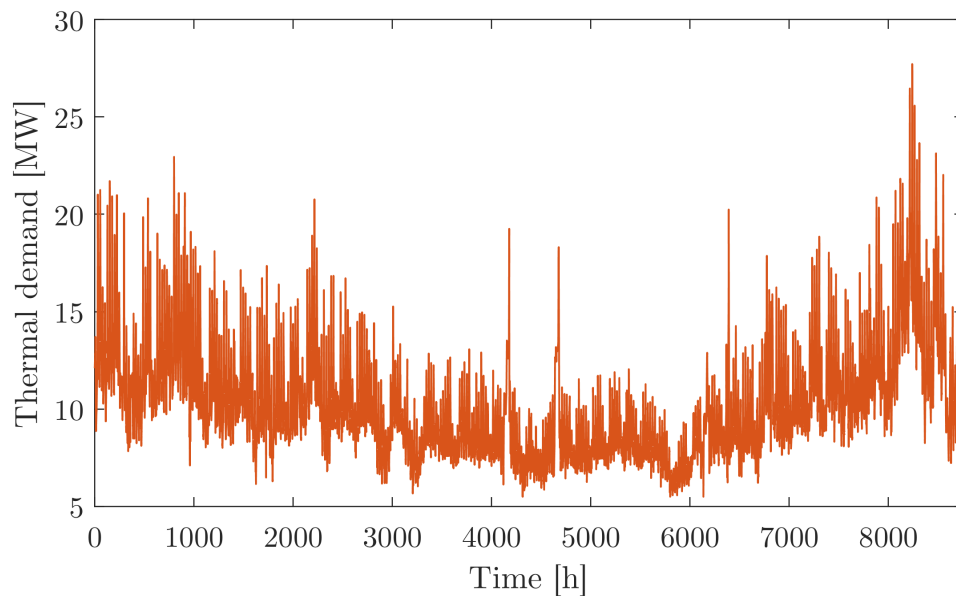
Figure 31. UCI campus thermal demand for the year 2014.

The campus annual electric demand was around 126 GWh in 2014 with an average load of 14.32 MW, a maximum load of 27.7 MW and a minimum load of 9.2 MW. Electricity demand is quite uniform during the year presenting daily peaks in work days and decreasing over the weekends. The highest electrical consumption days usually coincide with the hottest days when the electrical demand for campus air conditioning is highest. Campus thermal demand varies

between 5 and 27 MW and shows a significant seasonal variation rising during the winter and generally decreasing over the summer.

The photovoltaic installed capacity in 2014 represented by the data was 893 kW and it has been scaled up for future scenarios simulation with a scaling factor in order to simulate the grid response to increasing renewable installed capacity.

$$PV_{ScaleFactor} = \frac{Future\ installed\ capacity}{Installed\ capacity\ (2014)} \tag{39}$$

A previous work from UCI, Advanced Power and Energy Program estimates a maximum of 15 MW fixed photovoltaic installation (mainly building rooftops, parking structure terraces) and up to 22 MW of ground mounted 2-axis tracking photovoltaic systems in the surroundings of UCI campus [46].

4.2 Microgrid power plant model

The Gas Turbine is the main component of the campus power plant. The maximum electrical power output is 14 MW and the turbine can be turn down to a minimum power output of 8 MW; the minimum operating point is a consequence of necessary compliance to strict emissions law of the state of California [48]. Second important operational constraint is the ramp rate that has been set to reflect the capability of this turbine to go from minimum to full load in 1 hour, resulting in a ramp rate of 6 MW/h.

A simplified regression based gas turbine model previously developed [50], has been implemented to simulate the operation of the campus power plant main component. The gas turbine electrical efficiency and Turbine Exit Temperature are correlated to the electrical power output $P_{GT,El}$ according to Equations (40) and (41), represented in Figure 33.

$$\eta_{GT,El} = -8.9 \cdot 10^{-4} \cdot P_{GT,El} + 0.0299 \cdot P_{GT,El} + 0.0833 \tag{40}$$

$$TET = 0.069 \cdot P_{GT,El}^4 - 2.12 \cdot P_{GT,El}^3 + 19.14 \cdot P_{GT,El}^2 - 31.57 \cdot P_{GT,El} + 636.27 \tag{41}$$
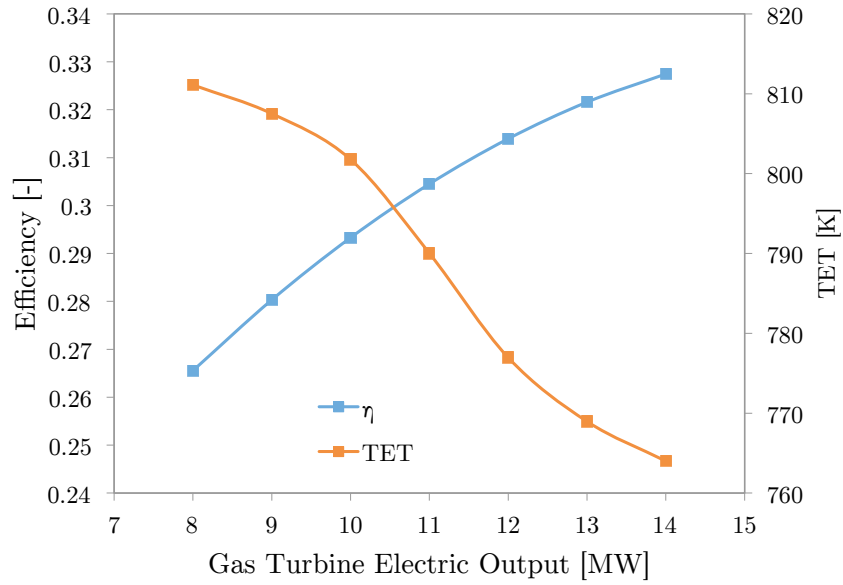
Figure 33. Gas turbine regression based operating parameters.

From the figure can be noticed that the electrical efficiency of the turbine decrease form 0.33 at the maximum operating load to 0.26 when the turbine operates at the minimum electric power output of 8 MW. The temperature of the turbine outlet and increase 764 K at maximum load to 811 K when the turbine is turned down to the minimum load.

The thermal power available from the turbine exhaust for the heat recovery steam generator is evaluated with Equation (42). The equation takes into account the average discharge temperature of turbine exhaust gases to ambient after the steam generator of 450 K compared to the reference temperature at which heating values are evaluated of 273 K.

$$P_{GT,Th,Waste} = P_{GT,El} \cdot \frac{(1 - \eta_{GT,El})}{\eta_{GT,El}} \cdot \frac{TET - 450}{TET - 273} \tag{42}$$

This thermal energy in form of steam is then used in the cogeneration plant to feed the steam turbine and to cover the campus heat demand via a steam/pressurized water heat exchangers section.

The 5 MW Steam Turbine never operates at full load since it is oversized for the application, the minimum operating point is 0.5 MW electric output, and it can be turned on and off depending on electric demand and steam availability [51]. The ramp rate implemented in the model is 4 MW/h. In every moment the maximum possible electrical output that can be delivered by the recuperative Steam Turbine is then related to the available waste heat by the electrical efficiency $\eta_{ST,El}$ according to Equation (43).

$$P_{ST,el} = P_{GT,Th,Waste} \cdot \eta_{ST,El} \tag{43}$$

During periods in which the waste heat from the gas turbine is not enough to cover the campus heat demand, additional Natural Gas can be burned in auxiliary boilers and by a duct burner present upstream the heat recovery steam generator [52]. The operational parameters and assumptions of the microgrid model are summarized in Table 9.

Table 9. Summary of microgrid model parameters.

Microgrid model parameters				
Gas Turbine	Electric output range	$8 - 14$	MW
	Electrical efficiency, $\eta_{GT,El}$	$f(P_{GT,el})$	-
	Turbine exit temperature, TET	$f(P_{GT,el})$	K
	Ramp rate	6	MW/h
Steam turbine	Operating range	$0.5 - 5$	MW
	Electrical efficiency, $\eta_{ST,El}$	0.25	-
	Ramp rate	4	MW/h

4.3 Microgrid dispatch model

The dispatch of the microgrid energy sources has been simulated as a linear programming problem implemented in Matlab® and solved with the *linprog* function. The problem variables have to be linked together with linear constraints and upper and lower boundaries must be set.

The problem variables are the electrical power output of the Gas Turbine ($P_{GT,El}$), the amount of waste thermal power in form of steam fed to the Steam Turbine ($P_{ST,Th}$), the extra natural gas power needed to satisfy thermal demand ($P_{EXTRA,Th}$), the electrical power import from external grid ($P_{IMPORT,El}$), the possible electric power excess ($P_{EXCESS,El}$) and the waste thermal power still available from the gas turbine outlet that is no being recovered ($P_{EXCESS,Th}$).

The electrical and thermal power balances are the constraints that must be satisfied at every time step:

$$P_{GT,El} + P_{ST,El} + P_{IMPORT,El} - P_{EXCESS,El} = LOAD_{El,2014} - P_{PV,El,SCALED} \tag{44}$$

$$P_{GT,Th,Waste} - P_{ST,Th} + P_{EXTRA,Th} - P_{EXCESS,Th} = LOAD_{Th,2014} \tag{45}$$

The objective function reflects the current dispatch strategy of UCI microgrid oriented to maximize the utilization of the cogeneration plant thus minimizing imports of electrical power from Southern California Edison grid and additional natural gas to cover thermal demand.

$$\min \{P_{IMPORT,El} + P_{EXTRA,Th}\} \qquad (46)$$

4.4 SOEC System Dispatch

The integration of SOEC Systems into the campus microgrid has been simulated as the deployment of multiple identical units previously modelled and presented in detail in Section 3.1.2.

The system control configuration that resulted in the best performance and that has been chosen for the grid integration is the one with constant air inlet temperature control. The steady state results of the physical model allow to characterize the performance of the single electrolysis system relating the system overall electric consumption with the outlet hydrogen production rate and with the consumption of the steam generator, to take into account the possible heat integration with the existing power plant. This simplified approach has been implemented to achieve computationally affordable simulation on annual data since the simulations performed in Section 3.2 did not highlight particular challenges to the dynamic operation of the SOEC system. The two characteristic curves are showed in Figure 35 and Figure 34. The values corresponding to intermediate working conditions are obtained via linear interpolation.

The inputs of the model are the annual electricity and heat excess profiles of the UCI microgrid obtained from the microgrid dispatch model. The otherwise curtailed electricity available at every time step is supposed to be delivered to the electrolysis system and to cover the power consumption of both SOEC stack and auxiliary components.

Two different dispatch strategies have been proposed and described in the following sections. In both dispatch approaches proposed the electrolysis modules are supposed to stay in a hot idle state when not in operation, energy consumption during the idle periods has not be taken into account but it has been estimated for a similar system that a 30 cm insulation layer is enough to keep overnight temperature decrease around 10 °C without additional active heating [29].
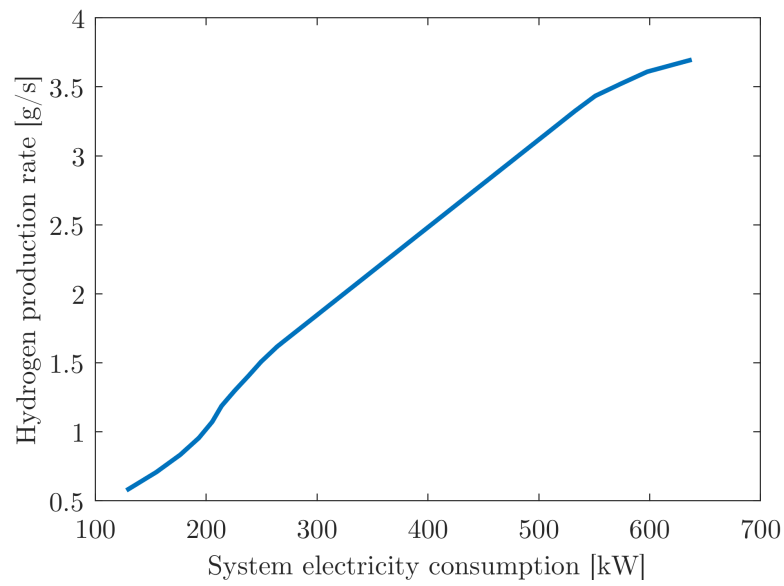
Figure 35. Hydrogen production rate of the single electrolysis module at different loads, function of the overall electricity consumption.
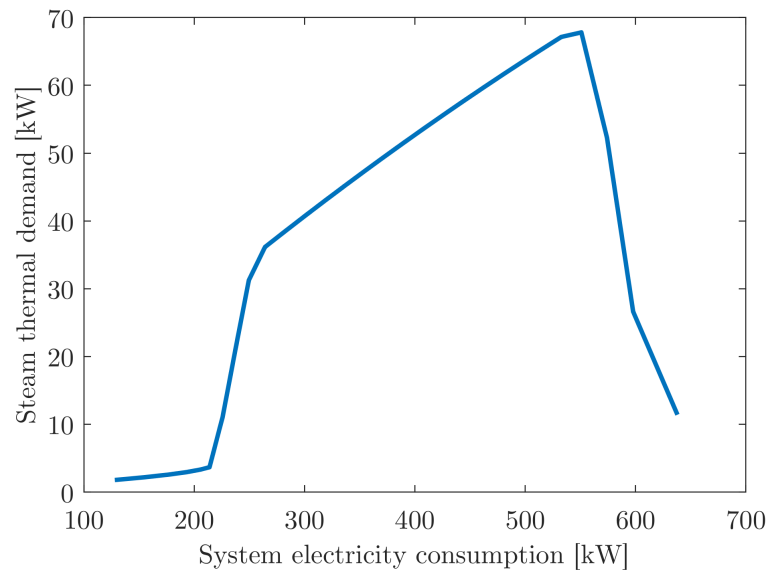
Figure 34. Steam generator consumption of the single electrolysis module at different loads, function of the total electricity consumption.

4.4.1 Sequential dispatch

When excess electricity from photovoltaic production is available on the microgrid, the SOEC modules are turned on sequentially one after the other. The modules are turned on when the amount of excess electrical power is higher than the power consumption of the single system module at the minimum load (120 kW). When the maximum load of the single module is reached, there is going to be some curtailment until enough power is available to turn on the next module. With this dispatch strategy every module works at full load except the last one that has been turned on that work at part load. In case of decrease of excess electrical power, the switch off procedure follow the symmetrical sequence.

In the scenario in which the integration of the electrolysis system with the heat recovery section of the cogeneration plant is taken into account, the available steam is fed to the electrolysis systems reducing the electrical consumption of the electrical steam generator and thus of the entire system. As a consequence of the reduced electrical consumption, the now available excess power is used to bring the electrolysis system to a higher stack load or to turn the following module on.

4.4.2 Parallel dispatch

This dispatch strategy requires that all the deployed electrolysis systems work in parallel at the same operating point. The available excess electric power is divided by the number of electrolysis module deployed and they all work at the same load. The modules are turned on only when is available enough power to turn every module on and in the same way when excess power is decreasing the working point of the modules is decreased equally until excess power reaches the minimum load and all of the electrolyzers are switched off at the same time.

In the scenario of heat integration with the cogeneration plant when steam is available, it is fed to all the modules and, since the overall electrical consumption would decrease, the now available excess power is used to increase the working load of the electrolysis modules increasing the hydrogen production.

5 Microgrid Integration: Results

5.1 Microgrid operation

Simulations of microgrid operation have been performed for the current situation and for future scenarios with increasing photovoltaic capacity installation to investigate the microgrid behavior to accommodate additional solar energy production and its limits. Two representative weeks of operation are reported and showed in Figure 36 and Figure 37.

In Figure 36 is reported a week in September characterized by high electric demand and relatively low thermal demand. It can be clearly noticed the weekly electric demand behaviour with daily peaks during work days and a general decrease over the weekend when most of campus activities are suspended. This week shows the ideal operation of the cogeneration plant, the gas turbine works at maximum load most of the time and since the campus heat demand is low also the steam turbine is able be employed to cover electric load. The fluctuation of the steam turbine output even when full electricity production would be requested are complementary with fluctuation of heat demand since priority on heat recovery is given to the latest.

In the lower part of the graph the daily photovoltaic production can be clearly identified with its peak in the middle of every day close to the maximum nameplate capacity of the current situation. September five shows and irregular shape of the photovoltaic production probably due to temporary clouds covers.

During this chosen week the electrical demand is particularly high overcoming the electricity production of both the campus power plant and photovoltaic installations and, as a consequence, electricity import from the external grid is present during the first four days and reaches values around 2 MW.

Substantial turn down of the cogeneration plant can be noticed during September 6 and 7 as a consequence of low electricity demand and high photovoltaic production forcing the power plant to reach the minimum operating condition of 8 MW electrical output during September 6; in this case the fast ramps are provided mainly by the steam turbine given the availability of recovered heat.

It can be clearly noticed that during this week the photovoltaic production is beneficial because mainly reduced the otherwise high electricity demand that would otherwise be covered with large imports.

Figure 36. Microgrid dispatch simulation results in a week of September with the current 4 MW of PV installed capacity.

The week in January represented in Figure 37 present relatively lower electrical demand but the campus thermal demand is much higher showing massive peaks at the beginning of every day. During the first four days these peaks reach 20 MW making impossible to be satisfied by heat recovery even when the gas turbine works at maximum load and the steam turbine is turned off. Additional natural gas has to be burned in the auxiliary boilers presents in the power plant every morning as can be noticed in the lower portion of the graph. Moreover, since the steam turbine is not covering its part of electrical load because of unavailability of steam for power generation, also electricity import is present during those mornings. Nevertheless, even during this week the photovoltaic production is well matched with the campus electrical demand, reducing considerably the electricity that would need to be imported since the heat recovery into the steam turbine is not possible as a consequence of relatively high heat demand.
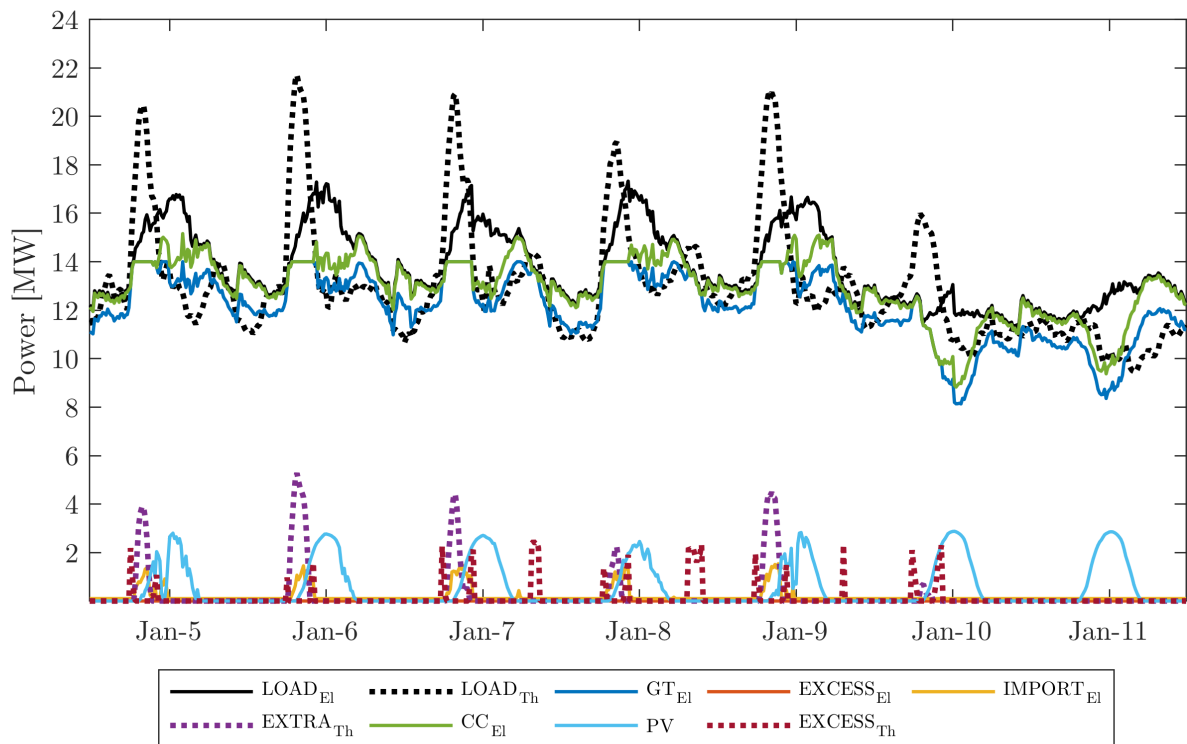
Figure 37. Microgrid dispatch simulation results in a week of January with the current 4MW of PV installed capacity.

The second scenario presented is the case in which 10 MW of photovoltaic capacity is installed on UCI campus, more than double with respect to the current situation. The same weeks have been reported in Figure 38 and Figure 39 to analyze the differences in microgrid response. In Figure 38 can be noticed that now the peak power output from the photovoltaic is

around 8 MW. More flexibility is requested to the gas turbine since every day the turbine has to ramp down as the photovoltaic output rises in the morning and ramp up as it decreases later in the afternoon. During the days with high electricity demand this fluctuation are still inside the microgrid limits and the additional photovoltaic capacity leads to reduced electricity import and reduced natural gas consumption compared to the present situation. As the electrical demand drops during the weekend, the first episodes of important curtailment occur in September 6: the steam turbine is turned off and the gas turbine works at the minimum power output of 8 MW but up to 4 MW of curtailment is necessary during the day since the power production exceed the demand.
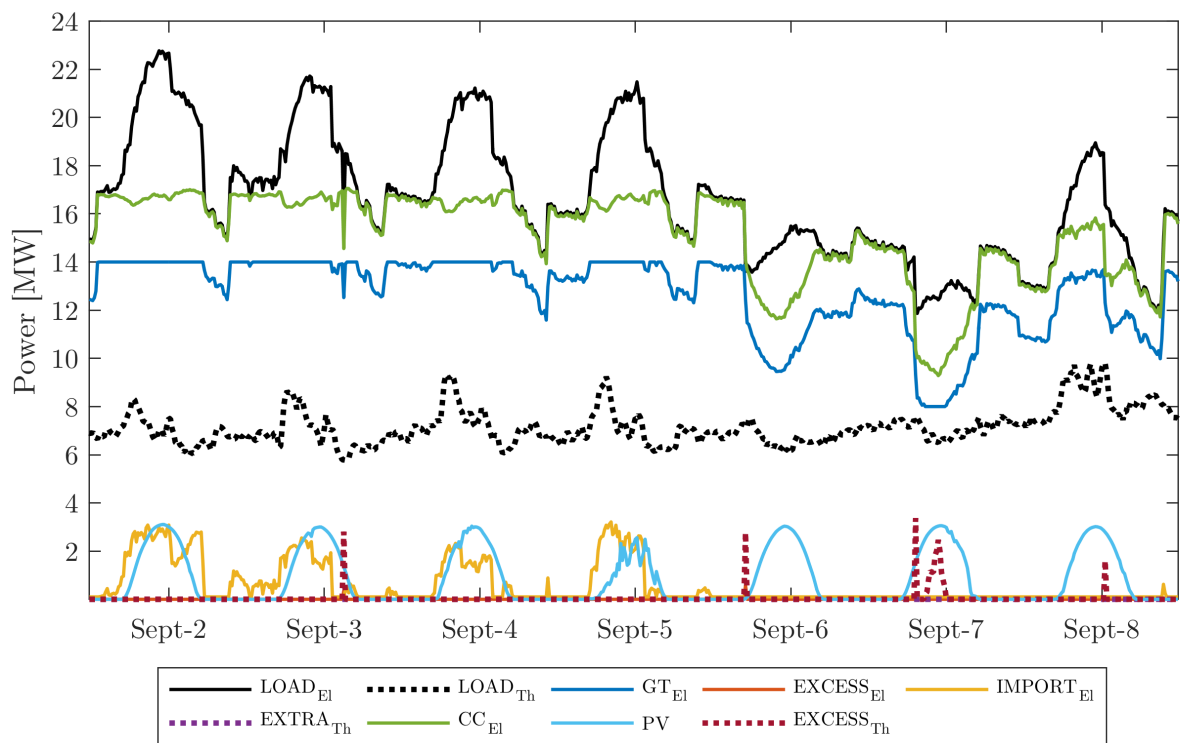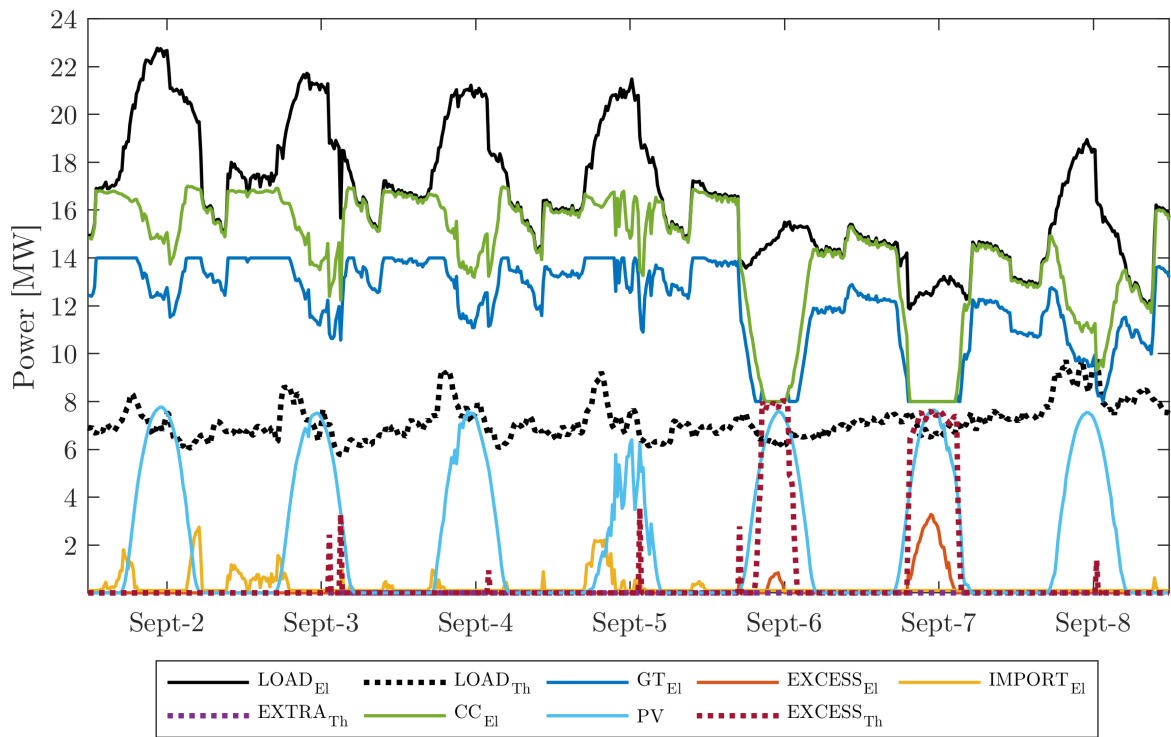

Figure 38. Microgrid dispatch simulation results in a week of September with 10 MW of PV installed capacity.

Regarding the week in January showed in Figure 39, the same response of the power plant to incoming photovoltaic production can be noticed throughout the week and again during work days the electrical demand is high enough to avoid complete gas turbine turn down while during the weekend curtailment would occur.

It can be also noticed that during days with uncertain weather, as January 5 and 9, strong dynamics have to be imposed to the campus power plant to compensate for the loss of photovoltaic production, but the resulting ramp rates are still achievable by the gas turbine alone

in this scenario since the high thermal demand prevents the utilization of the steam to drive the steam turbine.

Moreover, in both the weeks reported can be highlighted that as the power output of the campus power plant decreases to accept photovoltaic production, the fact that the steam turbine is turned off leaves large amounts of heat available to recovery from the gas turbine exhausts when the campus thermal demand is not particularly high, in particular during the days January 10 and 11 the excess of electricity and heat match.
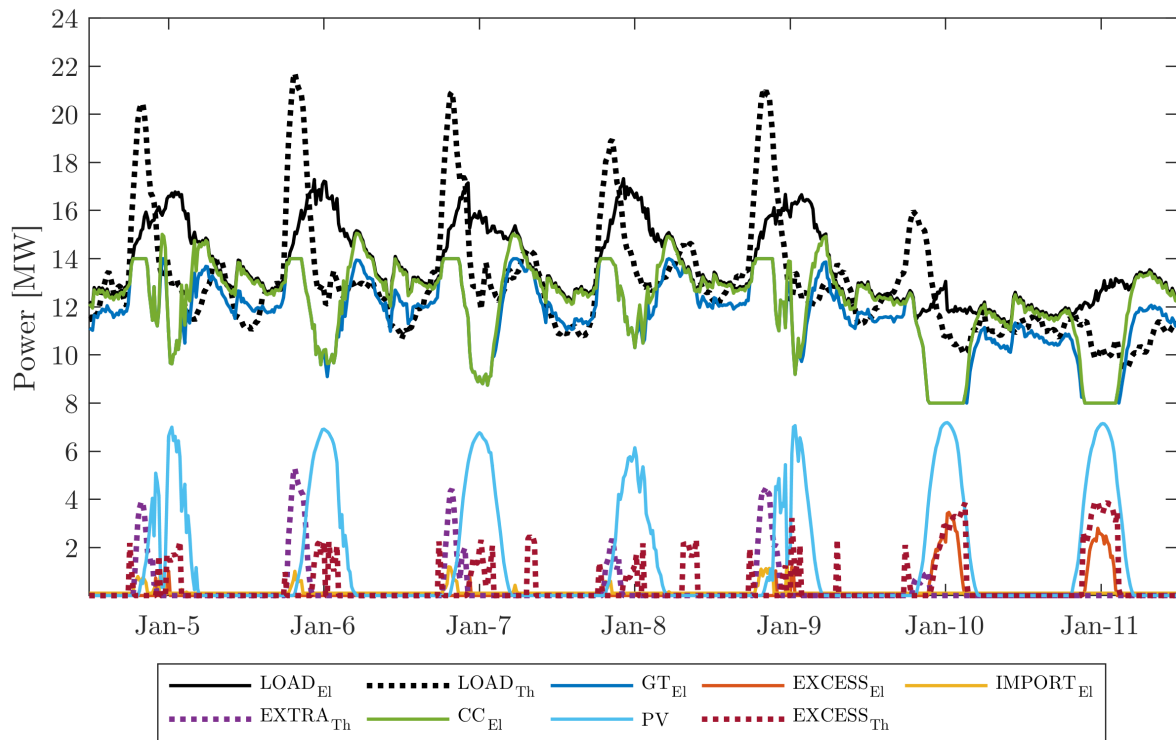
Figure 39. Microgrid dispatch simulation results in a week of January with 10 MW of PV installed capacity.

The last scenario reported in Figure 41 and Figure 42 for the two chosen weeks, is the scenario corresponding to 25 MW of installed photovoltaic capacity. In this scenario the peak photovoltaic power output reaches 19 MW and during many days this value is higher than the entire campus electrical demand. This situation will get worse for scenarios with higher photovoltaic capacity that are not showed here. As a consequence, every day the gas turbine has to be turned down to the minimum operating condition but still every day massive solar curtailment occurs. Electricity import is still necessary during the nights and during strong transient conditions.

In Figure 40, the grid operation is represented in detail during the day September 5. During this day clouds coverage appear from 10 to 11:30 am. As a consequence, PV output shows a drop from 13 to 1.3 MW followed by an increase to 16 MW in less than 2 hours. In the same time frame the gas turbine is not able to modulate its power output fast enough requiring electricity import to meet electrical demand from 10:30 to 11 during its ramp up and causing excess of electricity production during its ramp down between 11:30 and 12:15. After that the minimum operating point is reached and curtailment would occur anyway.

Can be noticed again that, when the heat demand is low enough, the presence of excess electricity and heat is often contemporary as showed in Figure 41. This fact will be exploited in the following section to supply steam to the electrolysis system generating it recovering heat from gas turbine exhausts.
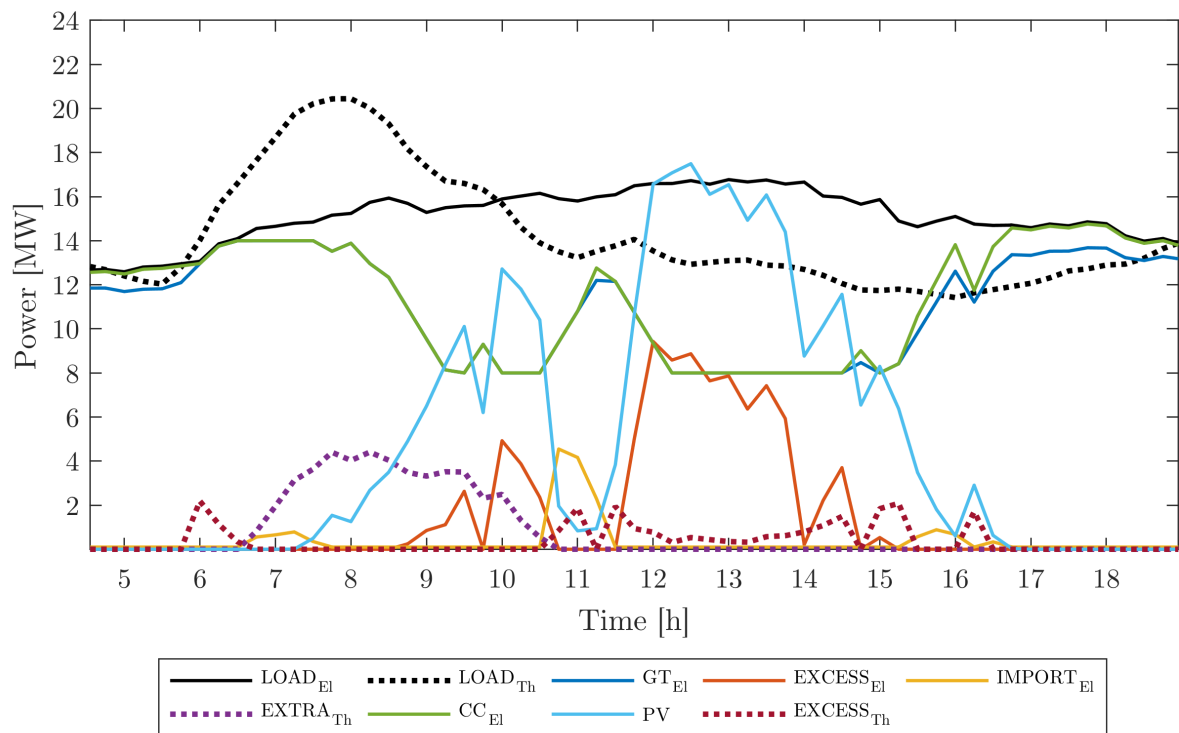
Figure 40. Detail of microgrid operation during the day January 5 with 25 MW of PV installed capacity.
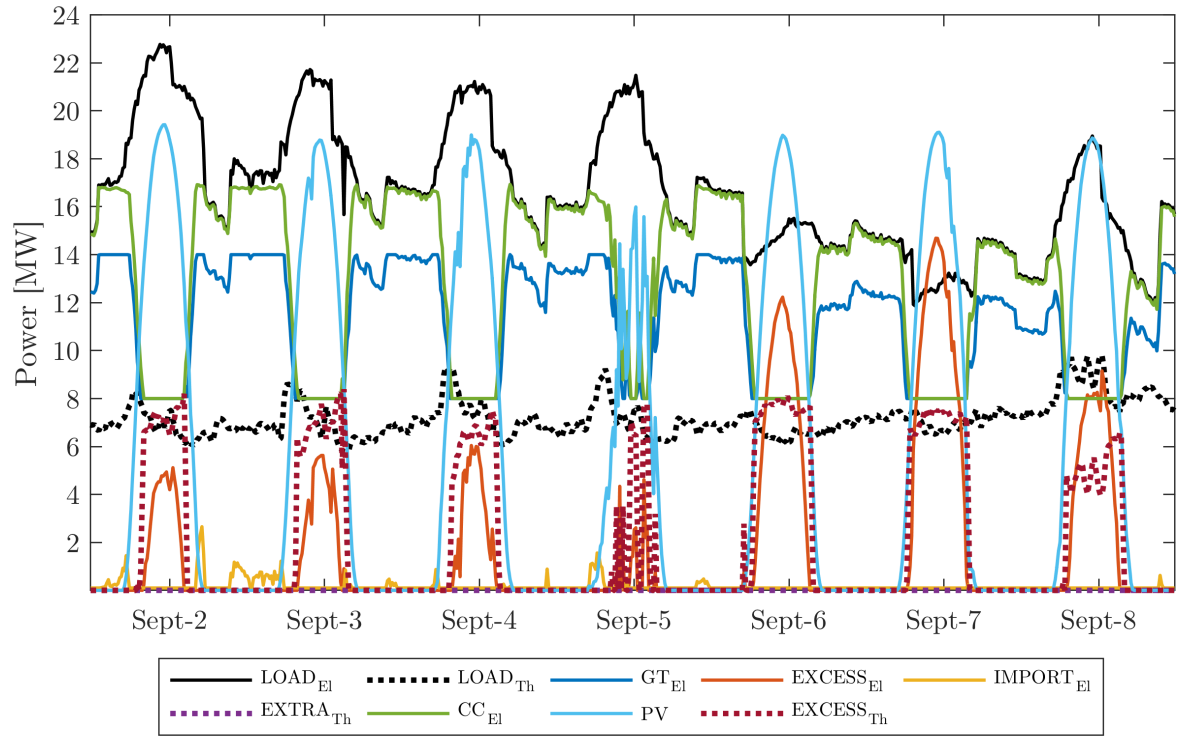
Figure 41. Microgrid dispatch simulation results in a week of September with 25 MW of PV installed capacity.
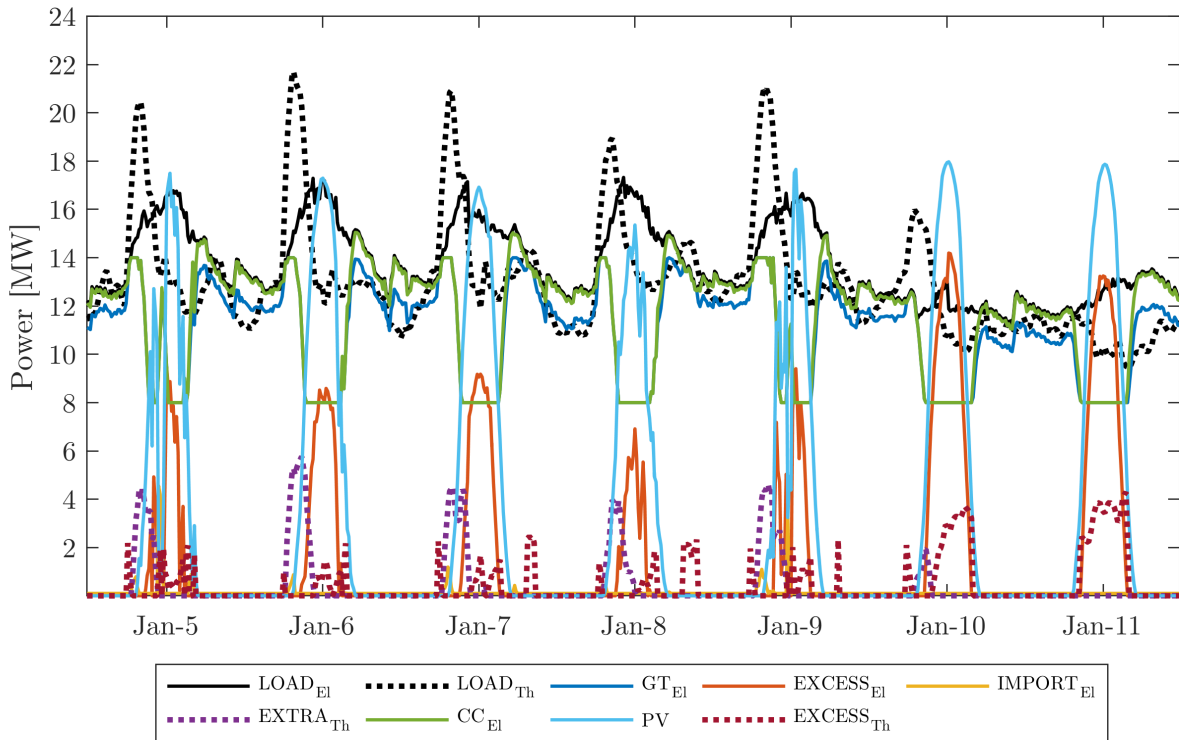
Figure 42. Microgrid dispatch simulation results in a week of January with 25 MW of PV installed capacity.

73

5.2 Photovoltaic deployment future perspective

The microgrid dispatch results are summarized in Figure 43 highlighting the contribution of the available electrical energy sources to the annual electricity demand of the campus, from the current situation with 4 MW of photovoltaic installed capacity to the maximum local estimated capacity of 35 MW. The red line represents the percentage of the energy produced by the future photovoltaic installations that cannot be absorbed by the microgrid and would have to be curtailed.

Currently the campus cogeneration plant provides around 94% of the campus needs, 83% of electricity production comes from the gas turbine and 10% from the steam turbine. summing the contribution of gas and steam turbines. The photovoltaic production can be fully absorbed by the microgrid and covers 5% of the annual campus electricity demand. The imported electricity from the external grid is needed to supply only 1% of the electrical demand.

The general trend is obviously the increase of renewable energy penetration as the installed photovoltaic capacity increases with consequent decrease of gas turbine and steam turbine contribution. The electricity import from the external grid shows a slight decrease but stays around 1% because of the current interconnection agreement that impose a continuous minimum import.
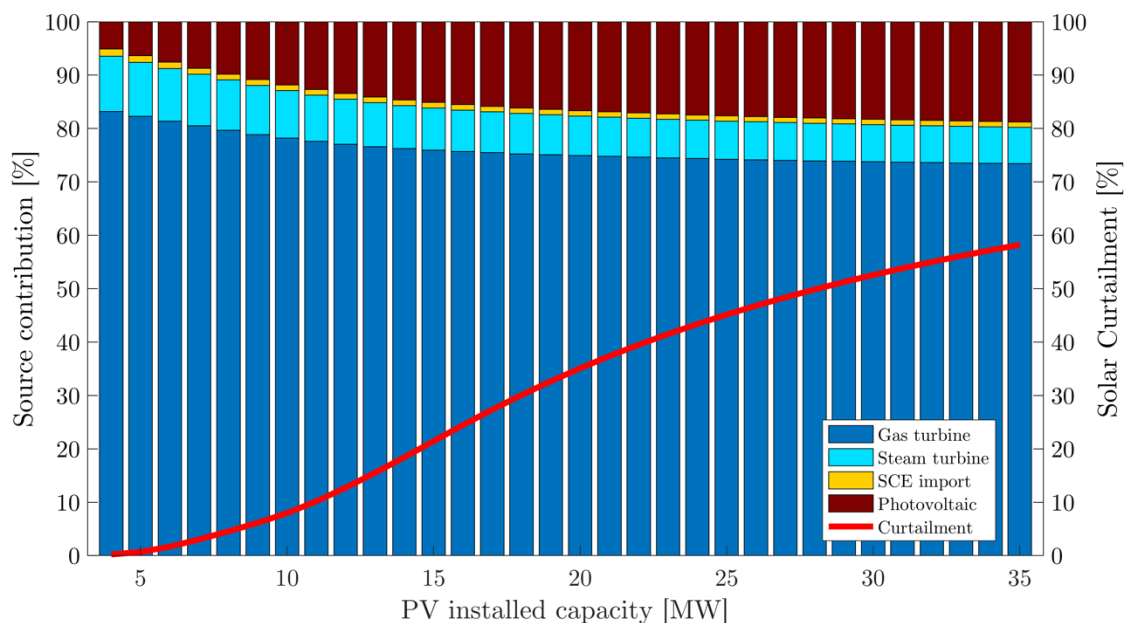
Figure 43. UCI microgrid energy generation mix and electricity curtailments in future scenarios with increased photovoltaic installed capacity.

The intrinsic limits of the microgrid structure, due to the power plant operation constraints, start to show as the amount of solar energy that would have to be curtailed immediately start to increase as the photovoltaic installed capacity. Installing new capacity up to 15 MW would result in sensible increasing in renewable energy contribution from 6 to 15 %, keeping solar curtailment around 20% of the production. Scenarios with further increasing of photovoltaic capacity show that only a 4% increase of renewable penetration is achieved up to 19% if the installed capacity increase from 15 MW to 35 MW. In the same range the percentage of excessive photovoltaic production that would has to be curtailed increases from 20% to 58%.

In Figure 44 are showed the distribution of excess of photovoltaic power in terms of entity and frequency. On the y-axis there is the indication of the number of hours of the year during which the excess power is at least the value that can be red on the x-axis. The six lines corresponds to scenarios with increasing photovoltaic capacity. The intercepts points with the y-axis are the total number of hours with curtailment while the intercepts point with the x-axis represent the maximum annual value of excess power.

It can be highlighted that the peak power evolves linearly with the increase of installed capacity while the number of excess hours increase rapidly for scenarios up to 15 MW and then the growth slow down converging to the total number of hours of photovoltaic production meaning that the additional capacity cannot be handle by the grid as previously showed. The massive curtailment can be noticed as the general trend of the curves change moving toward higher PV scenarios and more and more hours present excess power closer to the maximum than to the minimum value.

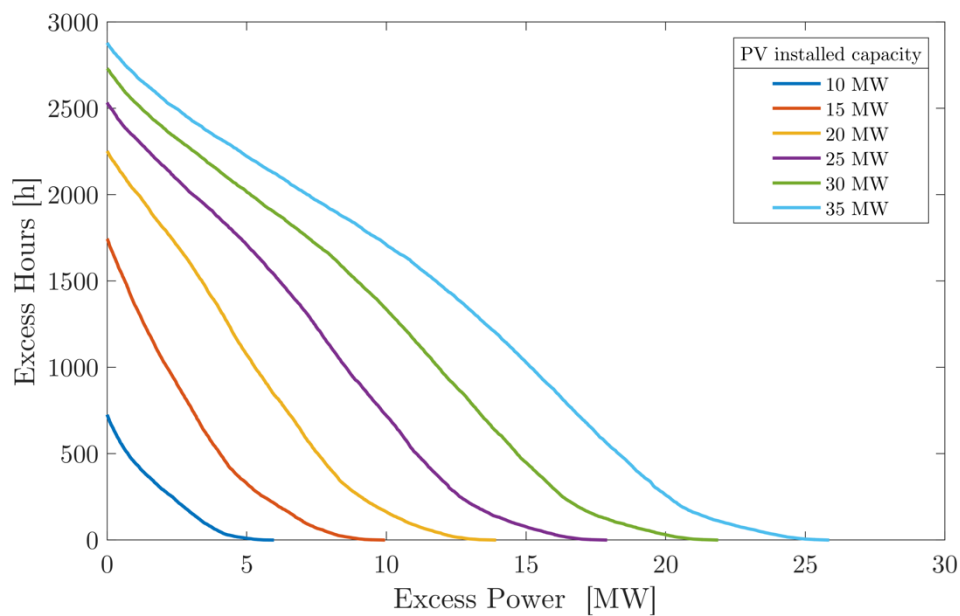**Figure 44.** Excess power distribution in future scenarios with increased photovoltaic installed capacity.

5.3 SOEC Systems dispatch

The estimations of the potential hydrogen production that could be obtained integrating high temperature electrolysis system with the existing microgrid structure are presented in this section. Simulation have been performed for every installed photovoltaic capacity scenario comparing the two dispatch strategies described in Section 4.4 and the possibility of heat integration with the heat recovery section of the cogeneration plant for steam supply. Results labeled as "NO Steam integration" refers to simulations in which the steam is internally generated in the electrolysis system while results labeled as "Steam integration" refer to simulation in which the possibility to feed the electrolysis system with steam generated from the exhausts of the gas turbine has been taken into account. Representative results are showed in Figure 45-48 and summarized in Table 10.

A sensitivity analysis on the number of SOEC modules have been performed implementing the Parallel dispatch strategy and the results reported in this section for the comparison with the Sequential dispatch refer to the results of the sensitivity analysis case in which the highest annual hydrogen production has been obtained.

Only scenarios relatives to installed photovoltaic capacity higher than 10 MW have been reported here because with lower capacity the electricity excess doesn't occur on a daily basis and this fact would result in longer periods of shut off for the electrolysis system requiring further calculations on the thermal management of the idle mode.

From the comparison of the annual hydrogen production showed in Figure 45 can be noticed that, as previously explained, scenarios with PV capacity higher than 15 MW would result in massive energy curtailment and this increase is reflected by the hydrogen production potential that for a doubled PV capacity, from 10 to 20 MW, shows an almost nine fold increase, regardless of the dispatch strategy selected, passing from around 26 t/y to values higher than 230 t/y.

The integration of the electrolysis process allows an increase of annual hydrogen production with respect to the stand-alone case of around 2-3 % in the case of sequential dispatch and around 10 % in the case of the parallel dispatch strategy. In particular the steam integration in the case of parallel dispatch yields in the highest annual hydrogen production values in every scenario resulting as the best integration strategy.

These results can be analyzed from the point of view of the average annual efficiency of the electrolysis process evaluated according to Equation (47) and showed in Figure 46.

$$\eta_{SOEC,Average} = \frac{m_{H_2,Annual} \cdot LHV_{H_2}}{E_{SOEC,Annual}} \tag{47}$$

where $m_{H_2,Annual}$ is the amount of hydrogen produced in one year, LHV_{H_2} is lower heating value of hydrogen and $E_{SOEC,Annual}$ is the total electric energy delivered to the SOEC modules over the year.

As expected the steam integration with the campus power plant results in higher efficiencies for both of the dispatch strategies but in the case of Parallel dispatch the average efficiency reaches values around 80%$_{LHV}$, remarkable values for electricity conversion into hydrogen. Moreover, this integration strategy can achieve the highest amount of hydrogen production with the deployment of less electrolysis module compared to Sequential dispatch in scenarios of PV lower than 30 MW. A much lower investment cost would be required with this integration strategy at given hydrogen production, resulting in a better choice from the economic point of view. The small increase in average efficiency between the heat integration and the stand alone configuration in the case of sequential dispatch, is related to the electrolysis system operating conditions and system internal heat integration defined in Section 2.3; the system has been designed to maximize internal heat recovery from the stack outlet streams and, as a consequence, when the system operates exothermically at full load the additional energy consumption of the electric steam generator is very low as can be noticed from Figure 34 resulting in a reduced advantage when an alternative heat source is available.

A last consideration on the dispatch strategy comparison can be made about the percentage of the microgrid excess power that cannot be delivered to the electrolysis system as showed in Figure 47. The sequential dispatch allows to better follow excess power variations in particular at the beginning and at the end of every excess period when the excess power is lower than the cut-on threshold. When the Sequential dispatch is applied the cut-on threshold corresponds to the minimum system consumption of one module (120 kW) while, when the Parallel dispatch is applied the cut-on threshold is equal to the minimum consumption of the single module multiplied by the number of modules (N·120 kW). Applying sequential dispatch less than 2% of the excess electricity from the microgrid cannot be delivered to the electrolysis system in every scenario. If the parallel dispatch is applied a lower percentage of excess electricity can be delivered to the electrolysis system especially in the scenarios with photovoltaic capacity lower than 15 MW in which the unused excess electricity reaches 10%. Nevertheless, the parallel dispatch strategy would be a better choice especially in future scenarios of large photovoltaic installations in which the daily excess power rapidly increases in the morning above the cut-on threshold reducing the percentage of unused excess electricity to values lower than 6%.

It needs to be highlighted that in the scenario with the maximum photovoltaic capacity the total electrolysis capacity deployed would be around 26 MW so in the hypothesis of large deployment of renewable energy sources a careful economic analysis between the costs of curtailment, costs of electrolyzers deployment and possible benefits derived by the hydrogen production must be performed to evaluate the optimal solution.
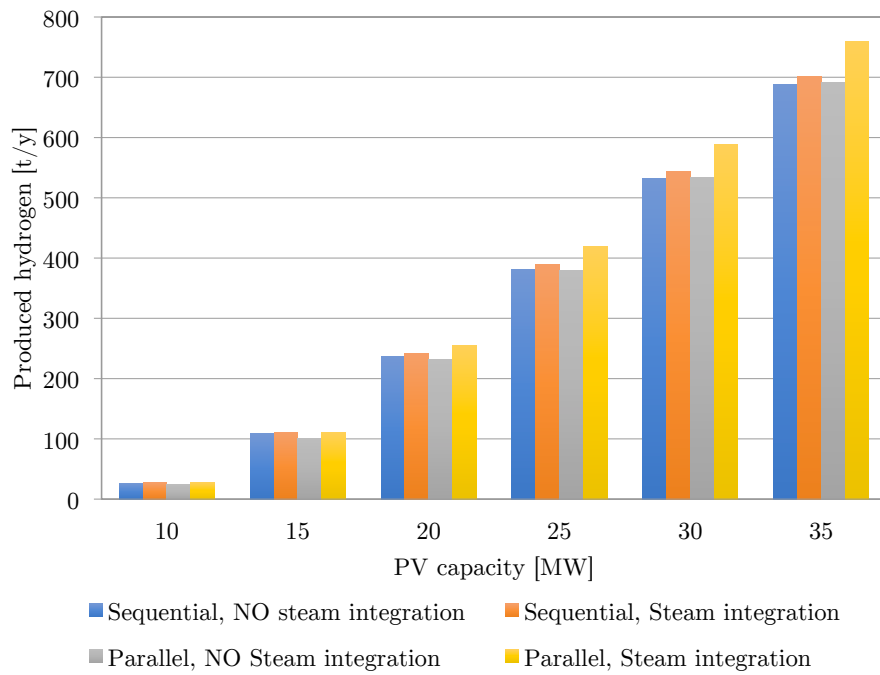
Figure 45. Comparison of annual hydrogen production for scenarios with increasing photovoltaic installed capacity depending on SOEC modules dispatch strategy.
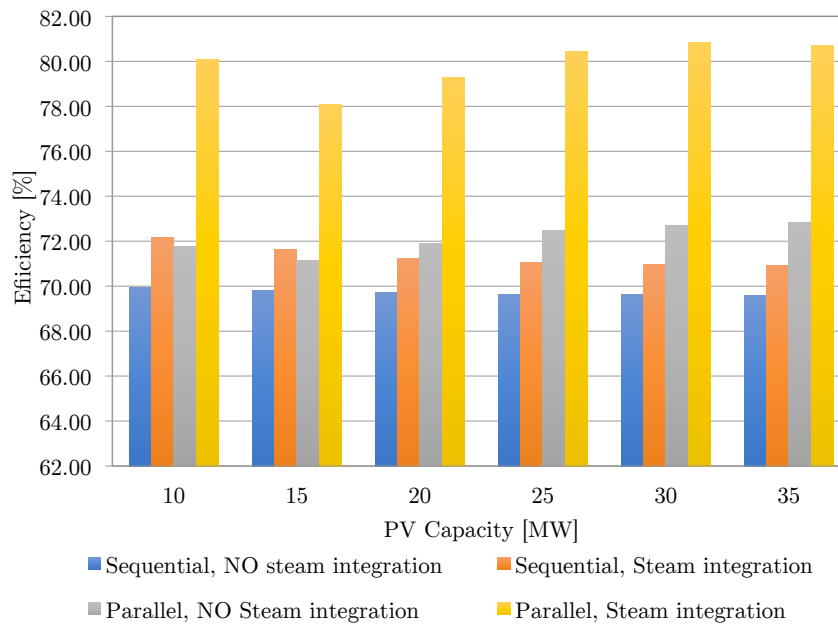
Figure 46. Comparison of annual average hydrogen production efficiency for scenarios with increasing photovoltaic installed capacity depending on SOEC modules dispatch strategy.

Figure 47. Comparison of annual percentage of unused excess electricity for scenarios with increasing photovoltaic installed capacity depending on SOEC modules dispatch strategy.
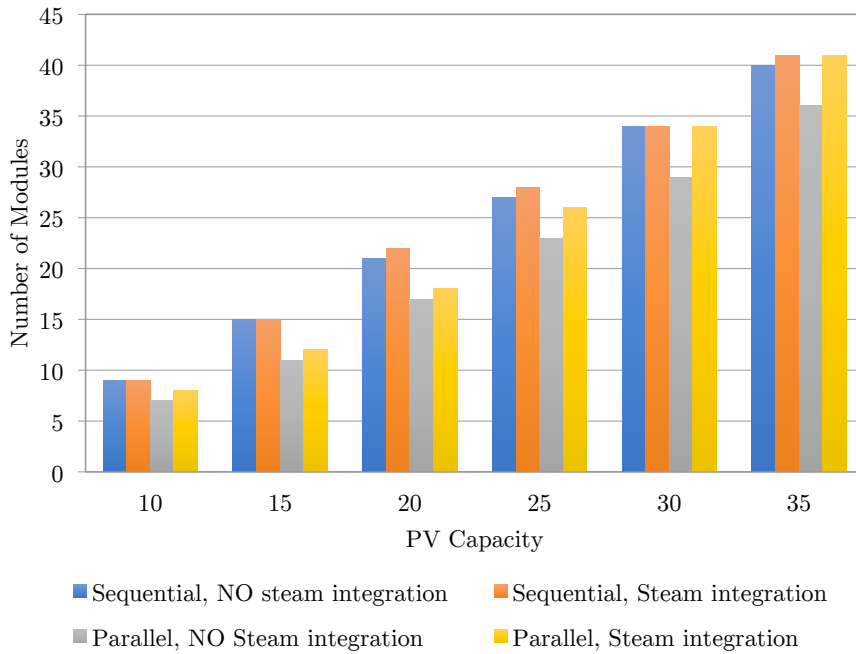
Figure 48. Comparison of the number of deployed modules for scenarios with increasing photovoltaic installed capacity depending on SOEC modules dispatch strategy.
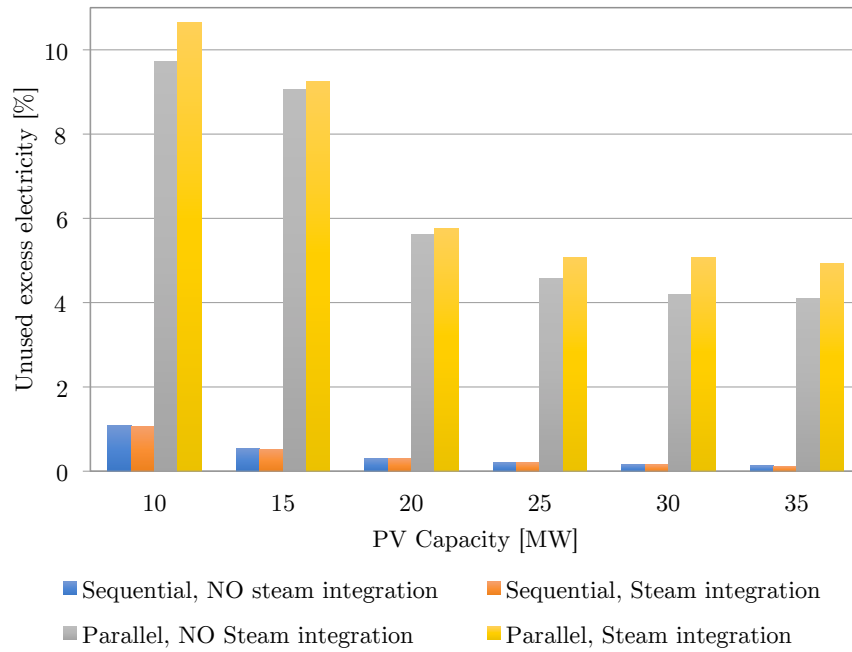
Table 10. Results of SOEC system microgrid integration.

H2 Production [t/y]				
PV capacity [MW]	Sequential dispatch		Parallel dispatch	
	NO Steam	Steam	NO Steam	Steam
10	26.758	27.610	25.047	27.670
15	108.481	111.299	101.111	110.705
20	236.945	242.145	231.315	254.806
25	381.094	388.898	379.215	418.710
30	532.558	542.982	533.494	588.008
35	688.235	701.278	691.321	759.731
Efficiency LHV [%]				
PV capacity [MW]	Sequential dispatch		Parallel dispatch	
	NO Steam	Steam	NO Steam	Steam
10	69.96	72.17	71.76	80.09
15	69.81	71.61	71.16	78.07
20	69.70	71.23	71.88	79.29
25	69.64	71.07	72.47	80.45
30	69.62	70.98	72.69	80.84
35	69.60	70.92	72.82	80.70
N [#]				
PV capacity [MW]	Sequential dispatch		Parallel dispatch	
	NO Steam	Steam	NO Steam	Steam
10	9	9	7	8
15	15	15	11	12
20	21	22	17	18
25	27	28	23	26
30	34	34	29	34
35	40	41	36	41
Unused excess solar power [%]				
PV capacity [MW]	Sequential dispatch		Parallel dispatch	
	NO Steam	Steam	NO Steam	Steam
10	1.08	1.05	9.72	10.65
15	0.54	0.52	9.06	9.24
20	0.29	0.30	5.61	5.75
25	0.20	0.20	4.57	5.08
30	0.16	0.15	4.20	5.07
35	0.13	0.12	4.11	4.92

5.4 On-site hydrogen utilization

The Power-to-gas system is based on the assumption that injecting hydrogen into the natural gas distribution network the hydrogen storage does not have to be built on site taking advantage of the virtually infinite existing storage volume. The amounts of hydrogen produced can be compared with possible on-site utilization capabilities such as the local hydrogen fueling station for fuel cell electric vehicles and the direct injection the produced hydrogen in the gas turbine inlet to reduce the natural gas consumption.

The local fueling station maximum daily delivery capacity is 180 kg/d and in 2017 the station delivered 48,599 kg resulting in an average daily hydrogen delivery of 133 kg, more than double the amount of the previous year. Therefore, in the unlikely perspective that the local hydrogen demand for mobility does not increase in the near future, the hydrogen fueling station could consume the whole renewable hydrogen production from the microgrid excess electricity up to the scenario with 11 MW of photovoltaic capacity, in which the average daily hydrogen production is around 140 kg. These values refer to the cases with Parallel dispatch strategy with steam integration implemented and can be compared in Figure 49.

Regarding the use of hydrogen as a fuel in existing gas turbines several studies are investigating the possibility to use a blend of natural gas and hydrogen as a temporary solution toward future energy systems based on fuel cells. A reference value for the hydrogen concentration limit that does not imply structural modification or important performance changes to existing devices is around 15%$_{vol}$ [51] [52].

The molar heating value of the gas mixture with the reference hydrogen volume concentration can be estimated according to Equation (48).

$$LHV_{mix} = x \cdot LHV_{H_2} + (1 - x) \cdot LHV_{NG} \tag{48}$$

where LHV_{H_2} and LHV_{NG} are the molar lower heating values of hydrogen and natural gas and x is the maximum volumetric hydrogen concentration. The maximum amount of hydrogen that could be injected into the gas turbine can be estimate with Equation (49) assuming that feeding the gas turbine with the mixture of hydrogen and natural gas does not affect the efficiency.

$$n_{H2,GT} = x \cdot \frac{E_{GT,El}/\eta_{GT,average}}{LHV_{mix}} \tag{49}$$

where $E_{GT,El}$ is the annual electric energy produced by the gas turbine, $\eta_{GT,average}$ the average electrical efficiency of the gas turbine and x the limit hydrogen concentration.

As can be seen from Figure 49, feeding the gas turbine with a gas mixture containing 15%$_{\text{vol}}$ hydrogen would suffice to consume the hydrogen produced up to the scenario with 27 MW of photovoltaic installed capacity. It is worth noting that the blending limit of hydrogen decreases with increasing photovoltaic capacity deployment because the electrical energy produced by the gas turbine decreases requiring lower fuel consumption.
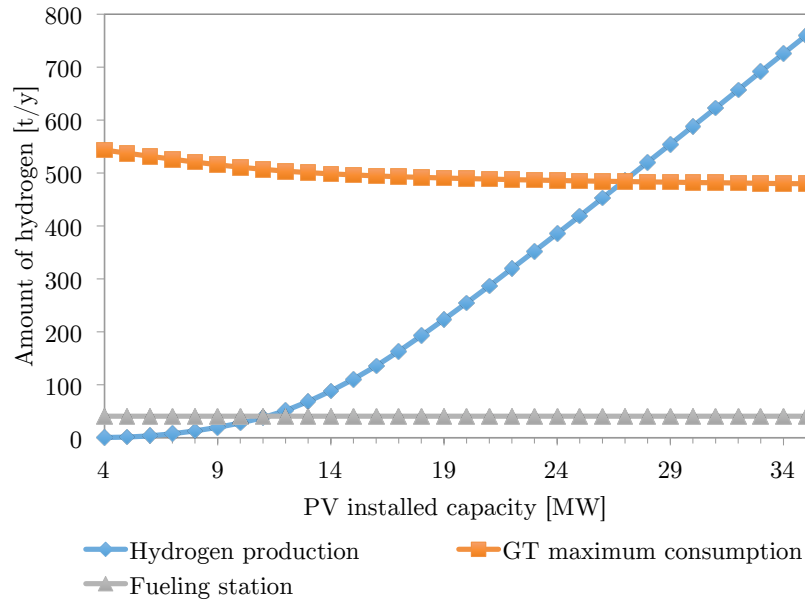

Figure 49. Comparison between hydrogen production and possible on-site consumption for scenarios with increasing PV installed capacity.

6 Conclusions

In the present work a physical dynamic model of a high temperature steam electrolysis system based on Solid Oxide Cells has been developed, characterizing the performance of the entire electrolysis process with a detailed analysis on the energy consumption of both stack and balance of plant components. Particular focus has been devoted to the development of a system control strategy suitable to obtain a wide range of operating loads, a necessary feature for energy storage systems coupled with variable renewable energy sources. Two control strategies have been compared, one based on the operation of the cell at a constant average temperature regardless of the thermodynamic behaviour and the other based on the definition of an allowable operating temperature range depending on the exothermic or endothermic operating conditions. A detailed investigation of the dynamic operation of the electrolysis system has been carried out evaluating the thermal stresses due to temperature gradients across the cells and the effectiveness of the implemented control strategies to mitigate temperature oscillations.

The results show that the operating range of the electrolysis system is 18-100%, corresponding to a stack load range of 12-100%, and that, implementing a control strategy that allows oscillations of the average cell temperature of 90°C around the nominal operating temperature, the electrolysis process can be performed with electrical efficiency higher than 70%$_{LHV}$ in the range 30-100% of stack load. The process electrical efficiency can be improved to values higher than 80%$_{LHV}$ if an external heat source is available for steam generation. The dynamic simulations performed did not highlight limitation and challenges related to thermal stresses on the cell confirming that solid oxide electrolysis is a promising technology for efficient hydrogen production from variable renewable energy sources that could allow the realization of large scale energy storage, paving the way to a future sustainable energy system.

The challenges of renewable energy sources penetration have been investigated in the context of the University of California, Irvine campus, simulating the existing power plant operation and examining the effects of increasing photovoltaic capacity installation.

The limits of the microgrid power plant have been identified and would result in massive electricity curtailment with no sensible increase in renewable energy consumption for photovoltaic installed capacity higher than 15 MW, if no energy storage solution is implemented.

The integration of a Power-to-Gas system based on solid oxide electrolysis with the campus microgrid has been modelled to evaluate the annual hydrogen production potential and the capability of the system to successfully absorb excess electricity from the photovoltaic installations. In particular, the opportunity to integrate the electrical feed of the electrolysis system with the excess photovoltaic power and to supply the steam necessary for the electrolysis process taking advantage of the existing heat recovery steam generator of the campus power plant has been explored. Two dispatch strategies have been suggested, the first assumes a sequential dispatch of electrolysis modules while the second one requires the parallel operation of the deployed electrolysis module. The dispatch strategies have been compared in terms of hydrogen production, average efficiency of electrochemical conversion, electrolyzers installed capacity and effectiveness of absorbing excess electricity from the microgrid. The electrical and thermal integration resulted to be energetically feasible allowing to achieve hydrogen production at remarkably high average electrical efficiency, higher than $80\%_{LHV,}$ if the parallel dispatch strategy is implemented. Compared to the other integration strategies up to 9% more hydrogen could be produced with the deployment of the same electrolysis capacity.

7 References

[1] T. Tian and P. Beiter, "2015 Renewable Energy Data Book.USDOE Office of Energy Efficiency and Renewable Energy (EERE)," 2016.

[2] P. Denholm and R. Margolis, "Energy Storage Requirements for Achieving 50 % Solar Photovoltaic Energy Penetration in California," NREL, 2016.

[3] B. Sørensen, *Solar Energy Storage*. Elsevier, 2015.

[4] B. Dunn, H. Kamath, and J.-M. Tarascon, "Electrical Energy Storage for the Grid: A Battery of Choices," *Science (80-.).*, vol. 334, no. 6058, p. 928 LP-935, Nov. 2011.

[5] Z. Yang *et al.*, "Electrochemical Energy Storage for Green Grid," *Chem. Rev.*, vol. 111, no. 5, pp. 3577–3613, May 2011.

[6] N. P. Brandon and Z. Kurban, "Clean energy and the hydrogen economy," *Philos. Trans. R. Soc. A Math. Eng. Sci.*, vol. 375, no. 2098, Jun. 2017.

[7] "Power-to-Gas: The case of Hydrogen, (White Paper)," California Hydrogen Buisness Council, Los Angeles,CA, 2015.

[8] M. A. Pellow, C. J. M. Emmott, C. J. Barnhart, and S. M. Benson, "Hydrogen or batteries for grid storage? A net energy analysis," *Energy Environ. Sci.*, vol. 8, no. 7, pp. 1938–1952, 2015.

[9] J.-P. Maton, L. Zhao, and J. Brouwer, "Dynamic modeling of compressed gas energy storage to complement renewable wind power intermittency," *Int. J. Hydrogen Energy*, vol. 38, no. 19, pp. 7867–7880, 2013.

[10] *Grant Solicitation GFO-15-605 Light Duty Vehicle Hydrogen Refueling Infrastructure*. Sacamento,CA: California Energy Commision, 2017.

[11] L. Zhao and J. Brouwer, "Dynamic operation and feasibility study of a self-sustainable hydrogen fueling station using renewable energy sources," *Int. J. Hydrogen Energy*, vol. 40, no. 10, pp. 3822–3837, 2015.

[12] C. Philibert, "Producing ammonia and fertilizers: new opportunities from renewables," 2017.

[13] J. Mougin, "8 - Hydrogen production by high-temperature steam electrolysis," in *Compendium of Hydrogen Energy*, V. Subramani, A. Basile, and T. N. Veziroğlu, Eds. Oxford: Woodhead Publishing, 2015, pp. 225–253.

[14] J. B. Hansen, "Solid oxide electrolysis - a key enabling technology for sustainable energy scenarios," *Faraday Discuss.*, vol. 182, , pp. 9–48, 2015.

[15] J. Mermelstein and O. Posdziech, "Development and Demonstration of a Novel Reversible SOFC System for Utility and Micro Grid Energy Storage," *Fuel Cells*, p. n/a-n/a, Jan. 2016.

[16] J. Mermelstein, C. Cannova, M. Cruz, and B. Anderson, "Field Demonstration of a Novel Reversible SOFC System for Islanded Microgrid Energy Storage," *ECS Trans.* , vol. 78, no. 1, pp. 2907–2912, May 2017.

[17] K. Schwarze, O. Posdziech, S. Kroop, N. Lapeña-Rey, and J. Mermelstein, "Green Industrial Hydrogen via Reversible High-Temperature Electrolysis," *ECS Trans.*, vol. 78, no. 1, pp. 2943–2952, May 2017.

[18]   E. Tang *et al.*, "Advanced Materials for RSOFC Dual Operation with Low Degradation," 2012.

[19]   A. Wood, H. He, T. Joia, M. Krivy, and D. Steedman, "Communication—Electrolysis at High Efficiency with Remarkable Hydrogen Production Rates," *J. Electrochem. Soc.*, vol. 163, no. 5, pp. F327–F329, Jan. 2016.

[20]   J. Schefold, A. Brisse, and F. Tietz, "Nine Thousand Hours of Operation of a Solid Oxide Cell in Steam Electrolysis Mode," *J. Electrochem. Soc.* , vol. 159, no. 2, pp. A137–A144, Jan. 2011.

[21]   J. Schefold, A. Brisse, and H. Poepke, "23,000 h steam electrolysis with an electrolyte supported solid oxide cell," *Int. J. Hydrogen Energy*, vol. 42, no. 19, pp. 13415–13426, 2017.

[22]   A. Hauch, K. Brodersen, M. Chen, and M. B. Mogensen, "Ni/YSZ electrodes structures optimized for increased electrolysis performance and durability," *Solid State Ionics*, vol. 293, pp. 27–36, 2016.

[23]   A. Houaijia, M. Roeb, N. Monnerie, and C. Sattler, "Solar power tower as heat and electricity source for a solid oxide electrolyzer: A case study," *Int. J. Energy Res.*, vol. 39, no. 8, 2015.

[24]   A. A. AlZahrani and I. Dincer, "Design and analysis of a solar tower based integrated system using high temperature electrolyzer for hydrogen production," *Int. J. Hydrogen Energy*, vol. 41, no. 19, 2016.

[25]   J. Sanz-Bermejo, J. Muñoz-Antón, J. Gonzalez-Aguilar, and M. Romero, "Optimal integration of a solid-oxide electrolyser cell into a direct steam generation solar tower plant for zero-emission hydrogen production," *Appl. Energy*, vol. 131, 2014.

[26]   J. Sanz-Bermejo, V. Gallardo-Natividad, J. González-Aguilar, and M. Romero, "Coupling of a solid-oxide cell unit and a linear fresnel reflector field for grid management," in *Energy Procedia*, 2014, vol. 57.

[27]   Q. Cai, N. P. Brandon, and C. S. Adjiman, "Modelling the dynamic response of a solid oxide steam electrolyser to transient inputs during renewable hydrogen production," *Front. Energy Power Eng. China*, vol. 4, no. 2, pp. 211–222, Jun. 2010.

[28]   Q. Cai, C. S. Adjiman, and N. P. Brandon, "Optimal control strategies for hydrogen production when coupling solid oxide electrolysers with intermittent renewable energies," *J. Power Sources*, vol. 268, no. Supplement C, pp. 212–224, 2014.

[29]   F. Petipas, A. Brisse, and C. Bouallou, "Modelled behaviour of a high temperature electrolyser system coupled with a solar farm," *Chem. Eng. Trans.*, vol. 45, 2015.

[30]   J. Sanz-Bermejo, J. Muñoz-Antón, J. Gonzalez-Aguilar, and M. Romero, "Part load operation of a solid oxide electrolysis system for integration with renewable energy sources," *Int. J. Hydrogen Energy*, vol. 40, no. 26, 2015.

[31]   J. Sigurvinsson, C. Mansilla, P. Lovera, and F. Werkoff, "Can high temperature steam electrolysis function with geothermal heat?," *Int. J. Hydrogen Energy*, vol. 32, no. 9, pp. 1174–1182, 2007.

[32]   R. Rivera-Tinoco, C. Mansilla, and C. Bouallou, "Competitiveness of hydrogen production by High Temperature Electrolysis: Impact of the heat source and identification of key parameters to achieve low production costs," *Energy Convers. Manag.*, vol. 51, no. 12, pp. 2623–2634, 2010.

[33]   E. Giglio, A. Lanzini, M. Santarelli, and P. Leone, "Synthetic natural gas via integrated high-temperature electrolysis and methanation: Part I—Energy performance," *J. Energy Storage*, vol. 1, pp. 22–37, 2015.

[34] C. H. Wendel and R. J. Braun, "Design and techno-economic analysis of high efficiency reversible solid oxide cell systems for distributed energy storage," *Appl. Energy*, vol. 172, pp. 118–131, 2016.

[35] D. McLarty, J. Brouwer, and S. Samuelsen, "A spatially resolved physical model for transient system analysis of high temperature fuel cells," *Int. J. Hydrogen Energy*, vol. 38, no. 19, pp. 7935–7946, 2013.

[36] D. McLarty, S. Samuelsen, and J. Brouwer, "Novel Dynamic Quasi-3-Dimensional High Temperature Fuel Cell Model With Internal Manifolding," in *ASME 2010 8th International Fuel Cell Science, Engineering and Technology Conference: Volume 2*, 2010, pp. 257–268.

[37] F. Petipas, A. Brisse, and C. Bouallou, "Model-based behaviour of a high temperature electrolyser system operated at various loads," *J. Power Sources*, vol. 239, no. Supplement C, pp. 584–595, 2013.

[38] D. Ferrero, A. Lanzini, M. Santarelli, and P. Leone, "A comparative assessment on hydrogen production from low- and high-temperature electrolysis," *Int. J. Hydrogen Energy*, vol. 38, no. 9, pp. 3523–3536, 2013.

[39] M. Fardadi, D. Mclarty, and F. Jabbari, *Controlling Spatial Temperature Variation in a Rapid Load Following SOFC*. 2013.

[40] M. Fardadi, D. F. McLarty, and F. Jabbari, "Actuator Limitations in Spatial Temperature Control of SOFC," *J. Fuel Cell Sci. Technol.*, vol. 10, no. 3, pp. 31005-31005–10, May 2013.

[41] K. J. Albrecht and R. J. Braun, "Dynamic Modeling of SOFC Cogeneration Systems for Light Commercial Applications," in *ASME 2014 12th International Conference on Fuel Cell Science, Engineering and Technology*, 2014.

[42] D. Villarreal, "Reversible solid oxide cells for bidirectional energy conversion in spot electricity and fuel markets," Columbia University, 2017.

[43] J. Mougin *et al.*, "Development of a Solid Oxide Electrolysis Stack Able to Operate at High Steam Conversion Rate and Integration into a SOE System," *ECS Trans.*, vol. 78, no. 1, pp. 3065–3075, May 2017.

[44] A. Buttler and H. Spliethoff, "Current status of water electrolysis for energy storage, grid balancing and sector coupling via power-to-gas and power-to-liquids: A review," *Renew. Sustain. Energy Rev.*, vol. 82, pp. 2440–2454, 2018.

[45] "UCI Microgrid," *Bridg. Adv. Power Energy Progr.*, 2016.

[46] S. Samuelsen, F. Mueller, J. Eichman, and B. Tarroja, "Piloting the integration and use of renewables to achieve a flexible and secure energy infrastructure," Irvine,CA, 2014.

[47] R. YLL PROUS, "Dynamic dispatch and control of hydrogen energy storage from solar power in microgrids," UNIVERSITY OF CALIFORNIA,IRVINE, 2015.

[48] D. McLarty, C. Civit Sabate, J. Brouwer, and F. Jabbari, "Micro-grid energy dispatch optimization and predictive control algorithms; A UC Irvine case study," *Int. J. Electr. Power Energy Syst.*, vol. 65, pp. 179–190, Feb. 2015.

[49] "Renewable 'Power-to-Gas' proof oc concept is a success," *Bridging, Advanced Power and Energy Program*, Irvine,CA, 2017.

[50] V. Chandan *et al.*, "Modeling and Optimization of a Combined Cooling, Heating and Power Plant System," in *2012 American Control Conference (ACC 2012)*, 2012.

[51]   B. Shaffer, B. Tarroja, and S. Samuelsen, "ADVANCING TOWARD SUSTAINABILITY GOALS AT THE UNIVERSITY OF CALIFORNIA, IRVINE," in *Proceedings of the ASME 2014 8th International Conference on Energy Sustainability*, 2014.

[52]   A.-T. V. Do, "Performance and Controls of Gas Turbine-Driven Combined Cooling Heating and Power Systems for Economic Dispatch," University of California, Irvine, 2010.

[53]   M. Andersson, J. Larfeldt, and A. Larsson, "Co-firing with hydrogen in industrial gas turbines," Malmo,SWE, 2013.

[54]   E. Heimdal, J. Larfeldt, M. Rokka, and V. Karlsson, "Hydrogen gas as fuel in gas turbines," 2015.